Patrick KOLAR, BSc

Advanced Particle Evaluation Method for Numerical Simulation of the Liquid Break-Up with the Volume-of-Fluid Method

MASTERARBEIT

zur Erlangung des akademischen Grades
Diplomingenieur
Masterstudium Maschinenbau

eingereicht an der

Technischen Universität Graz

Betreuer
Ao.Univ.-Prof. Dipl.-Ing. Dr.techn. Raimund Almbauer
Institut für Verbrennungskraftmaschinen und Thermodynamik

Zweitbetreuer
DI. Dr.techn. Wilfried Edelbauer
AVL List GmbH

Graz, September 2017

Institut für Verbrennungskraftmaschinen und Thermodynamik
Vorstand: Univ.-Prof. DI Dr. Helmut Eichlseder

Preamble

In the end of my working activity at the Advanced Simulation Technologies (AST) division at AVL List GmbH in Graz, Austria it was reasonable to ask for the possibility to do my master thesis in the field of multiphase flow. I was lucky that Dr. Wilfried Edelbauer stood up for me to do the thesis at Advanced Simulation Technologies in the desired part of fluid mechanics.

First of all, I want to thank my supervisor Univ.-Prof. Dipl.-Ing. Dr.techn. Raimund Almbauer from the Institute of Internal Combustion Engines and Thermodynamics for his decision to supervise me and his support during my work on this thesis.

Another person I'd particulary like to thank is my supervisor from AVL List GmbH Dr. Wilfried Edelbauer. He was always there to answer questions and during our little coffee breaks he gave some good inputs to guide me in the right direction. Many other persons at AVL took part to fulfill this thesis, so a thank-you must be extended to them too.

I also want to thank my girlfriend Alexandra who was always supportive. She cheered me up during difficult situations I had while writing this thesis. Without her, this thesis would have a lot more grammar and spelling mistakes.

At last I have to thank my parents Rosa and Johann. They always had an understanding for my actions and supported me all the way through my studies.

Table of Content

Eidesstattliche Erklärung

Ich erkläre an Eides statt, dass ich die vorliegende Arbeit selbstständig verfasst, andere als die angegebenen Quellen/Hilfsmittel nicht benutzt, und die den benutzten Quellen wörtlich und inhaltlich entnommenen Stellen als solche kenntlich gemacht habe. Das in TUGRAZonline hochgeladene Textdokument ist mit der vorliegenden Masterarbeit identisch.

I declare that I have authored this thesis independently, that I have not used other than the declared sources/resources, and that I have explicitly indicated all material which has been quoted either literally or by content from the sources used. The text document uploaded to TUGRAZonline is identical to the present master's thesis.

Patrick KOLAR

Graz, 09.09.2017

Abstract

The main task of this master thesis was to introduce and implement a new tool for particle length detection in multiphase flow simulations. Before this thesis was done, the evaluation of the particle length of the dispersed fluid was not possible. Only volume or mass equivalent diameters for droplet size distribution were able to be calculated and used to evaluate the particle sizes in a multiphase flow computation. All numerical simulations were done with the multiphase module of the Computational Fluid Dynamics software AVL-FIRE^{TM}. The code applies several numerical methods for simulation of the liquid spray break-up. In this thesis, the Eulerian-Eulerian method and the Volume-of-Fluid method were used to observe the introduced algorithm for particle length detection on an industrial injector.

The content of this work is divided in three main parts and will briefly be summarized below. First, the algorithm of the particle length detection was developed. It is the foundation of further testing and evaluation investigations and uses the volume fraction method to detect the coherent structure. The code is not limited for detection of a single particle, it is working for a big number of particles and can be used for multi-core simulations. In combination with the particle lengths algorithm another technique for particle shapes illustration was introduced, the so called particle form diagram.

The second part includes the testing of the new techniques where more than seventy different cases which belong to the category of multiphase flow were observed. Therefore, the resulting values of the main moments of inertia and the mass were compared with the results of an analytical solution to observe the particle shape and were illustrated to a normalized variable diagram.

The third part includes the simulation of an industrial injector. The simple advection tests to evaluate a single fluid particle were the basis for a real case simulation of a low-pressure gasoline injector, which shows the advantages and disadvantages of the used numerical scheme. The low-pressure injector includes cavitation effects in the flow domain of the nozzle and tented to vaporization. Also, the liquid phase interacts with the ambient gas outside the nozzle. Due to that it was necessary to calculate the multiphase flow with two different numerical methods. The liquid-gas interface was calculated with the Volume-of-Fluid approach and the Eulerian-Eulerian framework computes the liquid-vapor interaction. This was done to avoid a very high mesh resolution in the computation region. The coupling of both methods is a big advantage for a multiphase flow simulation in AVL-FIRE^{TM}. In this thesis, a comparison for a low-pressure gasoline injector was done with experimental data, which shows good agreements and accurate numerical results, this works well with the introduced form and particle length detection.

Key words: particle length detection, particle form diagram, Volume-of-Fluid, Eulerian-Eulerian, cavitation, primary breakup, liquid jet

NOMENCLATURE

Latin symbols

A	m^2	area
a, b,c	m	spatial distance
C_S	-	Smagorinsky coefficient
C_{cav}	-	scaling factor cavitation mass transfer
C_{con}	-	scaling factor condensation mass transfer
C_{drag}	-	drag coefficient
D	m	diameter
d	m	distance vector
E	s^{-2}	magnitude of velocity gradient tensor
F_{CS}	-	coherent structure function
F_{drag}	N	drag force
F_Ω	-	energy decay suppression function
f_B	N/m^3	body force
g	m/s^2	gravitational acceleration
I	kg/m^2	moment of inertia / product of inertia
M	N/m^3	inter-phase momentum exchange
N'''	m^{-3}	bubble number density
n	-	number
p	Pa	pressure
Oh	-	Ohnesorge number
Q	s^{-2}	second invariant of velocity gradient tensor
R	m	radius
Re	-	Reynolds number
S	s^{-1}	velocity strain tensor
S_α	1/s	source term in volume fraction equation
t	s	time
U	m/s	velocity
V	m^3	volume
We	-	Weber number
W	s^{-1}	vortricity tensor
x	m	space coordinate

Greek symbols

$\tilde{\alpha}$	-	normalized volume fraction
ν^t	m^2/s	eddy viscosity
α	-	volume fraction
β	-	functional relationship between normalized donor cell and face value
γ	-	blending factor between two differencing schemes
Δ	m	cell size
ϵ	m^2/s^3	turbulence dissipation rate
θ	rad	angle
κ	1/m	curvature
η	m	Kolmogorov length scale
$\mathit{\Gamma}$	$kg/(m^3s)$	inter phase mass transfer
μ	Ns/m^2	dynamic viscosity
ν	m^2/s	kinematik viscosity

ρ	kg/m^3	density
σ	N/m	surface tension coefficient
σ_{cav}	-	cavitation number
τ	N/m^2	shear stress
ξ, η, ζ		axis of the coordinates for arbitrary point

Subscripts

A	acceptor cell
cav	cavitation
cells	cells
con	condensation
d	donator
D	downwind cell
f	cell-face
i, j	vector component
k, p	phase indices
l	liquid
m	mixture
P	cell center
ph	phases
ref	refinement
sat	saturation
U	upwind cell
v	vapor

Abbreviations

ATS	Automatic Time Step
CBC	Convective Boundedness Criterion
CFL	Courant-Friedrich-Levy number
CSF	Continuum Surface Force
EE	Eulerian-Eulerian
GUI	Graphical User Interface
HR	High Resolution
NVD	Normalized Variable Diagram
UQ	Ultimate-Quickest
VOF	Volume-of-Fluid

1 Introduction

1.1 Definition of Multiphase Flow

Injector flows, splashing fuel in a tank or particle flow in a cyclone prefilter are only some examples, for technical applications of multiphase flows. These kind of fluid mechanics appear in phenomena in our daily environment and can be detected by opening the water tap, rainfall or bubble up gas in sparkling water bottles. One of the finest example for multiphase flow will be found in the book of Wallis [1] and incorporate an amendment as followed:

> *“A phase is simply one of the states of matter and can be a gas, liquid or solid. Multiphase flow is the simultaneous flow of several phases. Two-phase flow is the simplest case of multiphase flow”.*

For solving a multiphase problem in a numerical manner several methods and schemes were established today. In this work the physics behind were calculated in a numerical manner with AVL-FIRE^{TM}. A new method to calculate the ligament lengths was introduced by the author. To give a guaranty for correct implementation of the tool, a large number of test cases was calculated.

1.2 Task of the Master Thesis

Liquid spray break-up at industrial injectors is in general validated for droplet size distribution and are compared with experimental investigations as seen in Edelbauer et al. [2]. Before this thesis was done it was not possible to extract information about the particle form and length in multiphase Volume-of-Fluid simulation with the CFD-code AVL-FIRE^{TM}. This fact causes to introduce an algorithm to overcome this missing applications. The author works out a full analyzation tool for the particle length and form detection. The produced results are documented carefully in a separate output file which is the basis of the graphical representation for the particles form in a so called form diagram.

In general, a numerical scheme for Volume-of-Fluid simulation is evaluated by a comparison of figures from the numerical solution over the calculated time steps. This procedure is not an exact method to compare schemes, as it will be done afterwards in this work. To enhance the quality of testing, a uniform evaluation procedure was introduced in this thesis. It includes the particle length algorithm compared with the visualization of the results plotted in figures as seen in section 3.2. The testing of the introduced procedure was verified by more than seventy test cases to check the functionality of the code and to test the Multiphase Module of AVL-FIRE^{TM}. Therefore, a separate evaluation code was necessary, which is not part of the applied CFD-code. The numerical results were normalized and compared with analytical solutions and the normalized values were drawn over time in diagrams. This leads to a fast evaluation technique for the investigated multiphase schemes. Now it is possible to make a quantitative statement about the accuracy of the different schemes. Furthermore, the possibility for further enhancements will be provided with the new tools. The particle length detection and the form diagram has been implemented on this stage in AVL-FIRE^{TM} and customers are able to use them right now.

The last section of the thesis shows a multiphase flow problem for a three-phase low pressure gasoline injector and including liquid, vapor and air as ambient gas. The liquid and vapor fluid properties of the gasoline were extracted from the AVL database. This real test case was taken from the work of Ishimoto et al. [3], and it shows cavitation in the nozzle domain. The separate phases were solved with different multiphase methods and will be presented in detail in the theory section 2. The coupling of the methods was developed by Edelbauer [4]. The presented simulation was performed incompressible and isothermal.

The work of this thesis is divided in three fields of activities. After the theory in section 2, in section 3 the first part includes a new method to calculate the length of fluid particles in a multiphase flow domain. In combination with the particle length detection a graphical analyzing tool was introduced for a CFD calculation. The second activation in section 4 provides the testing for proving the correct implementation of the new particle length calculation tool. In the past, it was only possible to give a statement of the quality of a differencing scheme itself by evaluating post processing figures. With the introduced tool, it is now possible to give a quantitative statement of a scheme in a mathematical manner. At last in section 5, a real case of an injector is calculated to show that the new tool is also convenient for industrial multiphase flow calculations.

2 Theory

The numerical simulation of an injector flow presents a typical multiphase flow problem. In this thesis a two-phase calculation with liquid and gas was done, also an interaction with a third phase which represents vapor as fluid was calculated in one simulation. For the solution of a multiphase problem it is necessary to model the interface between the different phases. Two different methods are used to fulfil this demands, known as Eulerian-Eulerian (EE) and Volume-of-Fluid (VOF) method. Attention should be paid on the combination of the EE and VOF-method, how they are combined will be discussed later on. In the following section, only the basics which are needed to calculate a multiphase problem for an incompressible flow are mentioned briefly. Up next the methodology of both methods will be explained. At the end of the section the theory for particle length detection will be described. It leads to the background for the new powerful tool for particle length detection.

2.1 Eulerian-Eulerian Approach

The EE-mass ensemble averaging as described in the book of Drew and Passman [5] contains the governing equation for mass and momentum. Each phase k is solved separately, where the mass change in a control volume is caused by two different effects. For a component k the mass is changing during transport over the boundaries of the control volume which is better known as mass flux. The second variation includes the mass change during chemical production or phase change. In contrast to the VOF-method the EE-approach is not able to track the phase interphase, instead a distribution of the phase for a control volume will be solved. Each solved component takes a portion of the regarded volume, and the total portion is quantified by the volume fraction as defined:

$$\sum_{k=1}^{n_{ph}} \alpha_k = 1 \tag{2.1}$$

2.1.1 Balance Equation of the EE-Approach

The mass conservation equation is represented in Eq. (2.2) where the volume fraction is marked by α_k, the density of the phase represents ρ_k and t describes the time. The velocity vector $\mathbf{U}_{k,j}$ completes the right-hand side of the equation. The left-hand side stands for the sum of the interphase mass transfer Γ_{kp} over the number of phases n_{ph} and depends on the cavitation model, as seen in the section below. The indices contain a categorical differentiation between the phase k and phase p in the governing equations for mass and momentum in the EE-approach.

$$\frac{\partial \alpha_k \rho_k}{\partial t} + \frac{\partial}{\partial x_j}\left(\alpha_k \rho_k \mathbf{U}_{k,j}\right) = \sum_{p=1, p\neq k}^{n_{ph}} \Gamma_{kp} \tag{2.2}$$

The momentum equation for phase k leads to the form as defined in Eq. (2.3). Conventional on the right-hand side, the second term represents the viscous term which includes the shear stress $\boldsymbol{\tau}_{k,ij}$, the turbulence shear stress is $\boldsymbol{\tau}^t_{k,ij}$ and will be explained in section 2.3. The body force term $\mathbf{f}_{Bk,i}$ is the third term and includes the gravitational and surface tension forces in a vectorial manner. The last two terms in the momentum equation stand for the interphase momentum transfer and the momentum transferred by the inter phase mass transfer of the computation.

$$\begin{aligned}\frac{\partial \alpha_k \rho_k \mathbf{U}_{k,i}}{\partial t} + \frac{\partial}{\partial x_j}\left(\alpha_k \rho_k \mathbf{U}_{k,j} \mathbf{U}_{k,i}\right) = \quad & -\alpha_k \frac{\partial p}{\partial x_i} + \frac{\partial \alpha_k \left(\boldsymbol{\tau}_{k,ij} + \boldsymbol{\tau}_{k,ij}^{t}\right)}{\partial x_j} \\ & + \mathbf{f}_{Bk,i} + \sum_{p=1,p\neq k}^{n_{ph}} \left(M_{kp,i} + \mathbf{U}_{kp,i} \Gamma_{kp}\right)\end{aligned} \tag{2.3}$$

2.1.2 Eulerian-Eulerian Cavitation Model

The EE-approach which was discussed before includes the linear cavitation model, as described by Alajbegovic et al. [6]. The fundament of the model is the Rayleigh-Pleset equation for single bubble growth. The mass transfer term Γ_{kp} implies the mass transfer of a phase in case of phase change (see Drew and Passman [5]). For cavitating applications, the mass transfer is different for cavitation and condensation. Due to this separation, it leads to the mass transfer of cavitation $\Gamma_{lv,cav}$ as seen in Eq. (2.4), and mass transfer for condensation $\Gamma_{vl,con}$ which is presented in Eq. (2.5). Another difference will be found in the scaling factor for the mass transfer of cavitation C_{cav} and condensation C_{con} which are needed to fit the numerical model with experimental results. The difference between local pressure p_∞ and the saturation pressure p_{sat}, the term $p_\infty - p_{sat}$, is the driving force for cavitation.

$$\Gamma_{lv,cav} = C_{cav} \rho_v N''' 4\pi R_v^2 \sqrt{\frac{2|p_\infty - p_{sat}|}{3\rho_l}} \tag{2.4}$$

$$\Gamma_{vl,con} = -\frac{1}{C_{con}} \rho_v N''' 4\pi R_v^2 \sqrt{\frac{2|p_\infty - p_{sat}|}{3\rho_l}} \tag{2.5}$$

For the bubble number density N''' the approach described in the cavitation model of Sauer and Schnerr [7] can be applied. In this work the slightly different of AVL-FIRE™ is applied. It differs in the formulation of $N''' = f(\alpha_d)$ and in the density calculation. The bubble radius R_v, described in Eq. (2.6), contains the relation between the transported vapor volume fraction α_v and the bubble number density.

$$R_v = \left(\frac{3}{4}\pi\, \alpha_d \;\, N'''\right)^{\frac{1}{3}} \tag{2.6}$$

The inter phase momentum exchange $M_{lv,i}$ (Eq.(2.7)) includes the drag force term $\mathbf{F}_{drag,i}$,which was introduced by Schiller et al. [8]. C_{drag} is defined as the drag coefficient and is calculated by the relative bubble Reynold's number.

$$M_{lv,i} = N''' \mathbf{F}_{drag,i} = C_{drag} \frac{3}{8} \frac{\alpha_v \rho_l}{R_v} |\mathbf{U}_l - \mathbf{U}_v| \left(\mathbf{U}_{v,i} - \mathbf{U}_{l,i}\right) = -M_{vl,i} \tag{2.7}$$

2.2 Volume-of-Fluid Approach

The VOF-approach was originally introduced by Hirt and Nichols [9], and it uses the so called one-fluid formulation. It depends on solving the governing equations for an immiscible fluid. Both phases are tracked as mixture and share the same velocity in the control volume. The core of the VOF-method builds up the interface capturing of the mixture which is performed in this thesis with two different high resolution advection schemes. Both schemes, CICSAM as well as the HRIC scheme do not perform geometric reconstruction of the interface, as known from other methods. Depending on the solved values of the volume fraction it is possible to make a differentiation between considered phases and their boundaries. Examples given for two fluids, fluid one has volume fraction $\alpha = 1$ and fluid two has $\alpha = 0$. Cells, which have a volume fraction $0 \leq \alpha \leq 1$ include an interface. The sharpness of the interface is gained with smaller mesh cells, which leads to a higher numerical effort.

Next it will be explained how the surface tracking with the VOF-approach is working in general. The CFD-code AVL-FIRE^{TM} provides two different high resolution advection schemes. For both methods, the numerical solution procedure is the same. The difference lies in the determination of the cell-face value.

The explanation of the VOF-schemes capturing methods starts with the common form of transport equation for a volume fraction (see Eq.(2.8)). This section includes also the differences between the CICSAM and HRIC-schemes, and why they are needed in the solution procedure. When this is done, the governing equations for a three-phase cavitation simulation are shortly presented to round the section up.

2.2.1 The Volume Fraction Equation for VOF

The common form of the volume fraction equation is presented in Eq. (2.8), and is also discussed in the manual of AVL-FIRE^{TM} [10]. It is the governing equation for advection tests as seen in chapter 4, and for better understanding the solution procedure is described next.

$$\frac{\partial \alpha_k}{\partial t} + \frac{\partial}{\partial x_j}\left(\alpha_k \mathbf{U}_{m,j}\right) = 0 \tag{2.8}$$

The discretization of Eq. (2.8) uses the Crank Nicholson time integration as discussed up next. It is a common knowledge that VOF simulations needs low CFL- numbers. This leads to small time steps and the numerical calculations gains on duration and costs (see Hirsch [11]).

$$\left(\alpha_P^{t+\delta t} - \alpha_p^{t}\right) V_P = -\sum_{j=1}^{n_f} \frac{1}{2}\left[\left(\alpha_f\, F_f\right)^t + \left(\alpha_f\, F_f\right)^{t+\delta t}\right] \delta t \tag{2.9}$$

On the left-hand side of Eq.(2.9) the values corresponding to the cell center of the control volume are marked with index P. The exponent t stands for the time, and δt is the current time step. Where V_P denotes the volume of the control volume and α_p is the volume fraction in the center of the cell. The right-hand side presents the summation of the face values which are transported through the cell-faces itself and is marked with the index f. The cell-face volume fraction is presented by α_f, and the volumetric flux over face corresponds to F_f. A simplification is done for $F_f^{t+\delta t}$, because the value is not known at time of calculation and therefore it is approximated. The value of α_f has a larger variation compared to F_f over a time step of δt. This leads to the approximation that $F_f^{t+\delta t} \approx F_f^{t}$.

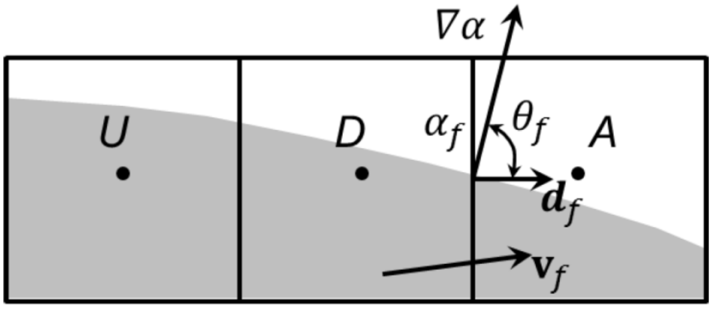

Figure 1: Visualization of the Upwind–, Donor- and Acceptor cells including the volume fraction gradient and the corresponding angle (AVL-FIRE™ manual [10]).

The core of the interface capturing method with the VOF-approach is the approximation of α_f which is a priori not known. To overcome this, the two high resolution (HR) schemes CICSAM and HRIC provide an approximation. As described in the manual of AVL-FIRE™ [10] the interpolation of α_f should provide no under- and overshoots, no artificial oscillations and no excessive smearing in case of numerical diffusion near the interface. The usage of HR-schemes minimizes the deficiency of artificial effects, and it sharpens the interface by using compressing differencing schemes as discussed in the work of Waclawczyk and Koronowicz [12].

The fundamentals for both HR- differencing schemes are based on normalized variables which are introduced by Leonard [13]. In general, the normalized variable for the volume fraction $\tilde{\alpha}$ follows the rules of Eq. (2.10).

$$\tilde{\alpha} = \frac{\alpha - \alpha_U}{\alpha_A - \alpha_U} \tag{2.10}$$

The indexes U represent the upwind, A the acceptor and D the donator value. To fulfill the explanation, Eq. (2.11)-(2.12) present the normalized values needed. Where $\tilde{\alpha}_f$ denotes the normalized variable on cell face and $\tilde{\alpha}_D$ represents the normalized volume fraction for the donor cell.

$$\tilde{\alpha}_f = \frac{\alpha_f - \alpha_U}{\alpha_A - \alpha_U} \tag{2.11}$$

$$\tilde{\alpha}_D = \frac{\alpha_D - \alpha_U}{\alpha_A - \alpha_U} \tag{2.12}$$

Eq. (2.11)- (2.12) include the normalized variables for the so called convective boundedness criterion (CBC) which is based on the work from Gaskell and Lau [14]. On unstructured meshes the upwind volume fraction α_U is not known. It has to be approximated (see Eq. (2.13)) by the volume fraction gradient of the donor cell $(\nabla\alpha)_D$, and the vector $\mathbf{d}$ which represents the connection between donor and acceptor cell centers.

$$\alpha_U = \min[max(\alpha_A - 2(\nabla\alpha)_D \cdot \mathbf{d})] \tag{2.13}$$

The weighting factor β_f includes the functional relationship of the monotonic and boundedness criterion by the normalized values $\tilde{\alpha}_f$ and $\tilde{\alpha}_D$ and implicitly contains the upwind value for α_U.

$$\beta_f = \frac{\tilde{\alpha}_f - \tilde{\alpha}_D}{1 - \tilde{\alpha}_D} \tag{2.14}$$

The value for $\tilde{\alpha}_f$ comes from the selected differencing schemes which will be explained in section 2.2.1.1 for the CICSAM and section 2.2.1.2 for the HRIC scheme. After α_f (see Eq. (2.15)) is calculated it is put in Eq. (2.9) to solve the volume fraction equation.

$$\alpha_f = \left(1 - \beta_f\right)\alpha_D + \beta_f \alpha_A \tag{2.15}$$

2.2.1.1 CICSAM Differencing Scheme

To approximate the normalized value $\tilde{\alpha}_f$ the CICSAM approach provides the usage of two separate differencing schemes based on the work of Ubbink [15]. The most compressive scheme of both is called HYPER-C with the drawback of interface instability. Based on that, CICSAM is blended with a less compressive differencing scheme called ULTIMATE-QUICKEST (UQ).

The Normalized Variable Diagram (NVD) applied for the acceptor-donor scheme leads to HYPER-C (Eq. (2.16)) as presented by Leonard [13], which fulfills the convection boundedness criterion and includes downwind differencing. On the one hand the gradient of the interface is compressed in fact of downwind differencing to a step profile, this leads to one of the most compressive and sharp differencing scheme. On the other hand, this scheme suffers from artificial deformation when the interface is tangential to the flow direction. This drawback will be seen in the advection test in section 4.3.

$$\tilde{\alpha}_{f_{CBC}} = \begin{cases} \tilde{\alpha}_D & when \quad \tilde{\alpha}_D < 0, \tilde{\alpha}_D > 1 \\ min\left(1, \dfrac{\tilde{\alpha}_D}{C_D}\right) & when \quad 0 \leq \tilde{\alpha}_D \leq 1 \end{cases} \tag{2.16}$$

To overcome the artificial wrinkling of the interface, the CICSAM-scheme is blended with another differencing scheme. The ULTIMATE-QUICKEST as seen in Eq. (2.17), which is a modification of QUICK by adding the bounded criterion is less compressive but third order accurate. As presented by Leonard [13] the scheme implies good results in convection tests which was the reason why Ubbink [15] has introduced it in CICSAM.

$$\tilde{\alpha}_{f_{UQ}} = \begin{cases} \tilde{\alpha}_D & when \quad \tilde{\alpha}_D \leq 0, \tilde{\alpha}_D > 1, \\ min\left(\dfrac{8C_D\tilde{\alpha}_D + (1 - C_D)(6\tilde{\alpha}_D + 3)}{8}, \tilde{\alpha}_{f_{CBC}}\right) & when \quad 0 \leq \tilde{\alpha}_D \leq 1 \end{cases} \tag{2.17}$$

The Courant-Friedrich-Levy (CFL) number C_D of the donor cell, which occurs in both differencing schemes, is determined in Eq. (2.18) for the Finite-Volume-Method (FVM). n_f is the number of faces which bounded the donor cell, $\mathbf{A}_f$ is the face-area vector, Δt is the time step and V_D is the Volume of the donor cell. For a sharp interface the CFL-number should not exceed values of 0.5 to 0.6. Otherwise the interface tends to smearing and the calculation results becomes more and more inaccurate.

$$C_D = \sum\nolimits_f^{n_f} max\left(0, \frac{\mathbf{U}_f \cdot \mathbf{A}_f \Delta t}{V_D}\right) \tag{2.18}$$

The angle between the interface normal $\nabla\alpha$ and the face direction d_f is denoted by θ_f. It is determined in Eq.(2.19) and a graphical illustration is seen in Figure 1.

$$\theta_f = arccos\left|\frac{(\nabla\alpha)_D \cdot \mathbf{d}_f}{|(\nabla\alpha)_D|\,|\mathbf{d}_f|}\right| \tag{2.19}$$

If θ_f is known in combination with the blending exponent C_θ the weighting factor γ_f (see Eq.(2.20)) can be calculated.

$$\gamma_f = min\left(1, \cos(2\theta_f)^{C_\theta}\right) \tag{2.20}$$

After cognition of the weighting factor, the normalized face volume fraction $\tilde{\alpha}_f$ yields to Eq. (2.21). This equation is the linear combination of the two differencing schemes. When $\tilde{\alpha}_f$ is known, it is inserted in Eq. (2.15).

$$\tilde{\alpha}_f = \gamma_f \tilde{\alpha}_{f_{CBC}} + \left(1 - \gamma_f\right)\tilde{\alpha}_{f_{UQ}} \tag{2.21}$$

Special attention should be paid to blending exponent C_θ of Eq. (2.20)), this is nothing else as the seamless blending parameter which can be set by the user in the calculation settings in AVL-FIRE^{TM}. The value of C_θ involves some gates, that means if $C_\theta = 0$ the calculation is done only by the HYPER-C-scheme. Is $C_\theta \gg 1$ the main part of the calculation is done with the UQ-scheme. For $C_\theta = 2$ the simulation is done with the original CICSAM-scheme of Ubbink and Issa [15].

2.2.1.2 High Resolution Interface Capturing (HRIC) Scheme

The High Resolution Interface Capturing scheme (HRIC) was introduced in the work of Ubbink [16]. It is based on the normalized variable diagram in combination with the donor-acceptor method similar to the CICSAM scheme. The workflow for the solution includes three steps. The first step leads to specify the normalized face volume fraction $\tilde{\alpha}_f^*$ as defined in Eq. (2.22)

$$\tilde{\alpha}_f^* = \begin{cases} \tilde{\alpha}_D & when \quad \tilde{\alpha}_D < 0, \tilde{\alpha}_D > 1 \\ 2\tilde{\alpha}_D & when \quad 0 \le \tilde{\alpha}_D < 0.5 \\ 1 & when \quad 0.5 \le \tilde{\alpha}_D \le 1 \end{cases} \tag{2.22}$$

Next is the corrector step for the face volume fraction where $\tilde{\alpha}_f^{**}$ represents the corrected face volume fraction with the local CFL – number C_D

$$\tilde{\alpha}_f^{**} = \begin{cases} \tilde{\alpha}_f^* & when \quad \tilde{C}_D < C_{DL} = 0.3 \\ \tilde{\alpha}_D & when \quad \tilde{C}_D > C_{DU} = 0.7 \\ \tilde{\alpha}_D + \left(\tilde{\alpha}_f^* - \tilde{\alpha}_D\right)\dfrac{C_{DU} - C_D}{C_{DU} - C_{DL}} & when \quad C_{DL} \le \tilde{C}_D \le C_{DU} \end{cases} \tag{2.23}$$

Up next the face volume fraction $\tilde{\alpha}_f$ can be calculated and inserted in Eq. (2.15). There is also a possibility for blending in the calculation settings in AVL-FIRE^{TM}. The blending exponent is per default $C_\theta = 0.05$.

$$\tilde{\alpha}_f = \tilde{\alpha}_f^{**}\left(\cos\theta_f\right)^{C_\theta} + \tilde{\alpha}_D\left[1 - \left(\cos\theta_f\right)^{C_\theta}\right] \tag{2.24}$$

2.2.2 Governing Equations for the VOF Approach

The next section represents the governing equations for mass and momentum. They include some additional terms for coupling with the Eulerian-Eulerian approach in case of cavitating flow. First of all, the description starts with the physical meaning of the so called volume fraction α_k^{VOF}which is explained below:

$$\alpha_k^{VOF} = \begin{cases} 1 & fully\ occupied\ by\ the\ tracked\ phase \\ 0 & not\ occupied\ by\ the\ tracked\ phase \\ 0 < \alpha_k < 1 & interface \end{cases} \tag{2.25}$$

The gaseous phase ($k = g$) is totally modeled with the VOF-approach. Attention should be paid on the liquid phase $k = l$. It interacts with the gaseous and the vapor phase and has a special attention in both methods as described in the work of Edelbauer [4]. The VOF-method computes the volume fraction from Eq. (2.26) for the so called one-field formulation. Where $\mathbf{U}_m$ is the convection velocity vector of the mixture, and $S_\alpha = \Gamma_{kp}/\ \rho_k$ includes the source/sink of the volume fraction. $S_\alpha = 0$ for the gas phase and $S_\alpha \neq 0$ for liquid phase, as side note, it is mentioned that the vapor phase is only solved with the EE method.

$$\frac{\partial \alpha_k}{\partial t} + \frac{\partial}{\partial x_j}\left(\alpha_k \mathbf{U}_{m,j}\right) = S_\alpha \tag{2.26}$$

The local mixture of the fluid density ρ_m and viscosity μ_m are computed to the equations:

$$\rho_m = \frac{\alpha_l \rho_l + \alpha_g \rho_g}{\alpha_m} \qquad \mu_m = \frac{\alpha_l \mu_l + \alpha_g \mu_g}{\alpha_m} \tag{2.27}$$

The mixture volume fraction α_m amounts to the sum of the volume fraction for liquid and gas:

$$\alpha_m = \alpha_l + \alpha_g \tag{2.28}$$

If vapor is present, α_m is less than one. The balance equation for mass in the VOF approach is solved for each phase itself. A difference is observed for the momentum equation and facts by solving it for a homogenous mixture instead of a single phase. This leads to Eq. (2.29) and is extracted out of Edelbauer [4]. The terms of $\mathbf{f}_{Bm,i}$ represent the body force and its approximation is found in Eq. (2.30). The last two terms of the equation represent the interphase momentum transfer of the i-th component $M_{lv,i}$ and the interphase mass transfer Γ_{lv}. of the computation

$$\begin{aligned} \frac{\partial \alpha_m \rho_m \mathbf{U}_m}{\partial t} + \frac{\partial}{\partial x_j}\left(\alpha_m \rho_m \mathbf{U}_{m,j} \mathbf{U}_{m,i}\right) = -\alpha_m \frac{\partial p}{\partial x_i} + \frac{\partial \alpha_m \left(\boldsymbol{\tau}_{m,ij} + \boldsymbol{\tau}_{m,ij}^t\right)}{\partial x_j} \\ + \mathbf{f}_{Bm,i} + M_{lv,i} + \mathbf{U}_{lv,i} \Gamma_{lv} \end{aligned} \tag{2.29}$$

The body forces $\mathbf{f}_{Bm,i}$ contains the gravity force and the surface tension force. In general, the last force complies to the Continuum Surface Force (CSF) model and is introduced by Brackbill et al. [17]. The equation involves the gravity vector $\mathbf{g}$, the curvatur $\kappa_{l,P}$ and the surface tension coefficient σ_l.

$$\mathbf{f}_B = \frac{1}{V_P} \int_0^{V_P} \left(\alpha_m \rho_m \mathbf{g} + \sigma \kappa_l \nabla \alpha_l\right) dV \approx \alpha_m \rho_m \mathbf{g} + \sigma_l \kappa_{l,P} \kappa_l \tag{2.30}$$

The curvature of the liquid phase $\kappa_{l,P}$ is defined in the cell center P as followed in Eq.(2.31).

$$\kappa_{l,P} = -\left[\nabla \cdot \left(\frac{\nabla \alpha_l}{|\nabla \alpha_l|}\right)\right]_P \tag{2.31}$$

2.3 Coupling of the Volume-of-Fluid and the Eulerian-Eulerian Method

The motivation to solve the vapor phase with the Eulerian-Eulerian approach is to reduce numerical effort due to solve only an ensembled-averaged phase indicator function. This decreases the numerical modeling efforts to calculate the interface between liquid and vapor. Therefore, it is assumed that cavitation introduced bubbles have a smaller length scale than droplets in case of spray break up. In facts of the numerical simulation it tends to a much smaller grid size to resolve the cavitation bubbles. As described by Edelbauer [4] a coupling of two methods, will reduce the costs of the numerical simulation for a cavitating flow problem. The liquid-gas interface is solved with the VOF-method as explained in section 2.1.2. The EE-approach (see section 2.1) solves the liquid-vapor interface as seen in Edelbauer [4] and a visualization for that is presented in Figure 2. Both methods are similar, differences can be found in the interphase exchange terms. It is important to distinguish how the interface is calculated for both methods. VOF uses the one-fluid approach to solve the indicator function as described by Hirt and Nichols [9], EE solve each phase separately own and uses the ensembles averaging approach.

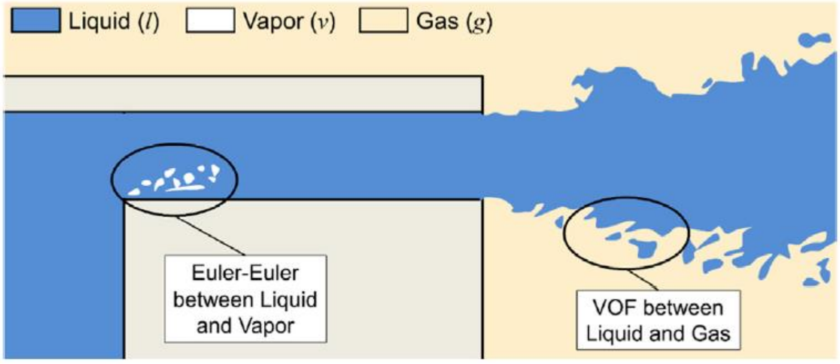

Figure 2: Illustration of the 3-phase multiphase concept for numerical simulation by Edelbauer [4].

2.4 Turbulence Modeling

In this work the turbulence effects were modeled with the Large Eddy Simulation (LES) approach. For the EE-method as well as the VOF-method, the transport equations for mass and momentum should oblige to spatial filtering in case of the turbulence effects. As mentioned in Hirsch [11] the turbulent fluctuations for large scale turbulent motion with lower frequency were directly calculated, and the small-scale fluctuations are modeled with the so called Sub-Grid Scale (SGS) model. After filtering the viscous term of the momentum equations for the EE- approach as well as for the VOF- approach, it becomes the form of Eq. (2.32).

$$\boldsymbol{\tau}_{k,ij} + \boldsymbol{\tau}^t_{k,ij} = \rho_k \nu_k \frac{\partial \bar{\mathbf{U}}_{k,i}}{\partial x_j} - \underbrace{\rho_k\left(\overline{\mathbf{U}_{k,i}\mathbf{U}_{k,j}} - \bar{\mathbf{U}}_{k,i}\bar{\mathbf{U}}_{k,j}\right)}_{\boldsymbol{\tau}^r_{k,ij}} \tag{2.32}$$

As approached from Alajbegovic [18] the viscous term is applied for both multiphase methods (EE and VOF-method) and the term $\boldsymbol{\tau}^r_{k,ij}$ denotes the SGS tensor. It is often called residual stress tensor which is modeled by an eddy viscosity model, and customary by the Samgorinsky model [19]. The SGS-filtered properties are indicated by an overbar. Eq. (2.33) shows the correlation of the SGS tensor, the filtered strain rate tensor $\bar{\mathbf{S}}_{k,ij}$ and the eddy viscosity ν^t_k.

$$\boldsymbol{\tau}^r_{k,ij} - \frac{1}{3}\boldsymbol{\tau}_{k,ii}\delta_{ij} = \rho_k \nu^t_k \underbrace{\left(\frac{\partial \bar{\mathbf{U}}_{k,i}}{\partial x_j} + \frac{\partial \bar{\mathbf{U}}_{k,j}}{\partial x_i}\right)}_{2\bar{\mathbf{S}}_{k,ij}} = 2\rho_k \nu^t_k \bar{\mathbf{S}}_{k,ij} \tag{2.33}$$

To calculate the eddy viscosity ν^t_k (Eq. (2.34)) with the Smagorinsky model, a coefficient which depends on the flow regime, the so called Smagorinsky coefficient C_S has to be defined.

$$\nu^t_k = (C_S\Delta)^2|\bar{\mathbf{S}}_k| \tag{2.34}$$

Term Δ is the filter length as a function of the cell volume V as described by the equation:

$$\Delta = V^{1/3} \tag{2.35}$$

The resolved strain rate tensor $\bar{\mathbf{S}}_k$ depends on $\bar{\mathbf{S}}_{k,ij}$ as described in Eq. (2.36).

$$\bar{\mathbf{S}}_k = \left(2\bar{\mathbf{S}}_{k,ij}\bar{\mathbf{S}}_{k,ij}\right)^{1/2} \tag{2.36}$$

Kobayashi [20] proposed the so called Coherent Structure Model (CSM), where parameter C_S is not constant anymore. Instead a local value C is expressed by the Eq. (2.37).

$$C = C_{CSM}|\mathbf{F}_{CS}|^{\frac{3}{2}}\mathbf{F}_{\Omega} \tag{2.37}$$

C_{CSM} is a fixed model parameter (see Eq. (2.38)).

$$C_{CSM} = \frac{1}{22} \tag{2.38}$$

The coherence structure function $\mathbf{F}_{CS}$ (Eq. (2.41)) corresponds to the second invariant of the velocity gradient tensor $\mathbf{Q}_k$ (Eq.(2.39)), and is normalized by the magnitude of the velocity gradient tensor $\mathbf{E}_k$ (Eq. (2.40)). The tensor of the resolved flow field $\bar{\mathbf{W}}_{k,ij}$ is the vorticity.

$$\mathbf{Q}_k = \frac{1}{2}\left(\bar{\mathbf{W}}_{k,ij}\bar{\boldsymbol{W}}_{k,ij} - \bar{\mathbf{S}}_{k,ij}\bar{\mathbf{S}}_{k,ij}\right) = -\frac{1}{2}\frac{\partial \bar{\mathbf{U}}_{k,j}}{\partial x_i}\frac{\partial \bar{\mathbf{U}}_{k,i}}{\partial x_j} \tag{2.39}$$

$$\mathbf{E}_k = \frac{1}{2}\left(\bar{\mathbf{W}}_{k,ij}\bar{\mathbf{W}}_{k,ij} + \bar{\boldsymbol{S}}_{k,ij}\bar{\boldsymbol{S}}_{k,ij}\right) = \frac{1}{2}\left(\frac{\partial \bar{\mathbf{U}}_{k,j}}{\partial x_i}\right)^2 \tag{2.40}$$

$$F_{CS} = \frac{\mathbf{Q}_k}{\mathbf{E}_k} = \frac{\frac{1}{2}\left(\bar{\mathbf{W}}_{k,ij}\bar{\mathbf{W}}_{k,ij} - \bar{\boldsymbol{S}}_{k,ij}\bar{\boldsymbol{S}}_{k,ij}\right)}{\frac{1}{2}\left(\bar{\mathbf{W}}_{k,ij}\bar{\mathbf{W}}_{k,ij} + \bar{\boldsymbol{S}}_{k,ij}\bar{\boldsymbol{S}}_{k,ij}\right)} = \frac{-\frac{1}{2}\frac{\partial \bar{\mathbf{U}}_{k,j}}{\partial x_i}\frac{\partial \bar{\mathbf{U}}_{k,i}}{\partial x_j}}{\frac{1}{2}\left(\frac{\partial \bar{\mathbf{U}}_{k,j}}{\partial x_i}\right)^2} \tag{2.41}$$

The energy decay suppression function F_Ω (Eq. (2.42)) and F_{CS} are bounded through their upper and lower limits as seen in the following manner:

$$F_\Omega = 1 - F_{CS} \tag{2.42}$$

$$-1 \le F_{CS} \le 1 \; and \; 0 \le F_\Omega \le 2 \tag{2.43}$$

Finally, the eddy viscosity is calculated in the following manner of Eq. (2.44)

$$\nu_k^t = C\Delta^2|\bar{\mathbf{S}}_k| \tag{2.44}$$

Note that the C and C_S are always positive and limited as shown below.

$$0 \le C \le 0.05 \; and \; 0 \le C_S = \sqrt{C} \le 0.22 \tag{2.45}$$

The benefit of the CSM is its robustness in fact of the boundedness as seen in Eq. (2.45)).

2.5 Theory for Particle Length Detection

This section includes the theory for particle length detection followed to the heading of mechanical engineering. Most of the equations are based on the book of Parkus [21]. The explanation starts with the moments of inertia for an arbitrary point followed by the tensor of inertia. The Steiner`s theorem is also required to calculate the main moments of inertia. To get the ligament lengths, the direction vectors of the main moments of inertia should be calculated. The vectors lead afterwards to the ligaments lengths with a computational algorithm which is explained in section 3.

2.5.1 Inertia Tensor for an Arbitrary Mass Point

Up next the chronological order starts with the mass moments of inertia (I_ξ, I_η, I_ζ) as written in Eq.(2.46) below for the three-coordinate axis separately. The indices ξ, η and ζ represents the three axis of the coordinates for an arbitrary point A which are parallel to the axis of the coordinate system in the center of gravity (point S) as seen in Figure 3. The dimensions a, b and c are the distances from the center of gravity to point A with mass m_A.

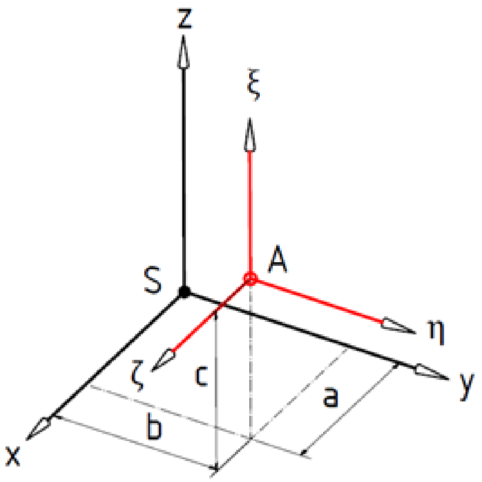

Figure 3: Visualization of the coordinate axis for an arbitrary mass point A (Parkus [21]).

$$
\begin{aligned}
I_\xi &= (\eta^2 + \zeta^2) m_A \\
\mathrm{I}_\eta &= (\xi^2 + \zeta^2) \mathrm{m_A} \\
\mathrm{I}_\zeta &= (\xi^2 + \eta^2) \mathrm{m_A}
\end{aligned}
\tag{2.46}
$$

The descriptive literature on engineering mechanics shows that there are some differences between the notations of the product of inertia. Kessel [22] describes that in English literature the product of inertia has a positive sign. In German literature, the product of inertia often has a negative sign as described in Dankert et al. [23]. For this work the notation of Parkus [21], with a positive sign is used, and this leads to the products of inertia ($I_{\xi\eta}$, $I_{\eta\zeta}$, $I_{\zeta\xi}$) as seen in Eq. (2.47).

$$
\begin{aligned}
I_{\xi\eta} &= I_{\eta\xi} = \xi\eta \ \mathrm{m_A} \\
I_{\eta\zeta} &= I_{\zeta\eta} = \eta\zeta \ \mathrm{m_A} \\
I_{\zeta\xi} &= I_{\xi\zeta} = \zeta\xi \ \mathrm{m_A}
\end{aligned}
\tag{2.47}
$$

Once the main moments and the products of inertia for an arbitrary point are known for all coordinate axis, a tensor of inertia with respect to an arbitrary point $\mathrm{I}_{\xi\eta\zeta}$ can be defined in (see Eq. (2.48)). The main moments of inertia are located on the main diagonal, and the products of inertia are placed on the off diagonal elements. Note, this tensor is symmetric.

$$
\mathrm{I}_{\xi\eta\zeta} = \begin{bmatrix} \mathrm{I}_\xi & I_{\xi\eta} & I_{\xi\zeta} \\ I_{\xi\eta} & \mathrm{I}_\eta & I_{\zeta\eta} \\ I_{\xi\zeta} & I_{\eta\zeta} & \mathrm{I}_\zeta \end{bmatrix}
\tag{2.48}
$$

2.5.2 Inertia Tensor for Center of Gravity

The same procedure as determined in section 2.5.1 to calculate the inertia tensor of an arbitrary point can be performed for the inertia tensor in the center of gravity. Instead of the length of a, b, and c from Figure 3, the variables x, y, and z will be used now. They represent the lengths from origin (point 0) to the center of gravity (point S) of a particle, see Figure 4.

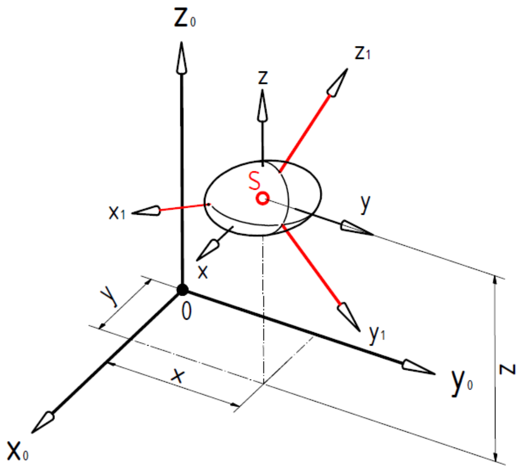

Figure 4: Visualization of the coordinate axis for center of gravity.

Now the moments of inertia (I_x, I_y, I_z) are described with respect to the center of gravity, as written in Eq. (2.49).

$$I_x = \int_m (y^2 + z^2)dm$$
$$I_y = \int_m (z^2 + x^2)dm \tag{2.49}$$
$$I_z = \int_m (x^2 + y^2)dm$$

The same procedure as seen in the section before the products of inertia in the center of gravity (I_{xy}, I_{yz}, I_{zx}) followed in Eq. (2.50).

$$I_{xy} = I_{yx} = \int_m xy\,dm$$
$$I_{yz} = I_{zy} = \int_m yz\,dm \tag{2.50}$$
$$I_{zx} = I_{xz} = \int_m zx\,dm$$

After the calculation for each axis, the inertia tensor I_{xyz} for the center of gravity is defined by the following equation.

$$\mathrm{I_{xyz}} = \begin{bmatrix} \mathrm{I_x} & I_{xy} & I_{xz} \\ I_{xy} & \mathrm{I_y} & I_{yz} \\ I_{xz} & I_{yz} & \mathrm{I_z} \end{bmatrix} \tag{2.51}$$

2.5.3 Steiner’s Theorem

Belong to the fact that the mass moment of inertia is known in the center of gravity, the Steiner’s theorem is used to calculate the mass moment of inertia for an arbitrary point. A detailed explanation was found in the book of Dankert [23]. To use Steiner’s theorem following coordinate transformation is applied

$$\mathrm{x = a + \xi;\ y = b + \eta;\ z = c + \zeta;} \tag{2.52}$$

and inserted in the Eq. (2.46) in section 2.5.1. The expression, only presented for I_ξ yields:

$$\begin{aligned} \mathrm{I}_\xi = \int_m (\eta^2 + \zeta^2)\mathrm{dm} &= \int_m (\,(\mathrm{y-b})^2 + (\mathrm{z-c})^2\,)\mathrm{dm} \\ &= \mathrm{I_x} + (b^2 + c^2)m - 2b\int_m \mathrm{ydm} - 2c\int_m \mathrm{zdm} \end{aligned} \tag{2.53}$$

In the center of gravity x, y and z become zero, and the equation reduces to:

$$\begin{aligned} \mathrm{I}_\xi &= \mathrm{I_x} + (b^2 + c^2)\,m \\ \mathrm{I}_\eta &= \mathrm{I_y} + (a^2 + c^2)\,m \\ \mathrm{I}_\zeta &= \mathrm{I_z} + (a^2 + b^2)\,m \end{aligned} \tag{2.54}$$

The same procedure can be done for the mass product of inertia leading to:

$$\begin{aligned} I_{\xi\eta} &= I_{\eta\xi} = \mathrm{I_{xy}} + abm \\ I_{\eta\zeta} &= I_{\zeta\eta} = \mathrm{I_{yz}} + \mathrm{bcm} \\ I_{\zeta\xi} &= I_{\xi\zeta} = \mathrm{I_{zx}} + cam \end{aligned} \tag{2.55}$$

With the Eq. (2.54) and (2.55) the inertia tensor $\mathrm{I}_{\zeta\eta\xi}$ for an arbitrary point yields.

$$\mathrm{I}_{\zeta\eta\xi} = \begin{bmatrix} \mathrm{I_x} & I_{xy} & I_{xz} \\ I_{xy} & \mathrm{I_y} & I_{yz} \\ I_{xz} & I_{yz} & \mathrm{I_z} \end{bmatrix} + m \begin{bmatrix} (b^2 + c^2) & ab & ca \\ ab & (a^2 + c^2) & \mathrm{bc} \\ ca & \mathrm{bc} & (a^2 + b^2) \end{bmatrix} \tag{2.56}$$

2.5.4 Eigenvalues and Eigenvectors

To solve the eigenvalues and eigenvectors problem, Eq. (2.56) is reformulated in a way where the inertia tensor for the center of gravity stands on the right-hand side as seen below.

$$\mathrm{I_{xyz}} = \mathrm{I_{\zeta\eta\xi}} - m\begin{bmatrix} (b^2+c^2) & ab & ca \\ ab & (a^2+c^2) & \mathrm{bc} \\ ca & \mathrm{bc} & (a^2+b^2) \end{bmatrix} \tag{2.57}$$

In the next step the determinate of the outlined tensor above is calculated, which leads to an equation of cubic form. Hence Eq.(2.58) yields the eigenvalues λ_i, and after solving (Bartsch [24]) they represents the principal moments of inertia. The solutions of them are always real because the determinant of the tensor Eq.(2.57) is symmetric as described in Parkus [21].

$$\lambda^3 + u\,\lambda^2 + v\,\lambda + w = 0 \tag{2.58}$$

To get the directions of the principal moments of inertia, the eigenvectors have to be known. In the book of Bartsch [24] a simple explanation is shown how these eigenvectors x_i can be determined. After solving the linear equation system, the three eigenvectors and the directions of the principal moments of inertia are known.

$$\left(\mathrm{I_{xyz}} - \lambda_i\,\mathbf{E}\right) x_i = 0 \tag{2.59}$$

2.6 Liquid Jet Break-Up

To evaluate liquid jet break-up the specialist literature presents some techniques to categorize these mechanism, a short summary is given in the next section.

2.6.1 Dimensionless Numbers for Spray Characterization

To categorize the break-up regime some dimensionless numbers are needed to know. First the Reynolds number Re_l is determined with the characteristic length for the nozzle diameter D.

$$Re_l = \frac{\rho_L U_L D}{\mu_L} \tag{2.60}$$

The liquid Weber number is defined as

$$We_l = \rho_L \frac{{U_L}^2 D}{\sigma} \tag{2.61}$$

U_L is the jet velocity ρ_L is the liquid density, μ_l is the dynamic viscosity and σ is the surface tension coefficient. The Ohnesorge number is related from the Reynolds number and the liquid Weber number as described by:

$$Oh = \frac{\sqrt{We_l}}{Re_l} = \frac{\mu_l}{\sqrt{\sigma \rho_l D}} \tag{2.62}$$

2.6.2 Break-Up Regimes

Based on the work of Ohnesorge [25], a classification of the different main break-up regimes can be found at Lefebvre [26]. A short summary of the four regimes is shown here. Once, the Ohnesorge and the Reynolds number are calculated, the break-up is classified in Figure 5.

Regime 1. - Rayleigh mechanism

- ⇨ Oscillations in the jet surface lead to break-up induced by surface tension forces with droplets diameters which are bigger then the jet diameter.

Regime 2. - First wind-induced regime

- ⇨ The relative velocity of the jet and the ambient gas increases the surface tension effect. Across the jet, a static pressure distribution is observed and accelerating surface grow to waves break-up with droplets sizes which are in the order of the jet diameter.

Regime 3. - Second wind-induced regime

- ⇨ The jet surface includes surface waves which grow unstable with short-wavelength. The relative motion of jet and ambient gas proceeds the break-up to droplets which have an averaged value smaller than the jet diameter.

Regime 4. Atomization regime

- ⇨ The atomization break-up starts directly at the nozzle outlet, and the averaged droplet diameters are much smaller than the jet diameter.

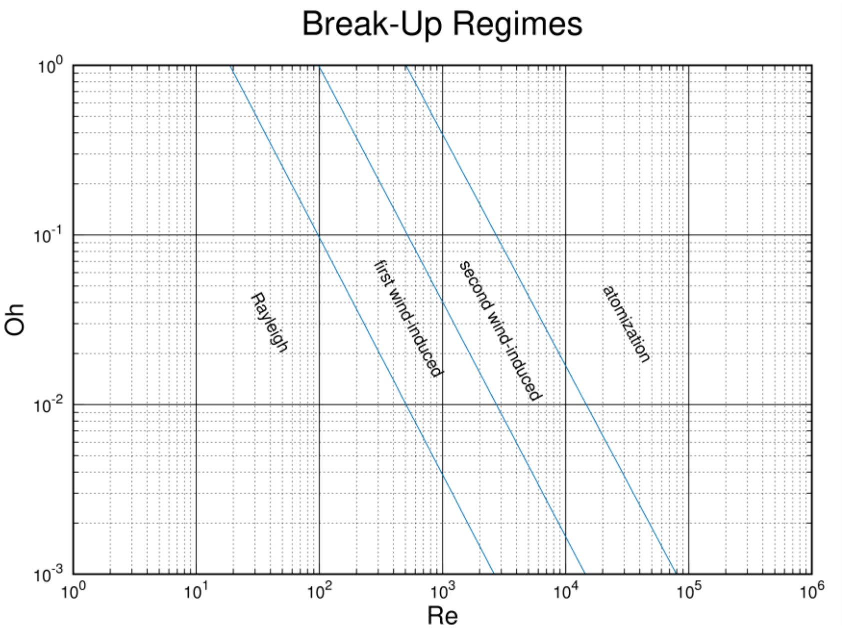

Figure 5: Ohnesorge monogram sharing different break-up regimens (figure reproduced from Reitz and Braco [27]).

Another classification for primary break-up mechanism can be found as summary in the work of Baumgarten [28]. He gives an overview of the mechanism in aerodynamical induced break-up which is induced by the relative motion of the liquid and the ambient gas. Turbulence effects from the flow field inside the injector creates bulges on the jet surface after the fluid streams out. The last presented mechanism sourced from cavitation effects inside the nozzle and all three primary break-up mechanism will be seen in Figure 6.

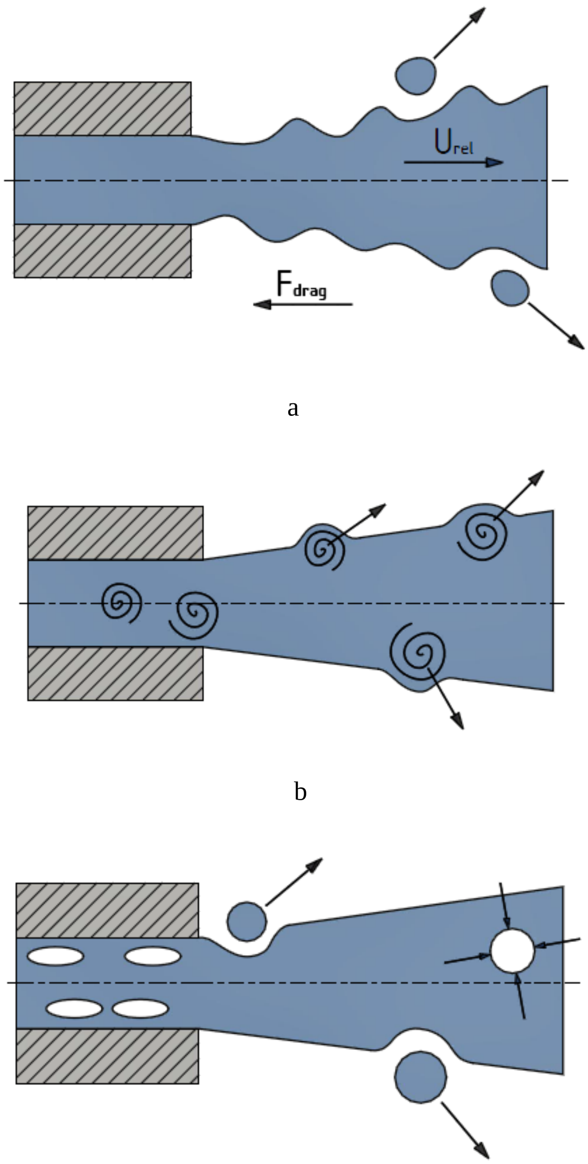

a

b

c

Figure 6: Visualization of primary break-up mechanisms. a) aerodynamical induced b) turbulent induced c) cavitation induced (figures reproduced from Som and Aggarwal [29]).

2.7 Cavitation

In general cavitation takes place in flow regions where the local pressure is lower than the saturation pressure. This is observed in flow regions with high liquid velocity like near edges or in the outer of vortexes. After dropping the saturation pressure the liquid will change his phase to vapor. Bubble Collapses downstream accelerate the jet break-up. The differentiation of cavity effects was adopted from Leick [30], and will be shortly presented up next.

Homogenous Cavitation

- ⇨ The homogeneous cavitation or bubble cavitation occurs during the static pressure drop and leads to cavitation bubbles in a homogenous two phase mixture. The bubbles have their origin on cavitation nucleis in the liquid.

Heterogenous Cavitation

- ⇨ The regions of cavitation will be observed as continuous films which have their origins in the flow domain near walls and edges. Their nucleis are induced by surface effects like wall roughness. It is often seen in devices like fuel injectors where the nucleis at the walls have more influence on the cavitation growth than nucleis in the flow domain. In injectors for diesel engines it was seamless observed that the cavitation film is stretched over the nozzle hole up to the injector orifice. This phenomenon is often called Supercavitation.

Vortex Cavitation

- ⇨ In swirls, regions with low static pressure in vortex centers can be observed. The long and stretched form gives this cavitation type the name “String Cavitation”. Its high graded instability origins from stochastic nature.

3 New Algorithm for Particle Analysis

The main topic of this thesis was to introduce a tool for particle length detection from a Volume-of-Fluid simulation of liquid break-up. In combination with the particle length detection a graphical scheme was introduced for verification of the particle shape as seen in section 3.2. After this it was necessary to test the correct implementation of the algorithm. Additionally, two differencing schemes have been verified. To overcome this large set of test cases and to give a meaningful statement, an enhanced technique for the testing process was introduced (see section 3.3).

3.1 Particle Lengths Detection

In this section the new introduced tool for particle length detection is explained. Furthermore, a tool for quantification of the particle shape, the particle form diagram, and a new method to evaluate multiphase schemes are presented.

3.1.1 Original Implementation in AVL-FIRE^{TM}

In multiphase VOF calculations, the dimensions and shapes of particles like the diameters of droplets in injector flows are of particular interest. To excite the example of the injector flow, the breakup of the liquid core followed by the droplet formation is a topic of interest for engineers. To make a statement of droplets sizes or their distribution it is necessary to know their volumes and dimensions. Before this thesis was done the multiphase module in AVL-FIRE^{TM} was only able to calculate the particle volume. After this was known, a volume-equivalent Sauter Mean Diameter (SMD), see Sauter [31] was determined. With the new implementation of the ligament length detection the postprocessing of multiphase simulations gains on profit. Now it is possible to get information about the particles dimensions directly. Nevertheless, the estimation of the SMD is also important. In general, numerical simulations are compared with experiments, and their droplets and distributions are often evaluated with the SMD or other characteristic mean diameters.

In numerical multiphase simulations, the shape distribution of particles is a common question. This is now possible with the introduced particle form diagram which is presented in section 3.2. This diagram applies the quantified shape of the particles and categorizes the form. It is common knowledge, that VOF simulations are expensive in term of numerical effort. On large simulation cases, where the spray break-up produces spherical particle, the numerical effort will be reduced by switching to another numerical method. Therefore, the Lagrange approach as described in [10], provides an obvious solution. To use this method, the distribution and size of the droplets must be known. With the relations of the ligaments dimensions, which are the core of the form diagram, and a simple calculation of the distribution, it is now possible to decide the best timing to switch between the VOF- and Lagrange method. This is not yet implemented, but it could be a benefit for the simulations in AVL-FIRE^{TM}.

3.1.2 Enhancements of the Particle Length Detection Algorithm

First, the volume fraction for each mesh cell as described in section 2 has to be calculated. The code detects cells with the equal volume fraction and identifies if they are connected to each other or not. The algorithm itself is not limited for detection of one ligament, it will work for a big set of ligaments too, and it can be used for multi-core simulations.

After the detection of the coherent liquid structures, the algorithm is able to do for what it was made, namely to calculate lengths of the numerically simulated particles. Some techniques from engineering mechanics as explained in section 2.5, are used to compute the ligaments length. A simplification was done for the calculation of the mass tensor of inertia. A fluid can change its shape continuously and normally it will not follow the law of solid mechanics. For particle length detection, the fluid is quasi-frozen at the time step of ligament detection. So, it is possible to do calculations similar as for a solid body. The code is not limited to the VOF-method, it is also working with the EE-Framework too. A detailed step by step explanation for these procedure is found in the following section.

3.1.2.1 Numerical Procedure

The following steps describe the algorithm for a single particle. Of course, the code can deal with a large number of particles, as seen later in the real case study. The size of the fluid particle is bigger than the size of a mesh cell.

Step 1

- ⇨ Calculate the volume fraction field of the particle as described in section 2.

Step 2

- ⇨ Calculate the inertia tensors with respect of an arbitrary point for the coordinates in the origin of the numerical mesh (see point 0 in Figure 7) for all mesh cells of the particle.

Step 3

- ⇨ Sum up the inertia tensors overall cells and over all MPI-domains to get the tensor ($\mathrm{I}_{\xi\eta\zeta}$ see Eq. (2.48)) of the whole particle.

Step 4

- ⇨ Apply Steiner's Theorem as described in section 2.5.3, to calculate the tensor of inertia ($\mathrm{I}_{\mathrm{xyz}}$) with respect to the center of gravity parallel to the axes x_0, y_0, z_0.

Step 5

- ⇨ Calculate the eigenvalues (Eq. (2.58)) and eigenvectors (Eq. (2.59)) of tensor of inertia ($\mathrm{I}_{\mathrm{xyz}}$) in the center of gravity. The implementation is correct, when the axes of the mass centroid are orthogonal.

Step 6

- ⇨ Calculate for all cells the distance vector between center of gravity and cell center.

Step 7

- ⇨ Calculate the dot products between the main axes of inertia and the distance vector from step 6. The maximum value is the length of the ligament in direction of the mass centroid vectors.

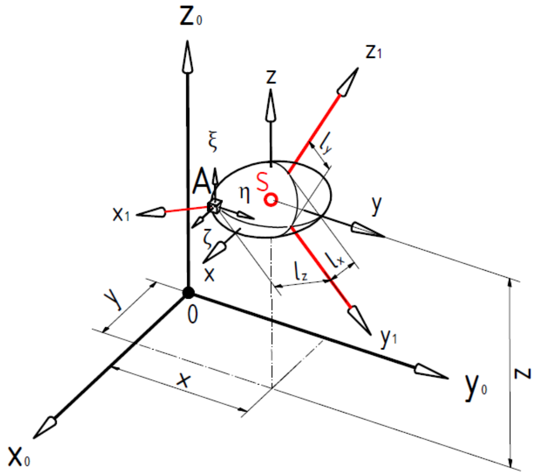

Figure 7: Graphical illustration of the particle length detection.

3.2 Particle Form Diagram

To illustrate the particles shape distribution, the particle form diagram was introduced. The idea to classify the shape of the particles in that manner was proposed by Walz [32] where particles shapes are sub-divided in different regions, as seen in Figure 8.

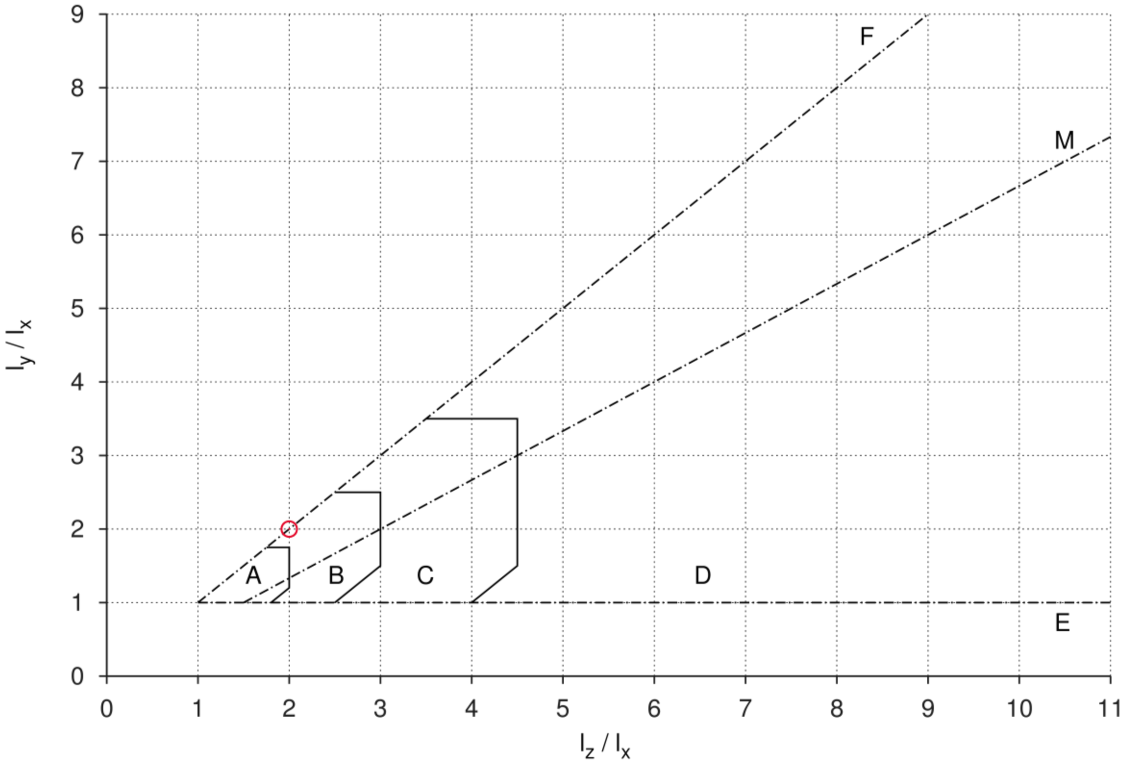

Figure 8: Particle form diagram for different shapes. Figure reproduced from Stieß [33].

To categorize the particles shape, the main measurements have to be known. Therefore, the procedure described in section 3.1 have to be performed. Then, the main measurements of particles (see Figure 7) have to be sorted in a way where $l_z \geq l_y \geq l_x$ with l_Z is the biggest, l_y is the intermediate and l_x the smallest ligament dimension. The ratio on the vertical diagram bar is defined by the ratio l_y/l_x . The horizontal bar includes the ratio l_y/l_x . The intersection of both ratios is now the indicator of the ligament shape as presented in Figure 8 with a colored red cycle. The classifications of the particle shapes are listed in Table 3-1. The regions in the first column, the description of the region in the second column.

Table 3-1: Classification of ligaments shape.

Region	**Ligaments Shape**
S	Spherical or regularly shaped bodies
F	Flat ligaments: two main dimensions have the same length the third is much smaller than the others
E	Elongated ligaments: two main dimensions have the same length, the third is much bigger than the others
A	Globular shape
B	Deviation from spherical shape
C	Flat and elongated ligaments
D	Remarkably flat and elongated ligaments

3.2.1 Usage and Forecast of further Applications

With the particle form diagram, it is now possible to get information about the ligaments shape and to categorize them, as explained in Table 3-1. This is helpful for real case multiphase simulations to get information about the particle shape distribution. In Figure 8 a particle with the ratio-coordinates 2/2 is marked by a red circle. In a real multiphase case investigation, there will be a big set of different particle shapes. As mentioned before there exists the possibility for a coupling between the VOF- and the Lagrangian method.

3.3 Development of Enhanced Testing Process

The aim of the tests was to evaluate the CICSAM and HRIC differencing scheme. With the new introduced algorithm for particle analysis, the evaluation was done for the main moments of inertia over a large number of time steps. In combination with evaluated mass conservation it was possible to show the advantages and disadvantages of both differencing schemes. To ensure these enhanced testing requirements, more than seventy test cases were calculated with the CFD-code AVL-FIRE^{TM}. To evaluate this large number a technique for evaluation of test cases was introduced. The main purpose of this evaluation technique is to get the information out of a big set of test cases. It is a matter of common knowledge that a comprehensive documentation is often neglected. To overcome this fact in this thesis a standardized approach was introduced as seen in Figure 9. Up next the steps for evaluation will be explained. Each section of the testing environment includes a table with a set of characterized values. These tables contain solutions or settings and confirm the evaluation of a test case. A short explanation for each table complements the information out of them. Up next the content of Figure 9 will be explained.

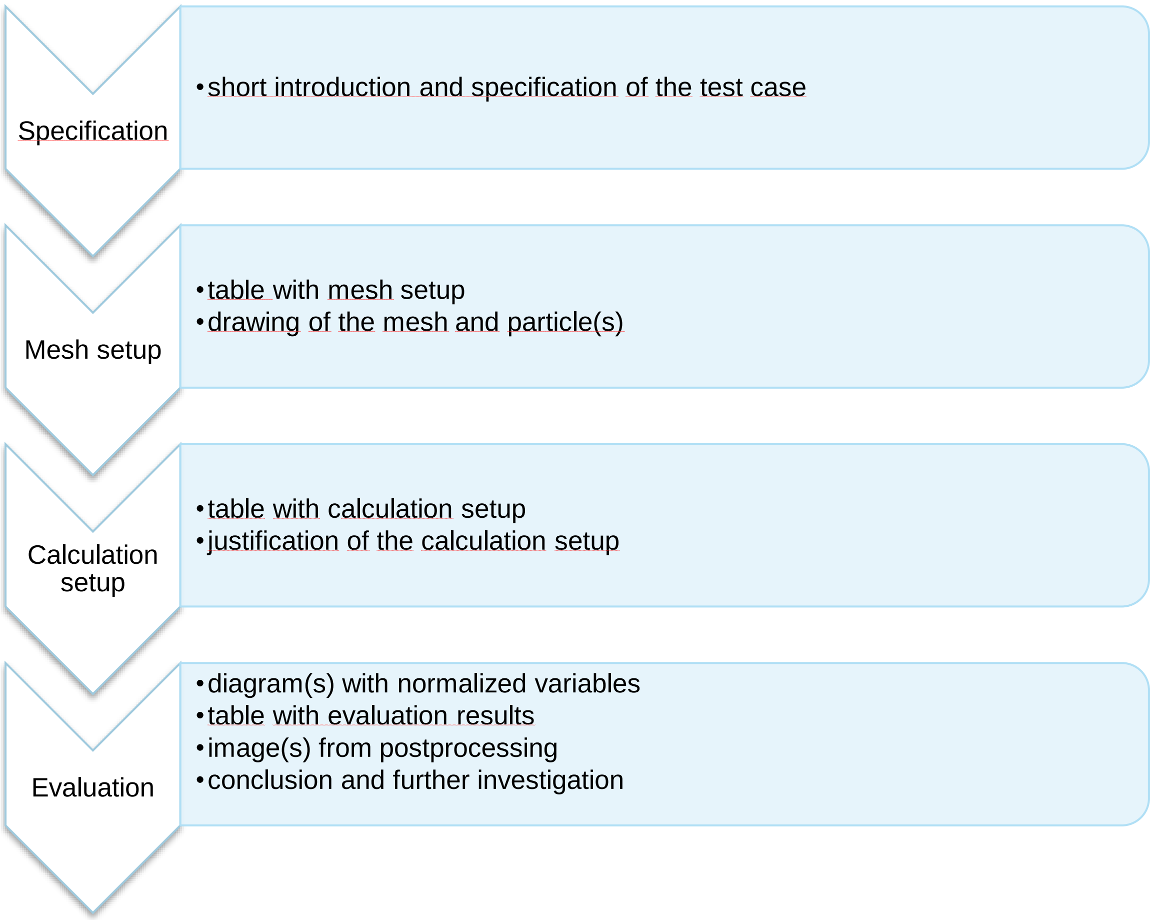

Figure 9: Standardized approach for evaluating a test case.

3.3.1 Standardized Approach for Setup

In the specification part an introduction of the case is included, and the characteristics should be presented. Also, a statement why the test case is chosen has to be written. For a better overview the mesh setup includes two parts, first a table for mesh setup (see Table 4-1) is introduced. It includes the number of cells, cell shape, minimum cell size and other mesh relevant settings. The second part contains the mesh geometry as seen in Figure 12. Test cases can be performed for single particles (see Figure 12) or a cloud of particles (see Figure 13).

Many settings for the calculation setup can be modified in AVL-FIRE^{TM}. In papers, which are dealing with multiphase simulations, it is rare that detailed information is given which settings are selected for solution finding. Regrettably multiphase schemes are sensitive for different settings, and in case of spray break-up as seen in section 5, the breakup has different shapes by variation of the calculation settings. This circumstance applies to simple convection tests too. A trustworthy evaluation should be presenting the settings in detail. In this thesis special attention was paid on the specification of the calculations settings, and they are presented tabularly in Table 8-1. A short statement about the reason for a calculation set-up should be also included.

3.3.2 Evaluation

The evaluation of a test case can be stripped in two parts. At first the initial values are calculated. It is important to keep the error at initialization small. Is the solution of the sought-for values found, the normalized variable diagram is plotted over a set of time steps. Therefore, the amount of the main moments of inertia and mass are normalized, as described in section 3.3.2.1. With the normalization process, the minimum and maximum values and the errors are known. The mesh initialization error and error from particle tracking are presented separately. This procedure is not part of the postprocess in AVL-FIRE^{TM} and is created in a separately algorithm which was introduced especially for this thesis. After this procedure, a statement is worked out and an assessment justified in a mathematical manner will be done.

3.3.2.1 Normalized Variable Diagram for Evaluated Values

During implementation and testing it turned out that it is more reasonable to compare normalized values as described in section 3.3.2.1. The benefit of this way is to compare values which do not have the same scale. For example, the main moments of inertia at the different axes range with a factor of ten, hundred or higher. With the normalized variables, the scale factor is eliminated and the main moments of inertia can be plotted easily into the same diagram (see Figure 8) or can be compared directly. Additionally, the error in percent can be evaluated directly, which determines a further benefit of this method.

For example, the normalized moments of inertia for the three main axes are plotted over time. The normalized analytical solution is unity for all axes, which demands on the definition of Eq. (3.1). This is the benchmark for the correctness of the numerical solution of the evaluated values.

With the new introduced particle length detection tool, it is now possible to get the particle length out of a numerical multiphase simulation. This is not the only great advantage, also the main moments of inertia as described in section 2.5 are calculated before. The comparison of the numerical with the analytical solution determines the quality of the numerical scheme. In the past, the evaluation was mostly done visually by comparing graphical representation delivered by the post processing. For an independent assessment, it is customary to compare normalized values. For the evaluation of the particles shapes, this mathematical procedure was done as described below.

$$I_n^{norm} = \frac{I_n^{num}}{I_n^{an}} \quad for \quad n = 1,2,3 \tag{3.1}$$

I_n^{norm} represents the normalized value of the calculated main mass moment of inertia and index n indicates the three-coordinate axes in the center of gravity. I_n^{an} is the analytical solution, and I_n^{num} represents the numerical main mass moment of inertia. After these simple calculations, the normalized values for each time step are drawn into the normalized variable diagram for main moments of inertia over time. The same procedure is performed for the mass.

3.3.2.2 Evaluation Table

All tests were done over several time steps. To get the minimum or maximum values, the solutions over all time steps were collected in one output file. Out of these set of solutions the minimum and maximum values for the main moments of inertias were filtered separately for all three axes, and the same procedure was done with the ligaments mass. It might be possible that the time step is not the same for all evaluated values in the so called table of evaluation. This is no problem, because in combination with the normalized variable diagram for the main moment of inertia (Figure 14) the time step can discern easily.

The first part of Table 8-4 is called *Initialization* and includes normalized values at the initialization step. It is evident that, when the particle is introduced by the meshing process, a difference between theoretical and numerical evaluated values occurs. This difference origins from the facts that the computed mesh cannot follow exactly the ligament shape. In Figure 10 this can be seen in detail by comparing two mesh resolutions. To reduce the error, it is recommended to reduce the cell size in order to follow the ideal particle shape with more accuracy. The index n $(n = 1,2,3)$ indicates the direction index for the main moments of inertia. Where $I_{\mathrm{n}\,in}^{norm}$ is the initial main moment of inertia for each axe, and m_{in}^{norm} includes the ligaments mass for the initialization step.

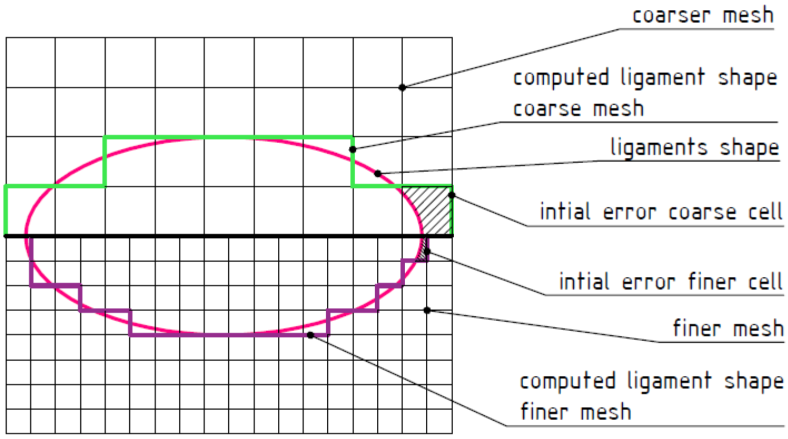

Figure 10: Comparison between idealized and numerically initialized particle shape: upper part includes a coarse mesh; lower part a fine mesh.

The second part of the evaluation table, is called *Normalized Values for Maximum and Minimum* and represents the normalized values for the main moments of inertia and the mass over all time steps. $I_{\mathrm{n}\,max}^{norm}$ stands for the maximal normalized main moment of inertia, and $I_{\mathrm{n}\,min}^{norm}$ is the minimum. Also, the normalized maximum mass m_{max}^{norm} and the normalized minimum mass $m_{min}^{norm}$are shown.

The third part is called *Loss of Accuracy* and includes the error of the calculation with respect to the analytical solution. $I_{\mathrm{n}\,max}^{er} = 1 - I_{\mathrm{n}\,min}^{norm}$. Where $I_{\mathrm{n}\,max}^{er}$ represents the maximum error, which is the difference between one and conforms to the normalized analytical solution and the smallest calculated main moment of inertia ($I_{\mathrm{n}\,min}^{norm}$). For the mass the same procedure is applied.

3.3.3 Conclusion of the Enhanced Testing Process

With this by the author introduced testing technique a faster documentation is provided. The procedure leads to a better overview, because it is possible to test a big set of cases parallel, as seen e.g. in Table 8-3 and the appendix. In combination with the summary of the calculation and mesh settings, the quality and reproduction is guaranteed too. The evaluation of the error against the analytical solution delivers a meaningful quantitative statement, which can be used to evaluate a numerical method, i.e. the differencing schemes.

4 Basic Test Cases

This chapter starts with the testing of the coded algorithm of the particle length detection followed by the evaluation of the CICSAM and HRIC differencing schemes. The test cases are formed in simple advection tests, as seen in Ubbink [15] or Zalesak [34]. The velocity direction includes translatory and rotatory motion. The mesh dependency was tested, and issues for the different schemes will be discussed next. As mentioned in section 2.2.1 the CICSAM and the HRIC differencing schemes belong both to the HR-schemes. One part of this thesis is to work out their limits. Therefore, new tools as presented in chapter 3 were developed by the author to calculate the main moments of inertia, as seen in section 3.1 above. To give meaningful statements, it is necessary to compare the calculated moments of inertia from a numerical simulation with the analytical one. The convection tests for two phases confirm the correct solution of Eq. (2.8), which represents the governing equation for the volume fraction in the VOF- model, here repeated as:

$$\frac{\partial \alpha_k}{\partial t} + \frac{\partial}{\partial x_j}\left(\alpha_k \mathbf{U}_{m,j}\right) = 0 \tag{4.1}$$

Where α denotes the volume fraction, t describes the time and $\mathbf{U}$ is the velocity field vector. The following test cases provide the setup for the industrial case, called gasoline injector (see chapter 5), to ensure highest results with the CFD-code AVL-FIRE$^{\mathrm{TM}}$. The cases will follow the introduced evaluation technique from section 3.3.

4.1 Plausibility of the Numerical Implementation

The main tasks of the test case in this section is to evaluate the implemented algorithm for particle length detection. To proof the correctness of the code the algorithm was tested step by step. A good analytical example was found in the book of Dankert [23]. The shape of the particle has not a symmetrical or a rounded form, it is a composition of two hexahedrons which are in contact to form a particle with sharp edges (see Figure 11). In that case, also the artificial behavior of sharped edges is tested. In a common multiphase simulation like an injector flow the ligaments will not have this kind of shape. The test case shows that the code can handle ligaments of arbitrary shape. This is demonstrated by comparison of the main moments of inertia which fit sufficiently to the analytical solution. With an improved setup, the accuracy can be increased. The next part describes the numerical solution procedure, where the meshing setup followed by the calculation setup.

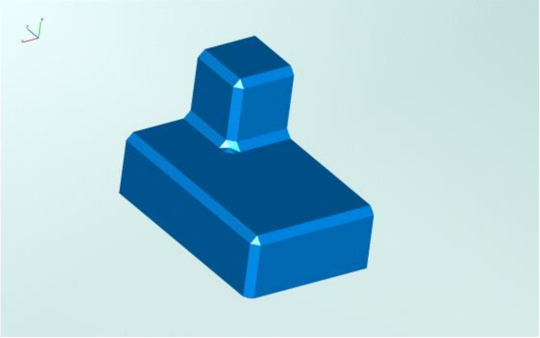

Figure 11: Ligaments shape for testing the code of the ligament lenght detection.

4.1.1 Setup of the Test Case

The mesh corresponds to the type of a structured mesh, and the cell type conforms with a cubic shape. A detailed drawing is presented in Figure 40 in the appendix.

Table 4-1: Mesh setup for the plausibility test of the numerical implementation.

Mesh Setup		
Case: Plausibility of the Numerical Implementation		
Mesh Setup		
Mesh Type	structured mesh	
Mesh Dimensions	0.2 x 0.1 x 0.4	[m]
Number of Cells	8 mio	
Cell Type	cubic	
Δx (cell width)	0.001	[m]
Particle Setup		
a = 10 Δx	0,01	[m]

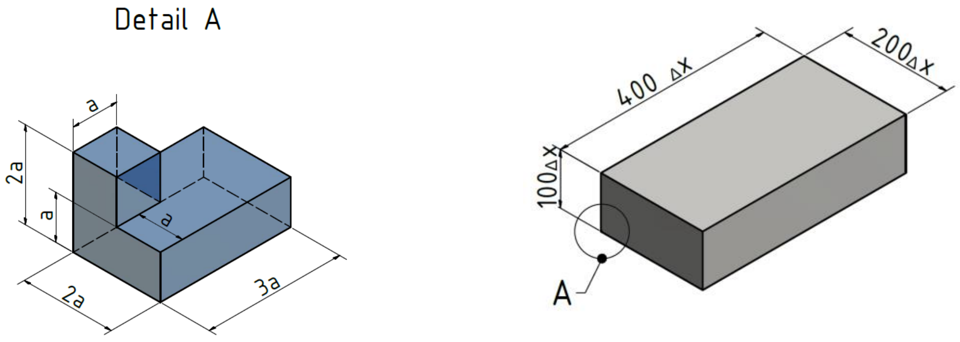

a b

Figure 12: a) tested particle includes dimensions as a detailed view from the right picture, b) mesh dimensions with initial location of the particle marked by capital A.

The CICSAM scheme was used in combination with the Automated Time Step (ATS). More usage details can be found in the AVL-FIRE^{TM} user manual [10]. This test case, was performed with the default setup for the automated time steps based on the recommended CFL number. Better results can be achieved, by changing the standard setup. An overview of the calculation setup is found in Table 4-2, and more details are placed in the appendix in (Table 8-1).

Table 4-2: Extraction of the calculation setup for the plausibility test.

Calculation Setup		
Case: Plausibility of the Numerical Implementation		
Setting Type	**Selection**	**Comments for Selection**
Settings Differencing Scheme for VF-Equ.		
Differencing Scheme for VF-Equ.	CICSAM	most sharpening scheme in AVL-FIRE^{TM}
Blending Exponent	2	default value to test with standard settings

4.1.2 Evaluation

For evaluation of the algorithm the solution of the numerical simulation was compared with an analytical result from Dankert [23]. On the stage of development, the comparison between analytical and numerical results were done step by step. This leads to minimizing the time for troubleshooting and bug fixing because of minimization the coded lines for checking their correctness in a mathematical manner. Table 4-3 represents the normalized values for the main moments of inertia and the normalized mass. For the main moments of inertia, the maximum error is less than 2.4 percent of the analytic solution.

Table 4-3: Loss of Accuracy in the plausibility test.

Evaluation Normalized Values	
Case: Plausibility of the Numerical Implementation	
Initialization	
$I_{1\,in}^{norm}$	1.00875
$I_{2\,in}^{norm}$	0.97655
$I_{3\,in}^{norm}$	1.01187
m_{in}^{norm}	1.00099
Loss of Accuracy	
$I_{1\,max}^{er}$	0.00875
$I_{2\,max}^{er}$	0.02345
$I_{3\,max}^{er}$	0.01187
m_{max}^{er}	0.00099

4.1.2.1 Conclusions from the Plausibility Test

The test case “Plausibility of the Numerical Implementation” was introduced to check the correctness of the implementation. A comparison for the ligaments lengths was not done, because they are tested in the particle test discussed in the next section 4.2. It is observed, that the results for the initialization step correspond well to the analytical solution for initialization the tested particle in a numerical mesh.

4.2 Particles Convection Tests

When a single particle is moved through a computational mesh, it is a well-known effect that the shape which is calculated by the VOF algorithm loses its accuracy. To overcome this, some scheme parameters should be variated to minimize the error. Also, the direction how the particle passed a single cell has an influence on the accuracy. As explained in section 2.2.1 the CICSA -scheme might has problems, if the interface is normal to the direction of motion. This is one fact which is shown in the following sections for the advection test with the CICSAM scheme. The translatory motion tests are evaluated with the same mesh. For each test case the particles shape and the mesh setup are explained first. The characterized particle shapes are shown in Figure 13 which includes the ratio of the ligaments lengths. Seven particles are initialized in a computational mesh. All of them belong to the category of triaxial ellipsoids.

Another important issue deals with the mesh size. In general mesh dependency tests were done with different cell sizes. This is not performed for the translatory convection test in this thesis. The different cell sizes were realized by different particle sizes, which are equivalent to tests of different cell sizes. This benefit reduced the number of investigated test cases, and leads to a better overview of the testing procedure.

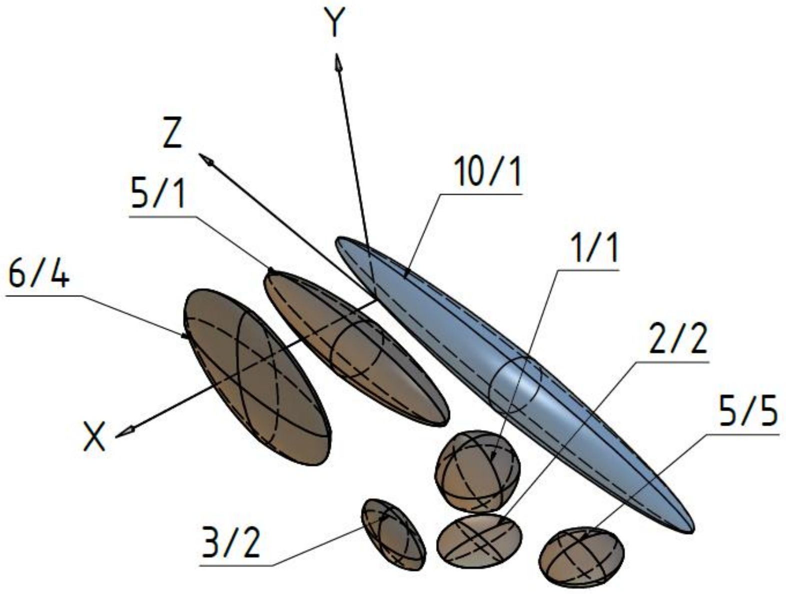

Figure 13: Different particles for the mesh dependency test. The number shows the ratio of the particle form factor.

The final results will be presented in detail with the tool of the normalized variable diagram for main moments of inertia as explained in section 3.3.2.1 in combination with the so called table of evaluation (see section 3.3.2.2). The analytical mass moment of inertia was calculated as described in Merziger and Wirth [35]. After a normalization of the analytical and numerical solutions the minimum and maximum error for each case was determined and the procedure of documentation follows the description in section 3. The detailed evaluation and setting tables can be found in the appendix.

4.2.1 Mesh Setup for Particles Convection Tests

The shapes as mentioned above require a special meshing technique. In AVL-FIRE^{TM} the so called meshing by formula tool was used for easy generation of the particles shapes. A detailed overview of particles sizes and their positions can be found in Table 4-5, and the overall mesh setup is listed in Table 4-4. In combination with the detailed drawing (see Figure 40 in the appendix) the shape of the particles are well defined.

Table 4-4: Mesh setup for particle convection test.

Mesh Setup		
Case: Particle Convection Test		
Mesh Type	structured mesh	
Mesh Dimensions	0.2 x 0.1 x 0.4	[m]
Number of Cells	8 mio	
Cell Type	cubic	
Δx (cell width)	0.001	[m]

Table 4-5 contains the ratio of the particle form in the first column named *Ratio form factor*. Followed by the column of *Dimensions triaxial ellipsoid* contains the dimensions of the three-semi axes (a, b, c) of the triaxial ellipsoid. The last three columns named *Center of gravity*, include the positions of the center of gravity (x, y, z) which presents the distances from the center of origin to each center of gravity for the corresponding particle.

Table 4-5: Measurements of the mesh dependency.

Dimensions of Particles						
Case: Particle Convection Test						
Ratio form factor	Dimensions triaxial ellipsoid			Center of gravity		
	a [m]	b [m]	c[m]	x [m]	y [m]	z [m]
1/1	0.020	0.020	0.020	0.068	0.050	0.197
5/5	0.020	0.004	0.020	0.068	0.050	0.285
2/2	0.020	0.010	0.020	0.097	0.050	0.241
10/1	0.015	0.015	0.150	0.018	0.050	0.155
5/1	0.015	0.015	0.075	0.058	0.050	0.080
6/4	0.010	0.040	0.060	0.105	0.050	0.065
3/2	0.008	0.016	0.024	0.105	0.018	0.173

4.2.2 Mesh Dependency for Translatory Particle Motion

Up next the mesh dependency will be illustrated on a set of different particles which variegate their form and sizes. The evaluation is done for translatory motions in the following directions: the coordinate axes X, Y, Z separate and the overlapped motions in XZ- and XZY directions (see Figure 13). The velocity is 50 m/s for each direction. This leads to higher velocity owing to the vectorial summation for the XY- and the XYZ- motions. To maintain the CFL number, a smaller time step is applied. Nevertheless, the variation of the velocity in flow direction has only minor impact on the results. An extraction of the calculation settings is represented in Table 4-6, and the full setup is present in the appendix.

Table 4-6: Extraction of the calculation setup for the dependency test with translatory particle motion.

Calculation Setup		
Case: Particle Convection Test		
Setting Type	**Selection**	**Comments for Selection**
Settings Differencing Scheme for VF-Equ.		
Differencing Scheme for VF-Equ.	CICSAM	most sharpening scheme in AVL-FIRE™
Blending Exponent	2	default value to test with standard settings

4.2.2.1 Evaluation

The mesh dependency test includes five calculations for different directions of motion, and the numerical solutions are compared with analytical results. The graphical analysis is shown in Figure 14, and the results in Table 4-7. The best numerical solutions are shown on the left-hand side, and the worst solutions on the right-hand side. For the CICSAM differencing scheme, the normalized values plotted over the time, and the monitoring presents some oscillations. It is obvious that the CICSAM differencing scheme shows some numerical instabilities maintaining the sharpness of the interface.

In terms of mesh dependency, it is seen that particles which have a thin and flat shape becomes more troubles in conjunction of fluctuations and accuracy when the direction of motion is perpendicular to the flat surface. Depicted examples are particles with a form factor of 5/5 for a motion in Y- direction and 3/2 in X- direction. Good results have been achieved with shapes of long and stretched particle longueurs in motion direction as seen for the form factor of 10/1.

Table 8-3 in the appendix shows the normalized results of the calculations. As explained above, it is evident that ligaments with a flat shape which move perpendicular to the surface, shows oscillations (see Figure 14). Special attention should be paid on the test case in Y- direction. This case shows the biggest error and the largest oscillations.

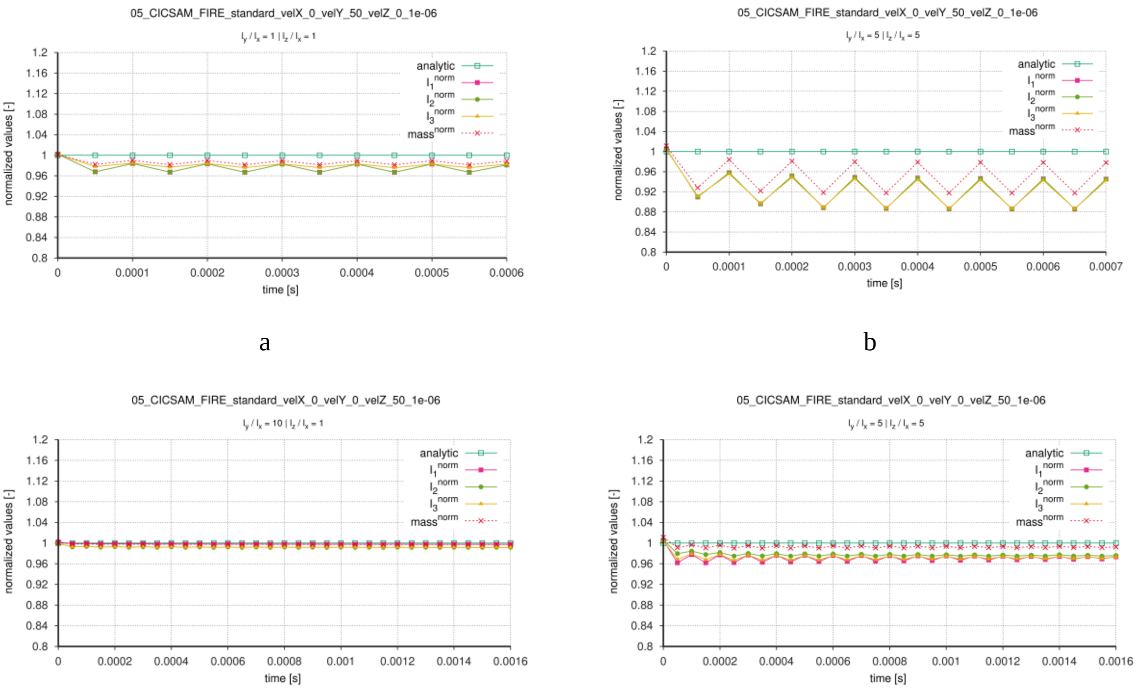

a

b

c

d

Figure 14: Excerpt of the normalized variable diagrams in relation with the motion direction. a) Velocity: Y-direction, form factor: 1/1 b) Velocity: Y-direction, form factor: 5/5 c) Velocity: Z-direction, form factor: 10/1, d) Velocity: Z-direction, form factor: 5/5.

Table 4-7: Extraction of the loss of accuracy table for the particle convection test.

Evaluation Normalized Values

Case: Particle Convection Test

Direction of Motion	**X**		**Y**		**Z**		**XZ**		**XYZ**	
Classification of Results	best	worst	best	worst	best	worst	best	worst	best	worst
Form Factor	2/2	3/2	1/1	5/5	10/1	5/5	5/5	3/2	1/1	3/2

Loss of Accuracy

$I^{er}_{1\,max}$ [%]	3.29	7.89	3.32	11.51	0.23	3.82	4.31	7.27	4.11	7.55
$I^{er}_{2\,max}$ [%]	1.85	7.57	3.32	11.44	0.86	2.52	3.96	6.99	3.97	7.09
$I^{er}_{3\,max}$ [%]	2.72	7.27	2.43	11.6	0.86	3.34	4.28	6.72	3.97	5.56
m^{er}_{max} [%]	1.52	5.27	1.86	8.23	0.27	1.00	1.56	4.79	2.47	4.84

The vectorial summation of the velocity leads to a CFL-number on the interface which is less than the limit of $CFL \leq 0.5$ The maximum value is $CFL_{max} \leq 0.15$. This is illustrated in Figure 15 for the motion in Z-direction and the motion in XYZ direction.

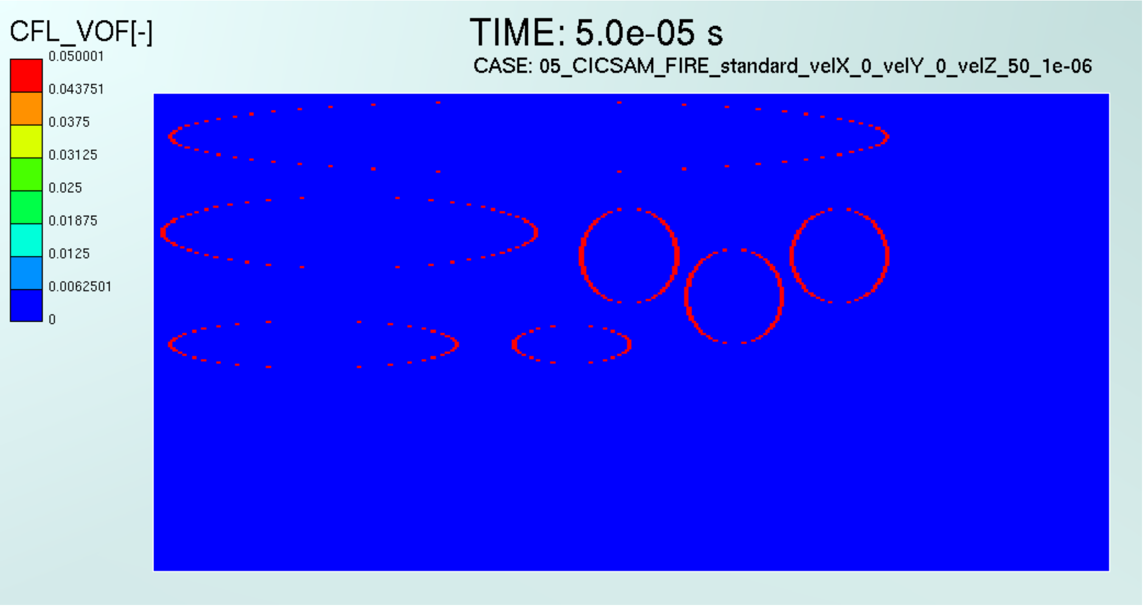

a

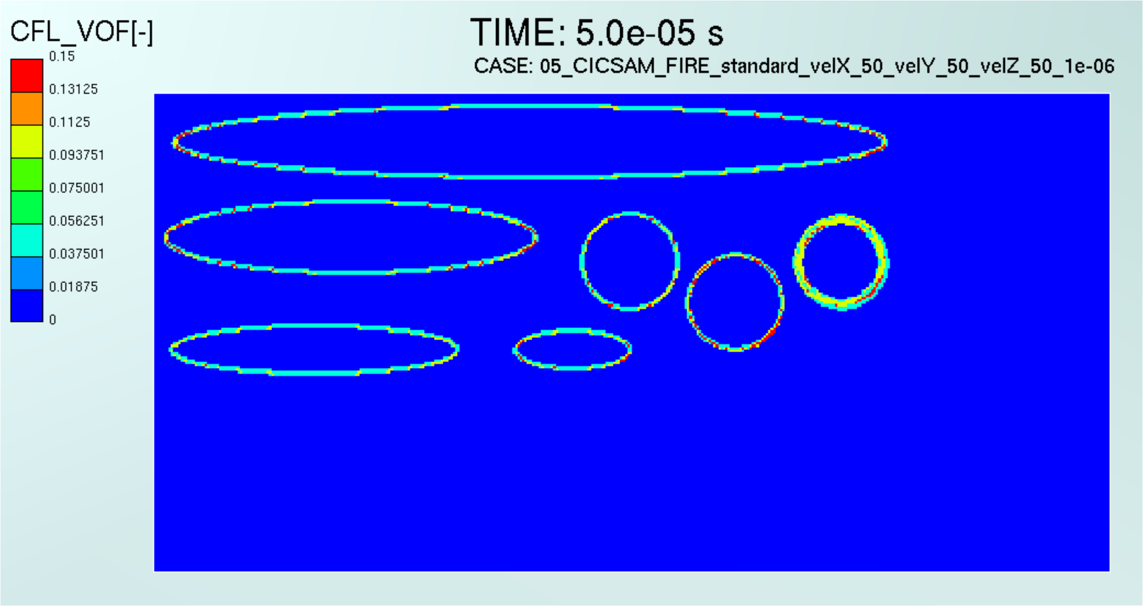

b

Figure 15: CFL number at the interface for different flow directions. a) Z- direction b) XYZ- direction.

4.2.2.2 Conclusions from the Mesh Dependency Tests

The mesh dependency was done for different convection velocity directions of the particles. It was seen that small flat particles have more problems to keep the accuracy when the flat shape is in motion direction. This is a known issue of the CICSAM scheme, when the interface is tangentially orientated to the flow direction, as discussed in section 2.2. Good accuracy was achieved for particles which are elongated in flow direction.

4.2.3 Dependency of the Blending Exponent on the Results

In AVL-FIRE^{TM} there is a possibility for blending between the two contributing differencing schemes. Therefore, the blending exponent C_θ in the calculation settings has to be changed. It influences directly the blending factor γ_f which is the transition factor between the downwind differencing scheme CBC and the UQ scheme in Eq. (2.21). For a better understanding both equations are rewritten

$$\gamma_f = min\left(1, \cos(2\theta_f)^{C_\theta}\right), \qquad \tilde{\alpha}_f = \gamma_f \tilde{\alpha}_{f_{CBC}} + \left(1-\gamma_f\right)\tilde{\alpha}_{f_{UQ}}. \tag{4.2}$$

Interesting possibilities for calculating the face volume fraction are presented in Eq. (4.3), where for $\gamma_f = 1$ the HYPER-C method will be used, and for $\gamma_f = 0$ the calculation is done with the ULTIMATE-QUICKEST method. Other values lead to a mixed discretization by blending both schemes. As introduced in the work of Ubbink [15], the recommended results are obtained with a blending exponent of $C_\theta = 2$ which is the default setting in AVL-FIRE^{TM}.

$$\tilde{\alpha}_f = \begin{cases} \tilde{\alpha}_{f_{CBC}} & when \quad \gamma_f = 1 \\ \tilde{\alpha}_{f_{UQ}} & when \quad \gamma_f = 0 \end{cases} \tag{4.3}$$

For further tests of the scheme, different calculations were done with several blending factors. The variation includes four different values as seen in Table 4-8. Each of them leads to different results which are investigated in the following section. The mesh setup and the initialized particles are the same as introduced at the top of this section. Only the calculation setup is changed as seen below.

The direction of motion was overlapped in X- and Y-direction and the space coordinates were the same as seen in Figure 13. The velocity was 50 m/s for each direction and this results again to 70.7 m/s after an vectorial summation. The blending exponent C_θ was variated from $C_\theta = 0$ to $C_\theta = 2$.

Table 4-8: Extraction of the calculation setup for dependency on the blending exponent.

Calculation Setup		
Case: Dependency on Blending Exponent		
Setting Type	**Selection**	**Comments for Selection**
Settings Differencing Scheme for VF-Equ.		
Differencing Scheme for VF-Equ.	CICSAM	most sharpening scheme in AVL-FIRE^{TM}
Blending Exponent	0 0.5 1 2	blending exponent variation

4.2.3.1 Evaluating the Blending Exponent Dependency

The accuracy depends on the ligaments form in combination with the motion direction. It was seen that flat particles turn to problems when the curvature of the interface is perpendicular to the flow direction. The lost accuracy in comparison to the analytic result is much higher for flat particle shapes then for elongated and stretched ligaments. In general, it has been seen that with smaller blending factors the interface becomes more and more sharp. For the CICSAM scheme, lower blending factors ($C_\theta = 0$) effects more oscillations over time which is illustrated in Figure 16. Instead higher values ($C_\theta = 2$) have more dumping effect and smooth the numerical results during two successive time steps (Figure 17). This is seen in the summation over the time for the normalized values of mass and main moments of inertia. For all calculations, the CFL number on interface is not higher then 0.1, and consequently lower the upper limit of 0.5 as recommended in AVL-FIRE^{TM}.

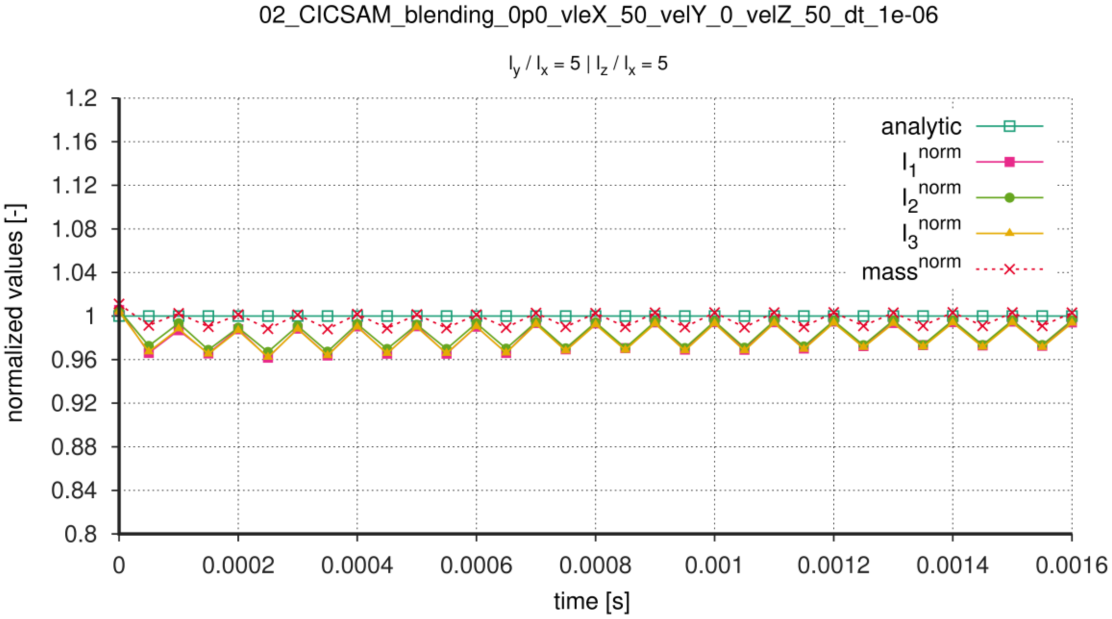

Figure 16: Normalized variable diagram for a flat particle with form ratio 5/5 and blending exponent 0.0

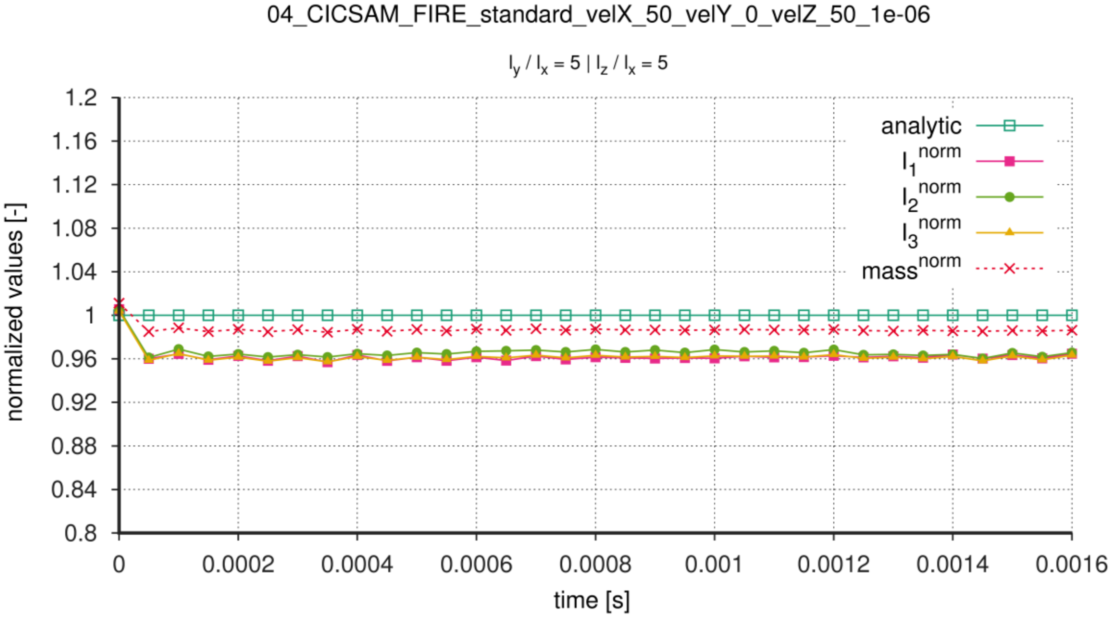

Figure 17: Normalized variable diagram for a flat particle with form ratio 5/5 and blending exponent 2.0.

A drawback of the VOF-method can be seen in Figure 18 where a cross section through the symmetry plane perpendicular to the ZX space coordinates of particle 5/5 was done. The volume fraction is plotted and red color represents the particle. Originally the shape was circular but over the course of time it changed to an octagonal form as presented in Figure 18d. Another effect for loosing conduct of particles form can be observed in fact of oscillations on the interface itself, which is seen during comparison over the time steps and different blending factors in Figure 18.

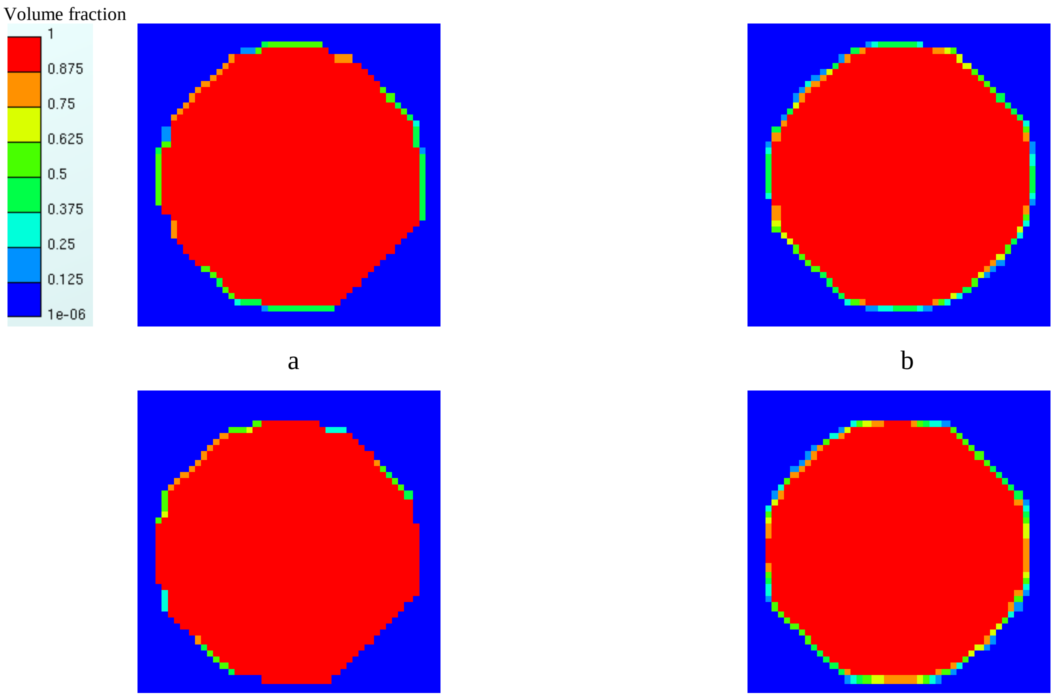

a

b

c

d

Figure 18: Volume fraction for different blending exponents for form ratio 5/5. a) time: 0.00155s $C_\theta = 0$ b) time: 0.0016s $C_\theta = 2$c) a) time: 0.00155s $C_\theta = 0$ d) time: 0.0016s $C_\theta = 2$.

Furthermore, it should be mentioned that higher blending factors do not guarantee the omittance of surface oscillations as seen in Figure 17. The investigated particle shape with a form ratio of 5/5 is a good exception because it shows more often oscillations in the results, when the blending exponent is higher. Values of $C_\theta = 0.5$ and $C_\theta = 1$ are not as interesting as the applied minimum ($C_\theta = 0$) and maximum values ($C_\theta = 2$). The evaluation of the loss of accuracy carried out that there are no considerable differences between the observed blending exponents for the maximum errors as seen in Table 4-8. Nevertheless, for minimum errors higher differences are visible. This behavior can be clearly seen in Figure 16 and Figure 17, where the minimum values in Figure 16 are much lower than in Figure 17.

Table 4-9: Extracted evaluation dependency on blending exponent.

Evaluation Normalized Values

Case: Dependency on Blending Exponent

Initialization

Blending Exponent	0	2
Form Factor	5/5	

Loss of Accuracy

$\boldsymbol{I^{er}_{1\,max}}$ [%]	3.83	4.31
$\boldsymbol{I^{er}_{1\,min}}$ [%]	0.52	3.54
$\boldsymbol{I^{er}_{2\,max}}$ [%]	3.31	3.97
$\boldsymbol{I^{er}_{2\,min}}$ [%]	0.39	3.11
$\boldsymbol{I^{er}_{3\,max}}$ [%]	3.79	4.28
$\boldsymbol{I^{er}_{3\,min}}$ [%]	0.60	3.53
$\boldsymbol{m^{er}_{max}}$ [%]	3.3	1.56
$\boldsymbol{m^{er}_{min}}$ [%]	1.21	1.16

4.2.3.2 Conclusion from the Variation of the Blending Exponent

The blending exponent was varied to blend between the two differencing schemes of CICSAM. For low blending exponents surface oscillations of the component values were visible. A damping effect was observed for the calculated particle properties like mass or moment of inertia by increasing the blending exponent to higher values. The highest damping was seen for a particle with a form ratio of 5/5. For spherical shapes the oscillations were in all main axis of inertia approximately the same which was illustrated in Figure 19.

Another test was made by comparing the minimum and maximum error. The maximum error is approximately the same during variation of the blending factor. Only the minimum error is smaller as seen in Table 4-9. If it is possible to reduce the oscillations, the blending forwards the HYPER-C scheme leads to computed results which are on the same respective level as the analytical solution.

Oscillations were not only observed by comparison of the normalized results. Also, some surface instabilities were seen in the interface between the two phases, as illustrated in-between the black lines of Figure 19. These small curvatures can also be seen on the opposite side of the particle and it looks like these small instabilities have numerical reason. Similar effects were seen in the real case investigation which is illustrated in the next chapter.

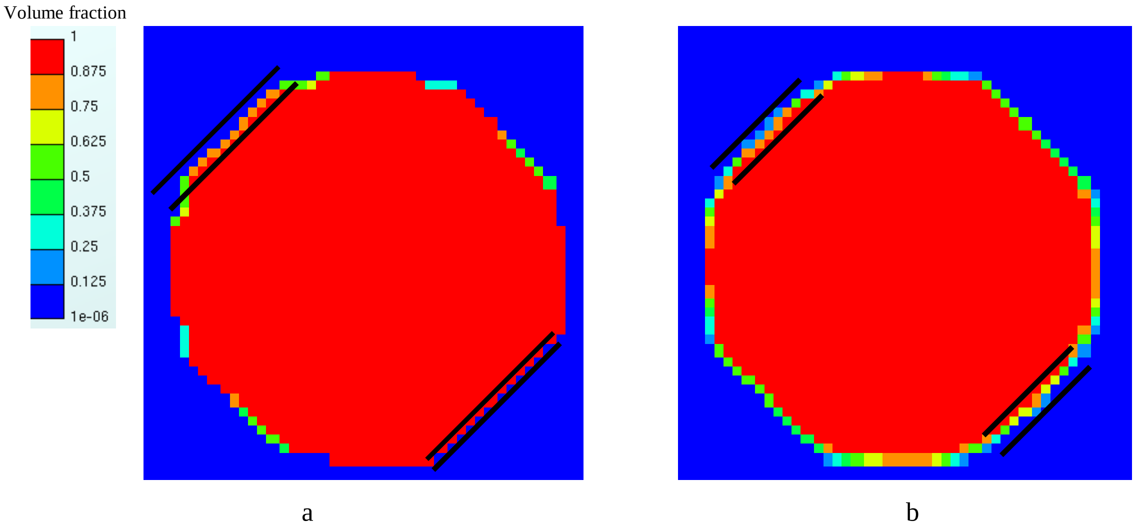

Figure 19: Interface instability a) $C_\theta = 0$, b) $C_\theta = 2$c.

4.3 Rotational Test Cases

The rotational test cases are based on the well-known work form Zalesak [34]. First of all, a modification was performed in form of a slotted sphere, instead of the slotted cylinder which was applied in Zalesak`s paper. The spherical form with the slot in the middle provides a sharper edge which is not an ideal condition for surface tracking with the VOF- method but this circumstance makes it ideal for testing. In combination with the particle initialization in a rotating velocity field, the possibility to evaluate the accuracy on long terms of particle motion is possible. Another fact is that the velocity increases with the radius. This leads to different CFL numbers over the particle length perpendicular to the circular motion direction. After the so called slotted sphere test cases the evaluation is performed with a cylinder similar to the original concept of Zalesak [34]. The angular velocity is $50\,\pi\ rad/s$ for all rotational test cases. The cell face of the hexahedrons is not always parallel to the particle shape and this leads to a deviation from the original shape.

4.3.1 Slotted Sphere Test Case

The investigation of the slotted sphere case includes the evaluation of particle rotating for four revolutions around the symmetry axis of the mesh. The rotation axis does not cross the center of gravity. The time steps were variated during the test cases but the end time of the calculation was the same for all. This is necessary for the investigation of the automatic time step tool, since it makes it possible to compare the total number of time steps of the different cases, which indicates the time step size. It is common knowledge that a big total number of time steps and a small time step size makes a numerical simulation slow. But in fact of the VOF-method this is often necessary because the scheme needs low CFL-numbers on the interphase, as explained in section 2.2.1.

The basis of the test case is a sphere which is slotted along the symmetry plane. This leads to sharp edges on the curvature and the form becomes an u-shaped profile. After the initialization process, the particle rotates in a mesh consisting of hexahedrons. The u-shaped particle rotates around the center point for four rotations with an angular velocity of $50\,\pi\ rad/s$. The initialized particle in the CFD simulation follows the drawing of Figure 20. Table 4-10 includes the mesh setup and the main dimensions.

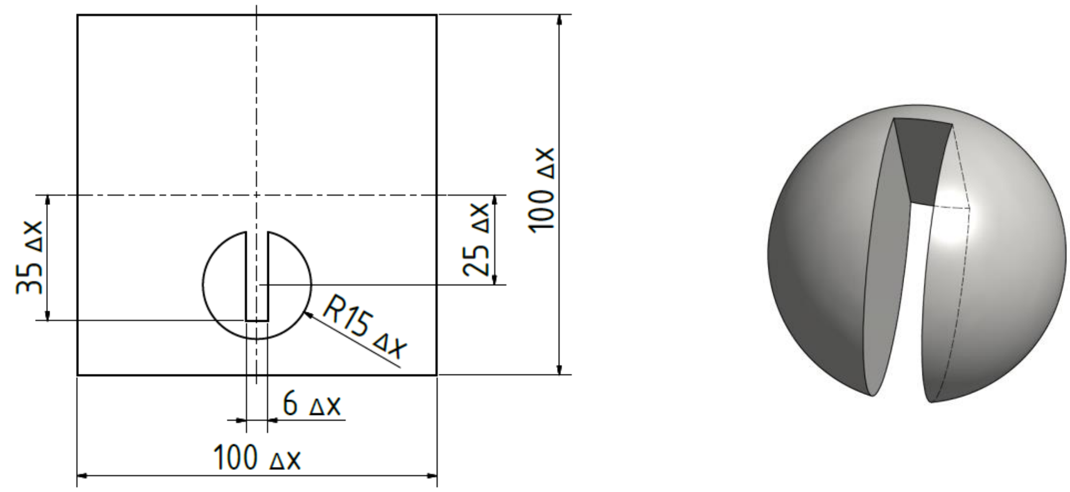

a b

Figure 20: Slotted sphere test case. a) Detail drawing, b) 3D- Model.

Table 4-10: Mesh setup for the particle convection test.

Mesh Setup		
Case: Slotted Sphere		
Mesh Type	structured mesh	
Mesh Dimensions	1.0 x 1.0 x 1.0	[m]
Number of Cells	1 mio	
Cell Type	cubic	
Δx (cell width)	0.01	[m]

The calculation setup is listed in Table 4-11 where the variation of the CFL Threshold is documented in the last row, and the value of the CFL Flow criterion was 0.5 for all tests. The variation of CFL Threshold influences the size of the time step.

Table 4-11: Extraction of the calculation setup for the slotted sphere test case.

Calculation Setup		
Case: Slotted Sphere		
Setting Type	**Selection**	**Comments for Selection**
Settings Differencing Scheme for VF-Equ.		
Differencing Scheme for VF-Equ.	CICSAM	most sharpening scheme in AVL-FIRE^{TM}
Blending Exponent	2	was tested for standard setting
Automatic Time Step		
CFL Flow	0.5	is only needed for advection test
CFL Threshold VOF Interface	0.5 0.45 0.25	variation; first column is standard setting

4.3.1.1 Evaluating the Slotted Sphere Test Case

The differences of the variation are shown from Figure 21 to Figure 23. It is clearly seen that the standard setting leads to the worst results, and in fact of accuracy, it got a non-conformance of more than 20 percent. All normalized values are decreasing in Figure 21 which is an indicator for loosing form stability. The worst deformation of the slotted sphere is seen in Figure 24a. The oscillations of the normalized values are seen in the rotational test cases too. The particle form stability is better for reduced CFD threshold values. This is also seen in the volume fraction plots of Figure 24, where α_{tres} = 0.5, as present in. The mathematical evaluation performed by the normalized variable values is shown from Figure 21 to Figure 23.

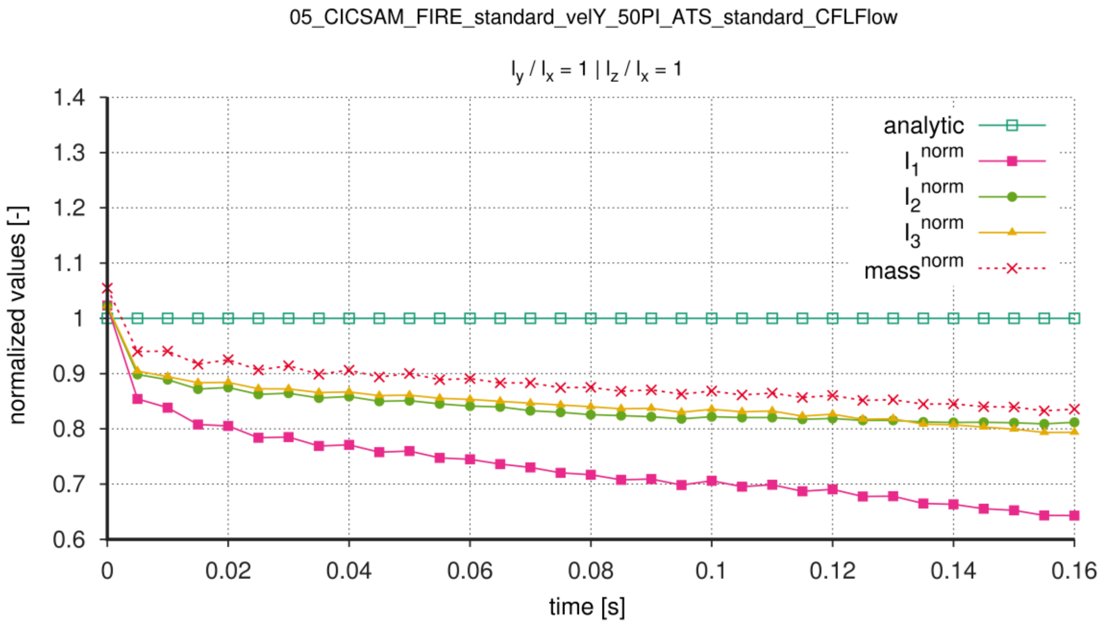

Figure 21: Normalized variable diagram for slotted sphere test case with ATS for standard values.

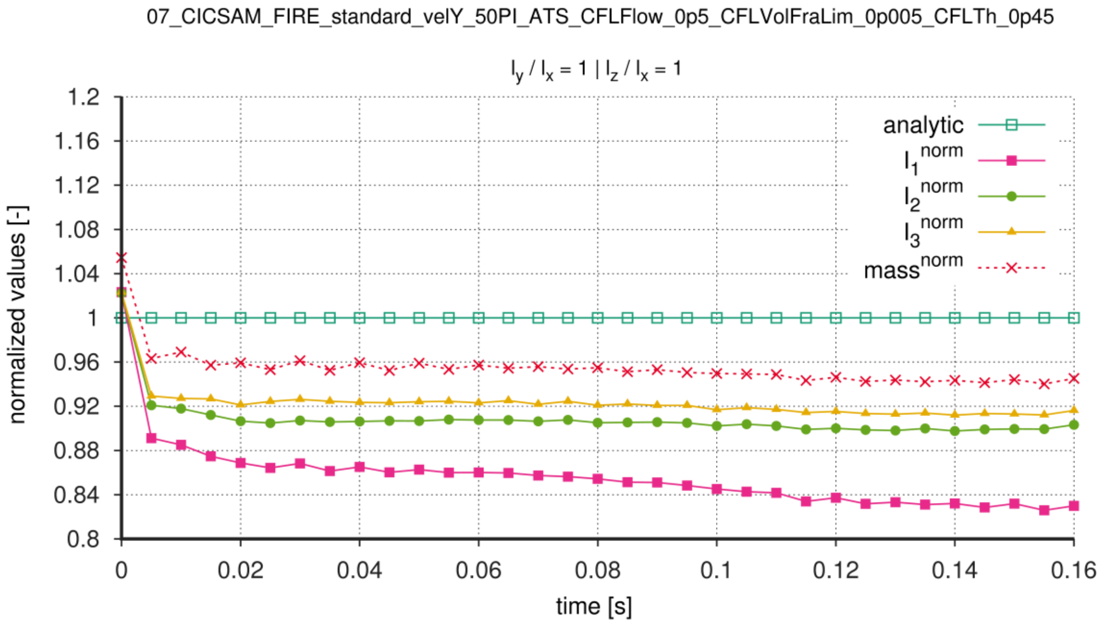

Figure 22: Normalized variable diagram for slotted sphere test case with ATS for CFL-Flow 0.5 and CFL-Threshold 0.45.

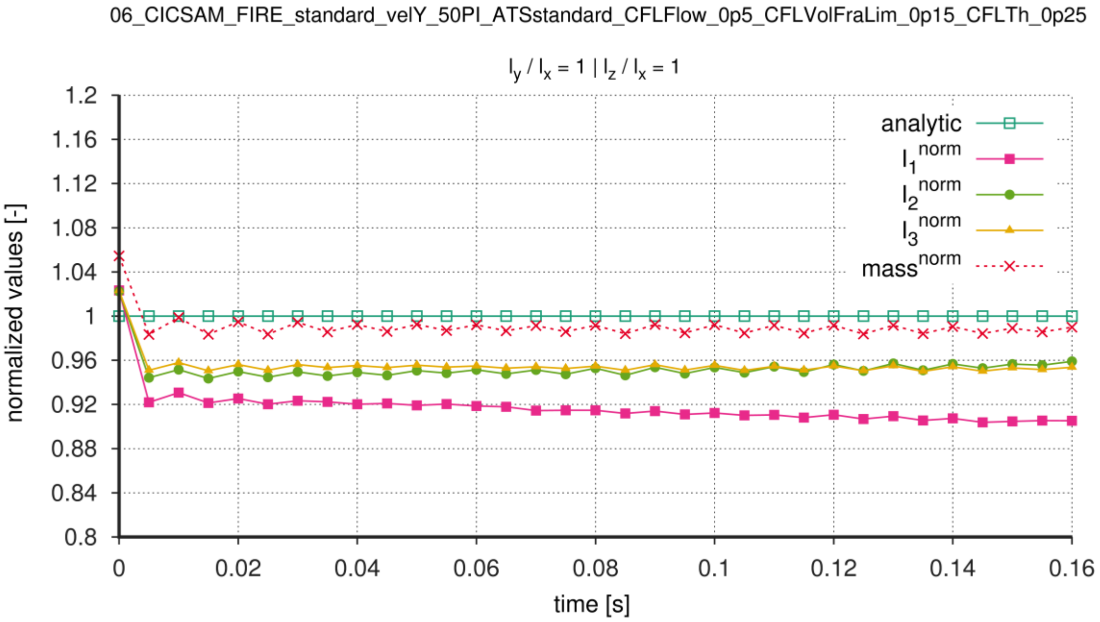

Figure 23: Normalized variable diagram for slotted sphere test case with ATS for CFL-Flow 0.5 and CFL-Threshold 0.25.

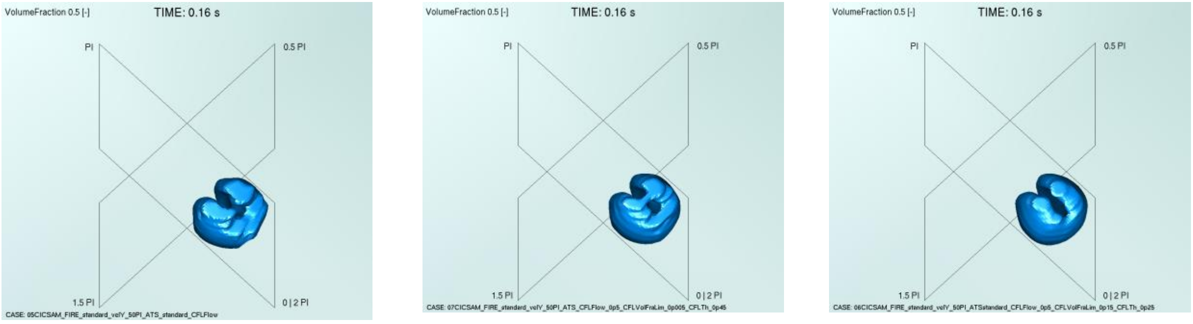

a b c

Figure 24: Loosing accuracy during variation of the CFL Threshold value presented on the end of calculation a) CFL Threshold corresponds to standard value b) CFL Threshold = 0.45 c) CFL Threshold = 0.25.

4.3.1.2 Conclusions of the Slotted Sphere Case

The best solution was found for a CFL Threshold of 0.25. This was achieved with a at least doubled number of time steps. The results in fact of accuracy were three to four times less accurate for the standard settings in the ATS module. But the direction for solution finding is clear, an accurate solution requires a CFL-threshold less than 0.45. The drawback of the higher accuracy is the increasing calculation time. This is seen in Table 4-12 when the time steps will decrease and the number of time steps grows. For an industrial case calculation, the relevant question will be how accurate the solution has to be. For small spherical ligaments, which includes only a few cells, there will be no big influence. It is clear that the u-shaped particle form with sharp edges on the curvature will not emerge in the real case, but it is a good test to show the limits of the VOF-method and how to change the settings to get accurate results.

Table 4-12: Extraction of the evaluation table for the slotted sphere test case.

Evaluation Normalized Values			
Case: Slotted Sphere			
Loss of Accuracy			
CFL Threshold VOF Interface	0.5	0.45	0.25
Form Factor	1/1		
$I_{1\,max}^{er}$ [%]	35.69	17.42	9.62
$I_{1\,min}^{er}$ [%]	14.58	10.89	6.93
$I_{2\,max}^{er}$ [%]	19.10	10.25	5.65
$I_{2\,min}^{er}$ [%]	10.15	7.91	4.10
$I_{3\,max}^{er}$ [%]	20.65	8.8	5.01
$I_{3\,min}^{er}$ [%]	9.56	7.07	4.22
m_{max}^{er} [%]	16.74	3.09	1.68
m_{min}^{er} [%]	5.93	5.99	0.14
Number of Time Steps			
Number	2488	3040	5328

4.4 Comparison of the CICSAM and HRIC Schemes

The next section gives an overview about the differences in the performance between the CICSAM and the HRIC differencing scheme. Based on the pro and contra of both schemes obtained from comparing the best and worst results from the CICSAM with the HRIC-scheme, a recommendation is given. At the end of this section, a guideline for a real case calculation will be established. The HRIC scheme was not as tested as the CICSAM scheme, because this was not the scope of this thesis. The same meshes as described in the tests of the previous section have been used for the HRIC tests. In the comparison the standard settings for both schemes were applied in terms of the blending exponent, $C_\theta = 2$ for CICSAM and $C_\theta = 0.05$ for the HRIC, as explained in section 2.2.1.

4.4.1 Comparison of the Translatory Particle Motion

The same test as described in section 4.2.2 was applied. The results are shown in Figure 25. The results, with the biggest error were obtained for the particle motion in Y-direction. Figure 25 shows the normalized values, where the graphics on the left hand side represents the evaluations of the CICSAM tests. On the right hand side the normalized HRIC values are shown.

The comparison was done for the same mesh, calculation settings, size of the time step and equal direction of motion. An interesting result is seen for the smallest particle with form ratio of 5/5. This had led to the results with the biggest error in the test case for CICSAM in section 4.2.2. There the calculations with the HRIC-scheme achieved better accuracy. This is unusual because for the other cases a trend for higher accuracy has been observed for the CICSAM scheme. One reason could be the oscillations visible in the CISAM scheme for this case. In general a trend for reduced surface oscillation the HRIC scheme as shown in Figure 25b where compared with Figure 25a but also for a less sharp interface can be observed.

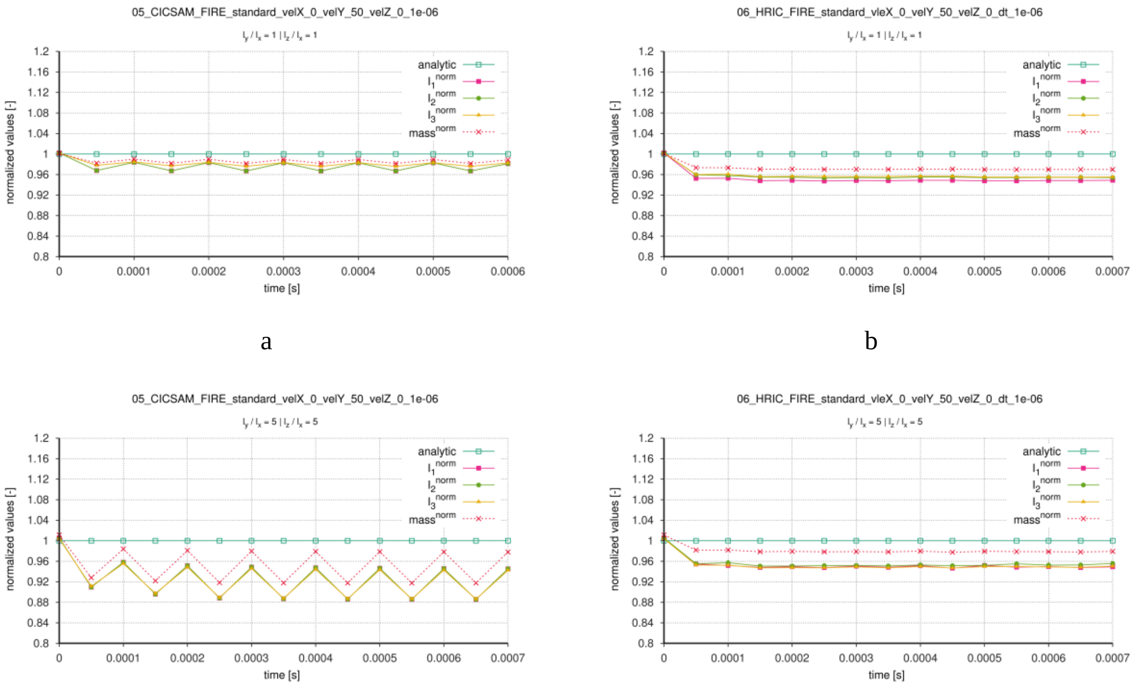

a b

c d

Figure 25: Comparison of CICSAM and HRIC-schemes for translatory particle motion, a) CICSAM-scheme, velocity Y-direction, form ratio 1/1, b) HRIC- scheme, velocity Y-direction, form ratio 1/1, c) CICSAM- scheme, velocity Y-direction, form ratio 5/5, d) HRIC- scheme, velocity Y-direction, form ratio 5/5.

Analogous to the diagrams for the normalized values over time the deviation from the analytical solution, as seen in Table 4-12, determine the quantitative difference between the two differencing schemes. For form ratios of 1/1 the best solutions were observed in Y-direction, and in that case the HRIC-scheme is not too bad. The biggest error was seen with a little bit more than five percent and this is only about two percent worse than the CICSAM solution. The test cases indicate that HRIC performs results with only a few percent less accuracy in the comparison with the analytic results compared with the CICSAM-scheme. For the form stability, which means how the discretization scheme is able to keep the initial particle shape over time, there is a difference, which is presented next for the ATS test cases.

Table 4-13: Comparison of the CICSAM and the HRIC schemes for the particle motion test.

Evaluation Normalized Values

Case: Comparison for Translatory Particle Motion

Initialization

Direction of Motion	**Y**			
Differencing Scheme	CICSAM	HRIC	CICSAM	HRIC
Form Factor	1/1		5/5	
Loss of accuracy				
$\boldsymbol{I^{er}_{1\,max}}$ [%]	3.32	5.26	11.51	5.34
$\boldsymbol{I^{er}_{2\,max}}$ [%]	3.32	4.65	11.44	4.94
$\boldsymbol{I^{er}_{3\,max}}$ [%]	2.43	4.51	11.6	5.31
$\boldsymbol{m^{er}_{max}}$ [%]	1.86	3.03	8.23	2.25

4.4.2 Comparison for Rotational Particle Motion with the Slotted Cylinder

In this section the comparison for rotational particle motion was done with the slotted cylinder test case. Based on the experience from section 4.3, again the ATS module of AVL-FIRE^{TM} was applied. The advantage is to ensure the same CFL numbers for the compared test cases, as set in the ATS setting in the calculation setup. As calculated in section 2.2.1 the improvement of accuracy requires a limitation of the CFL number for both differencing schemes. The comparison is also based on the Zalesak [34] test case, where here a slotted cylinder is applied. The axis of the cylinder is not the same as the rotation axis which is in the center of the mesh. Furthermore the three space coordinates of the cubic mesh cells are not parallel to the cylinders axes. This shows the influence when a ligament surface is not perpendicular to the orientation of the mesh.

4.4.2.1 Setup of the Slotted Cylinder Test Case

The mesh was the same as for the slotted sphere test case, only the ligaments shape was different because the spherical shape turns now to a cylindrical form. The detailed drawing of the test case can be found in Figure 26, and the corresponding mesh dimension are represented in Table 4-14.

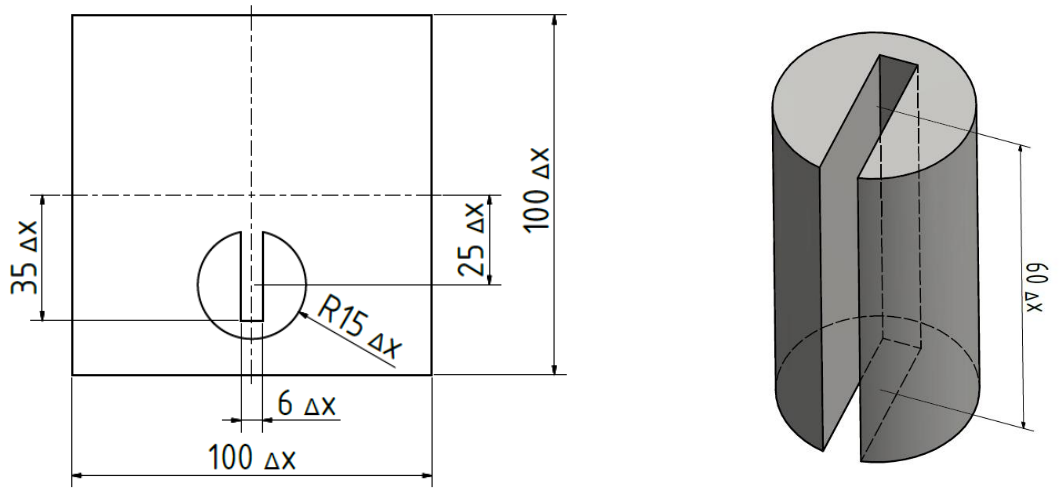

a b

Figure 26: Geometry of the slotted cylinder test case. a) Detail drawing, b) 3D- Model.

Table 4-14: Mesh setup for slotted cylinder test case.

Mesh Setup

Case: Slotted Cylinder

Mesh Type	structured mesh	
Mesh Dimensions	1.0 x 1.0 x 1.0	[m]
Number of Cells	1 mio	
Cell Type	cubic	
Cylinder Hight	60 Δ**x**	[m]
Δx (cell width)	0.01	[m]

An excerpt of the calculation setup is determined in Table 4-15. More details about the calculation settings can be found in the appendix. The main setup is the same as for the slotted sphere test case in section 4.3.1, only the differencing schemes are varied. The blending exponent is $C_\theta = 2$ for CICSAM scheme, and $C_\theta = 0.05$ for the HRIC scheme. The velocity field is initialized with a constant rotation around the mesh center with an angular velocity of $50\,\pi\, rad/s$. This leads to an orbital motion of the initialized particle which has a slotted cylinder as shape.

Table 4-15: Excerpt of calculation setup for the slotted cylinder test case.

Calculation Setup			
Case: Slotted Cylinder			
Setting Type	**Selection**		**Comments for Selection**
Settings Differencing Scheme for VF-Equ.			
Differencing Scheme for VF-Equ.	CICSAM	HRIC	variation of the differencing scheme
Blending Exponent	2	0.05	blending factor was default
Automatic Time Step			
CFL Threshold VOF Interface	0.45		was for all calculations the same

4.4.2.2 Evaluation of the Rotated Particle Motion Test Case

Analyzed was the accuracy of both differencing schemes with the analytical solution of the slotted cylinder. The values for the main moments of inertia and the mass were calculated with a CAD (Computer Aided Design) program to generate the normalized variables which were necessary for the comparison. The normalized variable diagram indicates some oscillations for the CICSAM scheme which are illustrated in Figure 27.

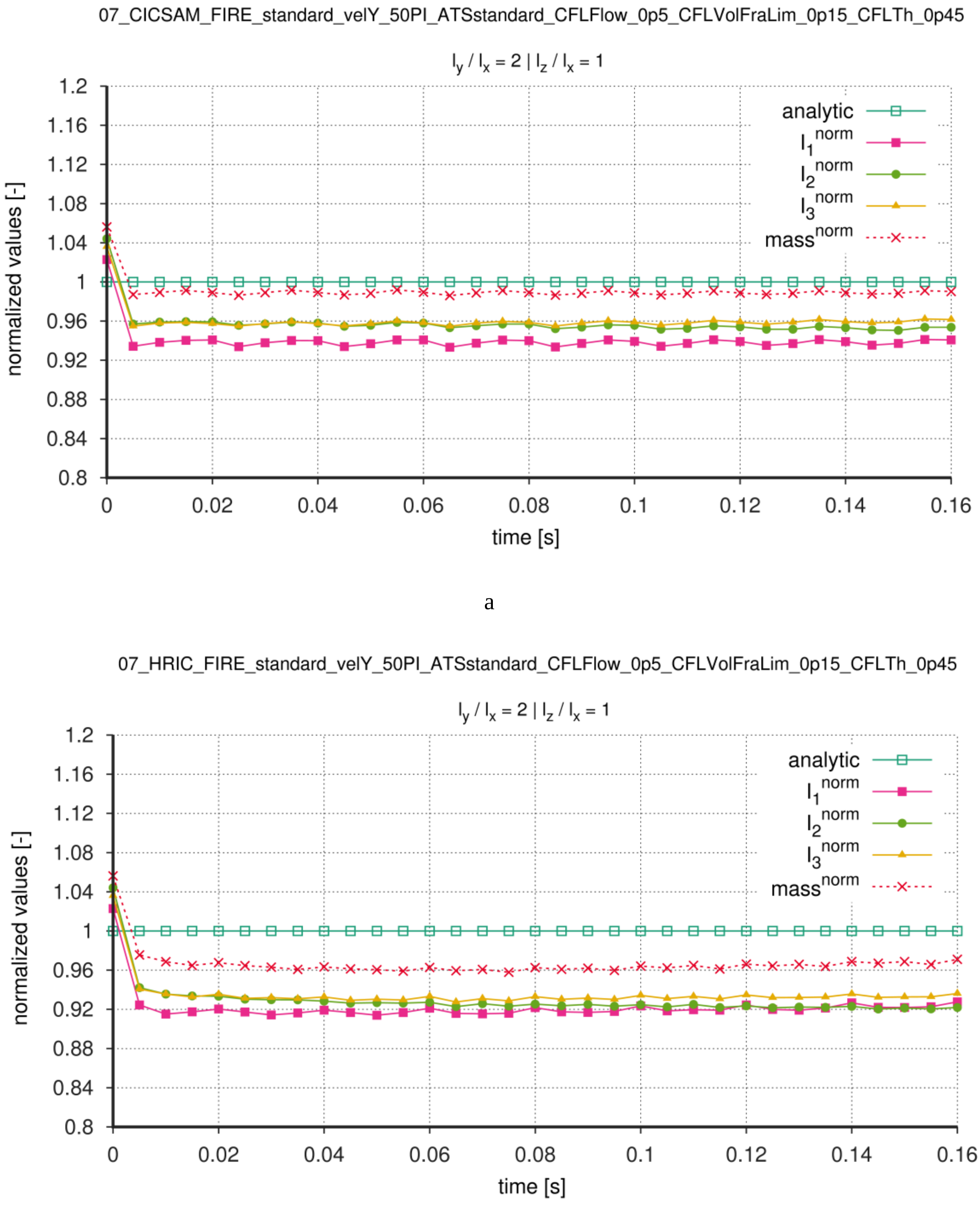

a

b

Figure 27: Comparison of CICSAM and HRIC-schemes for rotational particle motion, a) CICSAM, b) HRIC.

Some irregularities were also seen in the plotted iso-surfaces ($\alpha_{iso} = 0.5$) of the CICSAM simulation in Figure 28. Mainly the coarse and curled surface are detected on the interface which is perpendicular to the motional direction. The irregularly of the cylinder surface increases with the number of rotations. Nevertheless, the CICSAM scheme provides a good form stability and after four rotations the circular shape is maintained quite well. For the HRIC scheme the oscillations on the interface was not observed. But the volume fraction calculations lead to particle forms which diverge from the cylindrical initial shape, as seen in Figure 29.

1st rotation 2nd rotation 3rd rotation 4th rotation

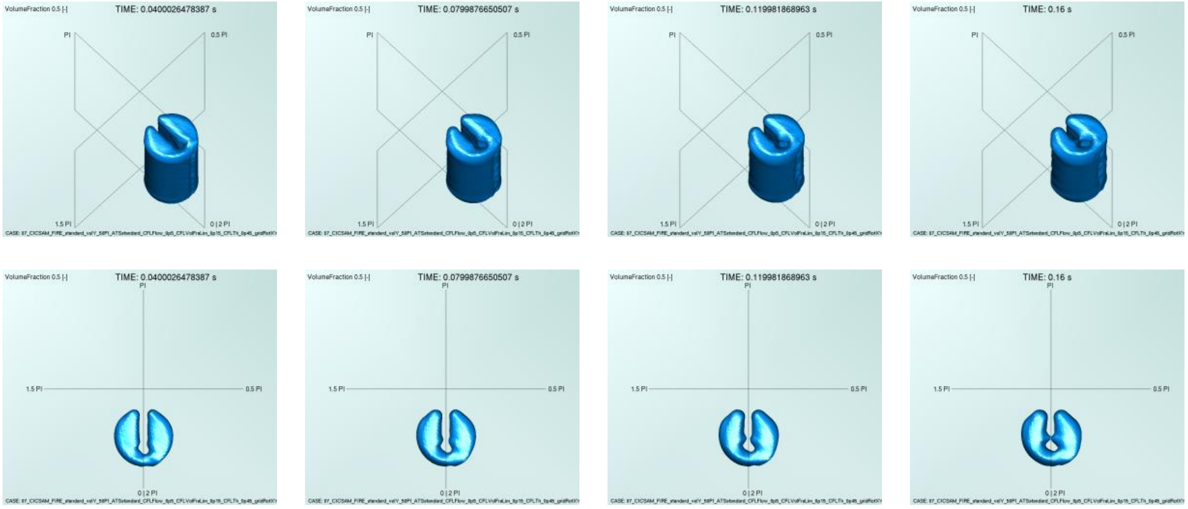

Figure 28: Iso-surface for volume fraction 0.5 over four rotations, for the slotted cylinder test case, CICSAM differencing scheme. The first row represents an isometric view and in the second row the top view is shown.

1st rotation 2nd rotation 3rd rotation 4th rotation

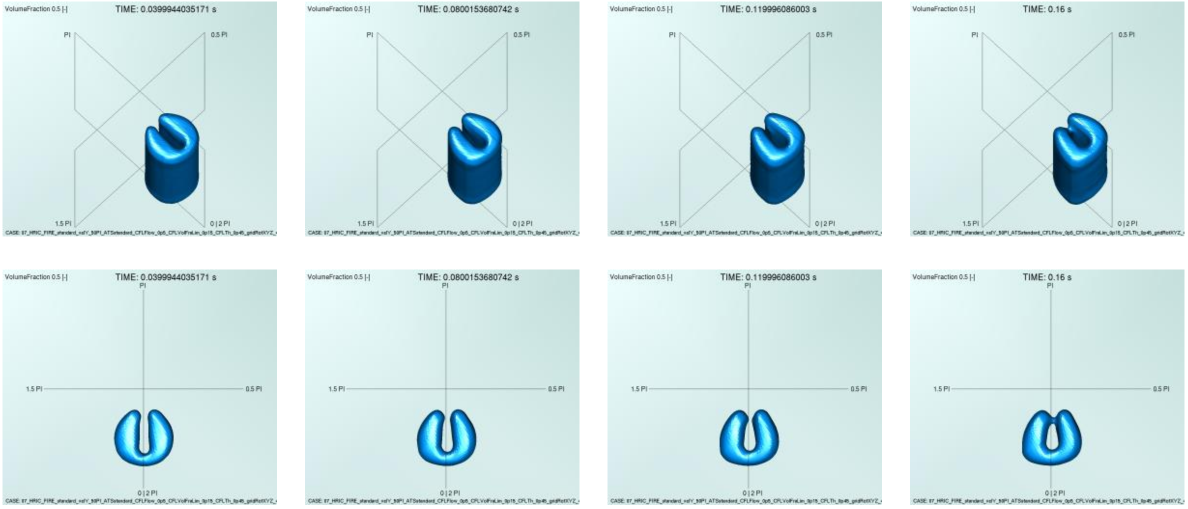

Figure 29: Iso-surface for volume fraction 0.5 over four rotations, for the slotted cylinder test case, HRIC differencing scheme. The first row represents an isometric view and in the second row the top view is shown.

Table 4-16 shows the excerpt of the evaluation table for the compared normalized variables and the number of time steps. The complete table is placed in the appendix, and it includes the normalized minimum and maximum values for the main moments of inertia and the mass. As already seen in the translatory motion tests the error of accuracy against the analytical result is for the HRIC-scheme only a few percent smaller than for CICSAM scheme (see Table 4-16). Also the number of time steps are roughly the same. Another interesting fact is that the normalized results at initial are bigger than in the represented test case (see appendix Table 8-10). This is caused by the initialization procedure covering all within the geometrical constraint, as explained in the introduction of this test case.

Table 4-16: Excerpt of the evaluation for the slotted cylinder test case.

Evaluation Normalized Values		
Case: Slotted Cylinder		
Initialization		
Differencing Scheme	CICSAM	HRIC
Form Factor	2/1	
Loss of Accuracy		
$\boldsymbol{I^{er}_{1\,max}}$ [%]	6.68	8.60
$\boldsymbol{I^{er}_{1\,min}}$ [%]	5.89	7.24
$\boldsymbol{I^{er}_{2\,max}}$ [%]	4.95	7.98
$\boldsymbol{I^{er}_{2\,min}}$ [%]	4.06	5.78
$\boldsymbol{I^{er}_{3\,max}}$ [%]	4.53	7.25
$\boldsymbol{I^{er}_{3\,min}}$ [%]	3.78	5.92
$\boldsymbol{m^{er}_{max}}$ [%]	1.40	4.22
$\boldsymbol{m^{er}_{min}}$ [%]	0.82	2.44
Number of Time Steps		
Number	3582	3612

4.4.3 Conclusions from the Comparison of the CICSAM and HRIC Differencing Scheme

Test cases for translatory and rotatory motion for different particles shapes were evaluated. The basis of the comparison were the tests for the CICSAM scheme, as discussed in section 4.2 for the translator, and in section 4.3 for the rotatory motion. With this experience the HRIC scheme was contrasted and the differences were outlined in detail. The conclusion is that the CICSAM scheme shows higher accuracy and form stability. But it might show also surface oscillations when the direction of motion is perpendicular to the interface. The reason for this instability was not investigated in this work, but it seems that they have numerical origin. This leads to the conclusion that further establishing work to improve the CICSAM differencing scheme is necessary.

5 Primary Break-Up at a Low-Pressure Gasoline Injector

To investigate the particle length algorithm on a real case, the multiphase injector flow simulation was performed. The low-pressure injector geometry is based on the work from Ishimoto et al. [3], which includes numerical results and a comparison with measurements. These results were used to compare the computed results with the CFD-code AVL-FIRE^{TM}. The calculation was performed for a three phase flow purpose which includes cavitating effects in the injector nozzle. Hence, the liquid-gas interface was calculated with the VOF-method (see section 2.2), and the liquid-vapor interface was computed with the EE-approach (see section 2.1). The challenge is to couple both methods AVL-FIRE^{TM} performs this quite well, as presented in the work of Edelbauer [4], from where the main settings for the presented low pressure investigation were taken. Simplifications were done through the assumption of constant temperature (isothermal) and constant density resulting in incompressible flow. The pressure inside the injector belongs to 0.444 MPa and the ambient pressure was 0.1 MPa. The fluid properties for the liquid phase belong to gasoline and the ambient gas is air. The characteristical geometrical dimensions are the nozzle length with $\mathrm{L} = 60\ \mu\mathrm{m}$ and the diameter with $D = 226\ \mu\mathrm{m}$. The computational mesh belongs to the category of structured meshes. It is separated into the injector and the spray domain, which are connected by a so called arbitrary interface at the nozzle orifice. The spray domain is separated into four refinement regions which commits of interlacing cones with different cell sizes. The small cell size regions are located where cavitation effects in the nozzle and spray break-up downstream the nozzle orifice takes place. The calculation was computed with the linear cavitation model which is similar to the AVL manual [10]. Turbulence modeling is applied with LES-CSM as described in section 2.4.

5.1 Meshing Process

The structured mesh includes 16.3 million cells. To fullfil the high mesh requirements a VOF simulation regarding small cell sizes, a special technique has to be used to avoid an excessive high number of cells. Different cell sizes are possible in meshes which are created with AVL-FIRE^{TM} and the so called refinement levels (I – V) are arranged along the expected spray axis through eccentrical canonical shapes. The mesh is shown in Figure 30 left, and the dimensions are listed in Table 5-1. The workflow will be presented in the following steps, and a detailed view on the mesh refinements levels and the dimensions will be found in Figure 30:

1. Generate a CAD-file of the investigated injector geometry without the spray area.
2. Create a block structured mesh for the injector and the nozzle.
3. Calculate the cell size for each refinement to get the number of cells before starting to mesh the spray grid.
4. Create the spray mesh with refinements regions.
5. Connect the injector and spray meshes on the outlet of the nozzle with the so called arbitrary interface applied between cells of different orientation and size.
6. Set the selections for the boundary conditions.

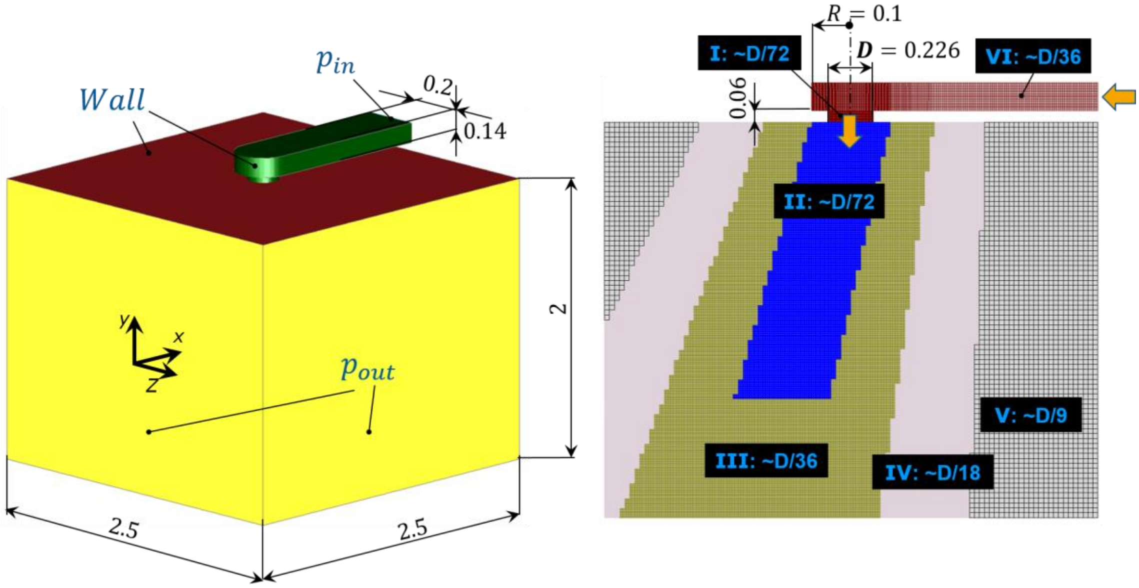

a b

Figure 30: Computational mesh of the low-pressure injector. a) dimensions and boundary conditions, b) mesh refinements in a cross section through the mesh axis. [36].

An overview about the mesh setup follows next. It should be mentioned that the number of mesh cells are the limitation for the calculation because they depend the number of CPUs which are available in the calculation cluster. So it is useful to make an estimation about the expected number of cells, which can be done easily by a simple calculation for a volume V_{ref}. For cubic cells it is easy, because the cell length in each direction has the same size which leads to Eq (5.1), and after a transformation the number of cells n_{cells} are known. As seen in the cross section of Figure 30 the different mesh domains with different cell sizes Δx have canonical shape, and so it is customary to calculate the volume for each refinement itself in order to get the cell number.

$$V_{ref} = \Delta x^{\,3} \cdot n_{cells} \tag{5.1}$$

After the connection step 5, the boundary conditions for the injector and spray domain were set. As shown in Figure 30 the surface selection marked by green (injector) and red color (spray domain) are set as wall boundary conditions ($Wall$). The inlet p_{in} and outlet p_{out} boundaries are marked with yellow color and are located far away from the nozzle to minimize their influence during the computation. As initial condition the injector is totally filled by the liquid phase (gasoline) and the spray domain includes only ambient gas (air). The boundary between liquid and gas is chosen at the outlet of the nozzle.

Table 5-1: Mesh setup for the low-pressure injector test case.

Mesh Setup		
Case: Low-Pressure Injector		
Mesh Type	structured mesh	
Mesh Dimensions	0.0025 x 0.0022 x 0.0025	[m]
Number of Cells	16.3 mio	
Cell Type	cubic	
Δx (smallest cell width)	3.125	[µm]
Characteristically Dimensions		
D (nozzle diameter)	226	[µm]
L (nozzle length)	60	[µm]
Refinement Levels		
I , II	$\sim \mathrm{D}/72$ = 3.125	[µm]
III	$\sim \mathrm{D}/36$	[µm]
IV	$\sim \mathrm{D}/18$	[µm]
V	$\sim \mathrm{D}/9$	[µm]
VI	$\sim \mathrm{D}/36$	[µm]

5.2 Calculation Setup

As mentioned before the calculation setup for the cavitation model is based on the work of Edelbauer [4]. There the model was validated against experimental data for cavitating nozzle flow, and this setup builds the basement for the following settings. For some values a pre-assessment can be done and this leads to the following section.

5.2.1 Assessments for the Calculation Settings

Before starting for the numerical simulation, it is customary to do some pre-assessments. This includes to estimate the amount of the velocity through the nozzle outlet which is calculated through Bernoulli's equation for incompressible flow without height change:

$$\mathrm{p} + \frac{1}{2}\rho U^{2} = const \tag{5.2}$$

It is necessary to know the velocity in a point close to the nozzle orifice to calculate the minimum time step for the first calculation step which is needed for the ATS setting. It is estimated by the CFL-number which should not be bigger than $\mathrm{CFL} \leq 0.5$. After transformation of the CFL criterion in Eq. (5.3), the time step $\Delta \mathrm{t}$ is obtained. Where Δx is the minimum cell size which is known from the mesh generation. It should be mentioned that this kind of CFL criterion is a simplification and is slightly different, to those of the CFD-code of AVL-FIRE^{TM}. Where a flow based criterion as discussed in section 2 is applied.

$$\mathrm{CFL} = \frac{U\,\Delta t}{\Delta x} \tag{5.3}$$

5.2.2 Calculation Setup

The fluid properties are presented in Table 5-2. They are based on the AVL data set for gasoline fuels which represent liquid, vapor and air.

Table 5-2: Fluid properties for the low-pressure injector case.

Fluid Properties

Case: Low-Pressure Injector

Fluid	**Liquid**	**Vapor**	**Gas**
Density [kg/m^3]	732	4.62	1.134
Dynamic Viscosity [Pa s]	0.442E-03	6.2E-06	1.51E-05
Surface Tension [N/m]	0.0198		
Saturation Pressure [Pa]	6155		
Temperature (isothermal) [K]		293.15	

For a multiphase simulation, a lot of settings have to be configurated to generate reasonable results. AVL-FIRE^{TM} provides a cell-centered finite volume approach where the cell centered gradients are computed by a linear least-square method. Solving the convection terms is proceeded by different differencing schemes. As described in the theory section of this thesis the volume fraction equation is discretized in different ways. The CICSAM scheme is used for the VOF-method and computes the interaction between liquid and gas. The EE-approach is applied for the liquid-vapor interface and follows an upwind discretization. The SMART-bounded differencing scheme is used for the convection term in the momentum equation, as presented in Gaskell and Lau [14] and in the AVL-FIRE^{TM} manual [10]. For the continuity equation, the SIMPLE algorithm and the central differencing scheme are applied.

A brief summary about the numerical setup is presented in Table 5-3. The discretization for the volume fraction transport equation is done with the CICSAM-scheme. The blending exponent $C_\theta = 0.25$ is low that there is a tendency to the most sharpening HYPER-C scheme in order to get a sharp interface. The ATS setup with a low CFL-number limit leads to small time steps. The selected configuration is necessary to guarantee a stable and robust calculation. In AVL-FIRE^{TM} a limit for the maximum velocity over the whole domain can be set. This was also applied to increase the simulations stability. During the primary break-up, it was observed several times that a gaseous bubble was totally surrounded by liquid, and squeezing effects lead to high velocities owing to the incompressible gas assumption. A compressible simulation would be more physical, but this was not considered in this investigation.

Table 5-3: Calculation setup for the low-pressure injector case.

Calculation Setup		
Case: Low-Pressure Injector		
Setting Type	**Selection**	**Comments for Selection**
Settings Differencing Scheme for VF-Equ.		
Differencing Scheme for VF-Equ.	CICSAM	most sharpening scheme in AVL-FIRE^{TM}
Blending Exponent	0.25	smaller blending exponent for sharper interface
Automatic Time Step		
CFL Flow	0.5	is only needed for advection test
CFL Threshold VOF Interface	0.45	was for all calculations the same

5.3 Evaluation of the Low-Pressure Injector

The first step of the evaluation process was to calculate the characteristic dimensionless numbers (see Table 5-4) to categorize the break-up regime as seen in section 2.6. With Bernoulli’s equation a velocity of 30.6 m/s was estimated of for the nozzle outlet. The Reynolds number is 11475 and the jet follows to turbulent flow. The Weber number leads to 7853 and the Ohnesorge number is calculated to 0.0077. With the calculation of these three dimensionless numbers the operation point can be drawn into the Ohnesorge nomogram, as illustrated by the red circle in Figure 31. At idealized conditions the second wind-induced break-up regime can be expected.

Table 5-4: Dimensionless Numbers for Low-Pressure Injector.

Characteristical Dimensionless Numbers	
Case: Low-Pressure Injector	
Bernoullie`s Velocity [m/s]	30.6
Reynolds Number [-]	11475
Weber Number [-]	7853
Ohnesorge Number [-]	0.0077

It should be mentioned that some simplifications were done for the calculation of the dimensionless numbers. It was subjected to incompressible and isothermal flow, so it is allowed to calculate the velocity at the outlet of the nozzle with Bernoulli’s equation. Also, the velocity is not constant over the injection period of time, and consequently the point of the expected break-up regime will move.

In the study of Ishimoto et al. [3] it was already discussed that the current injector geometry leads to cavitation. Consequently, the mechanism for primary break-up will be aerodynamical effects (Kelvin-Helmholtz instability), turbulence and cavitation. Aerodynamic induced break-up mechanisms can be observed especially in the early beginning of the jet formulation but also later over the time. Cavitation can be detected over the whole computation, mainly seen as string cavitation.

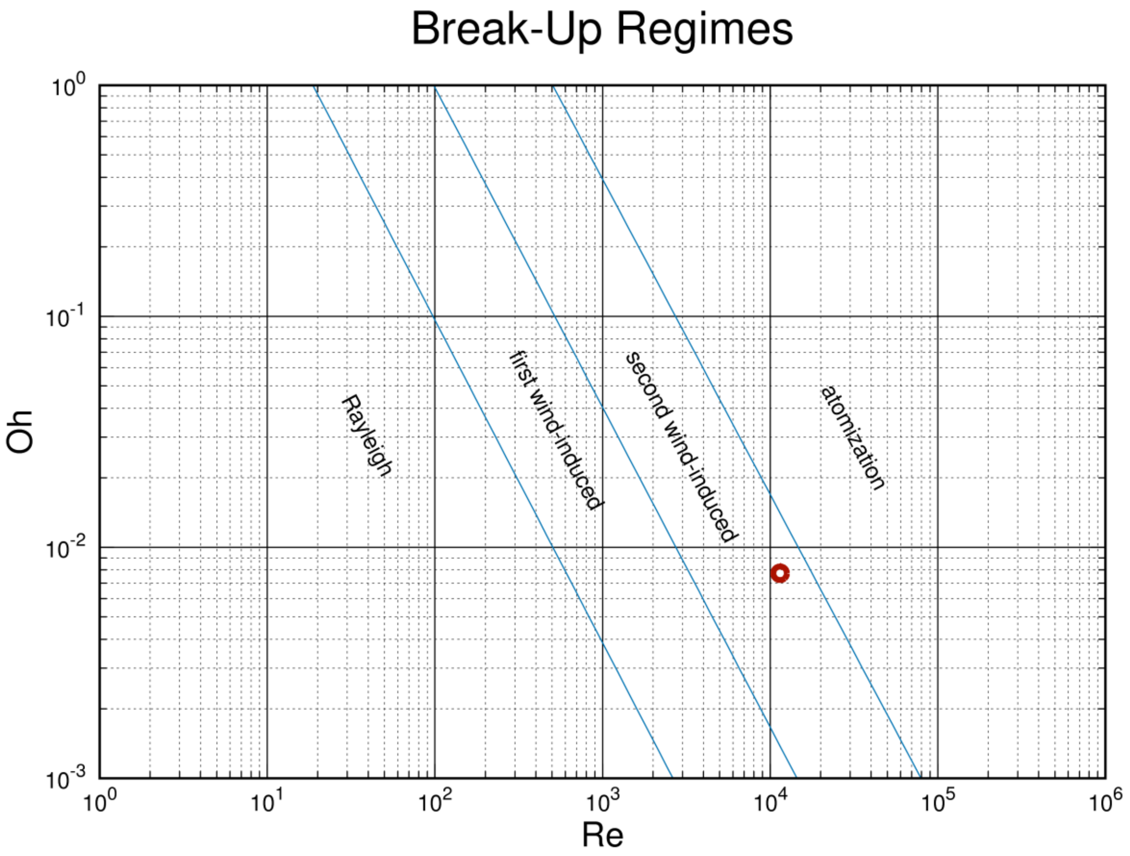

Figure 31: Estimation of the expected break-up regime with the Ohnesorge nomogram of Reitz and Braco [27]. The red circle indicates the operation point.

5.3.1 Cavitation Effects

Several cavitation effects were observed for the presented injector, sometimes cavitation inception and beginning cloud cavitation, but most of the time cavitation in the vortex center often called string cavitation. As discussed in section 2.7, cavitation starts at nucleis in regions where the static pressure has low magnitudes. This will be seen around the edge of the nozzle hole where the flow is reduced and strongly accelerated. In Figure 32a the beginning cloud cavitation has its origin in the acceleration of the fluid which is illustrated by the vector plot in the cross section of the nozzle inlet. The blue colored iso-surface represents the volume fraction of the liquid ($\alpha_l = 0.5$), and the red colored surface the vapor phase ($\alpha_v = 0.2$). Another cavitation effect is caused by vortexes in the nozzle. In general, to resolve this kind of effects a LES and high mesh resolution are required. For the presented simulation the smallest size in this mesh region was $3.125\mu m$. This high effort was necessary to calculate the string cavitation visualized in Figure 32b. The causative vortexes can be clearly observed in the vector plot, where in the center of the two swirls the two cavitation tubes are visible. As mention in the theory part the string cavitation is highly unstable and its stochastic occurrence was observed during the whole computation.

The streamlines and the red colored volume fraction iso-surface in the second row of Figure 32, allows to visualize the flow domain from a side view. The swirl motion and the string cavitation in the vortex center are clearly visible (Figure 32d). Upstream in direction toward the inlet, a laminar undisturbed inflow can be observed.

The third row shows the volume fraction field in a planar cut through the coordinate center in the middle of the mesh. The last row shows the local pressure field. Cavitation takes place in regions where the local pressure is less than the saturation pressure of gasoline, which is listed in Table 5-2. In the next section the influence of cavitation on the primary break-up will be discussed. Later on the explanation of the primary break-up the influences of the instabilities will be seen and how it impacts during the spray formation.

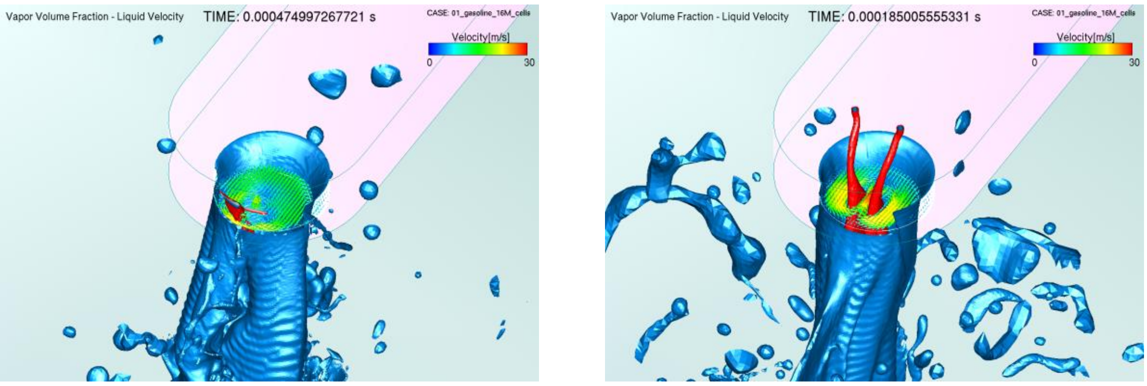

a: velocity from 0-30m/s b: velocity from 0-30m/s

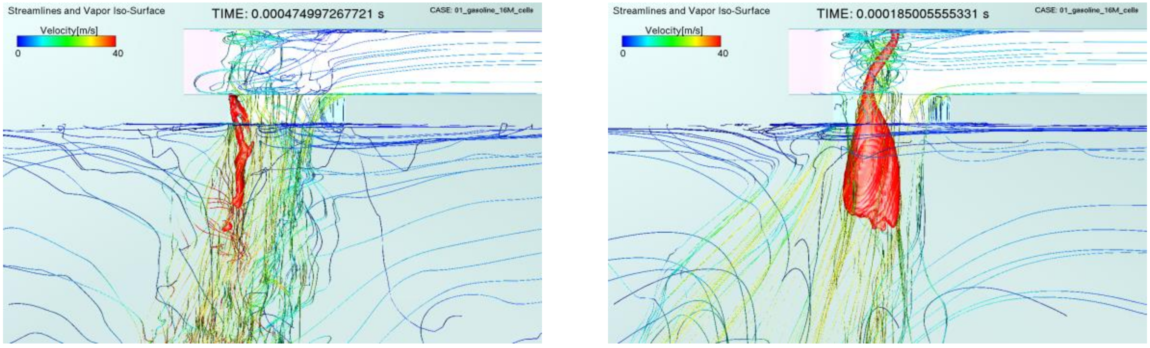

c: velocity from 0-40m/s d: velocity from 0-40m/s

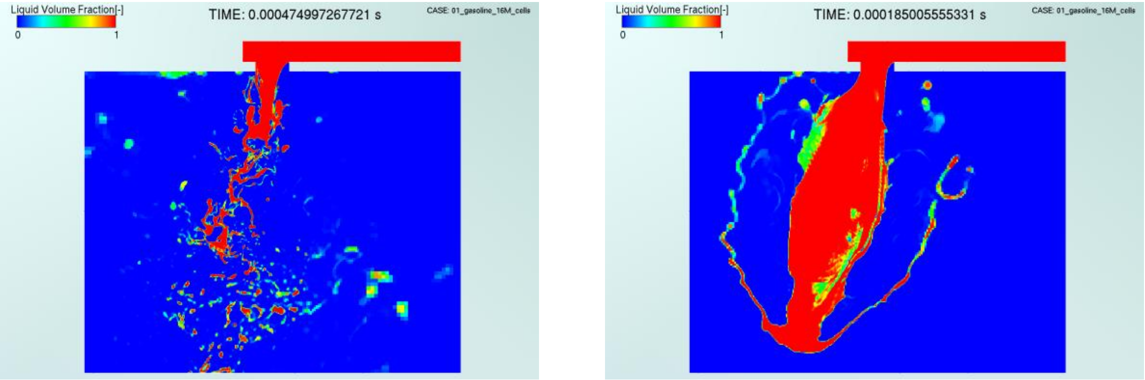

e: volume fraction 0-1 f: volume fraction 0-1

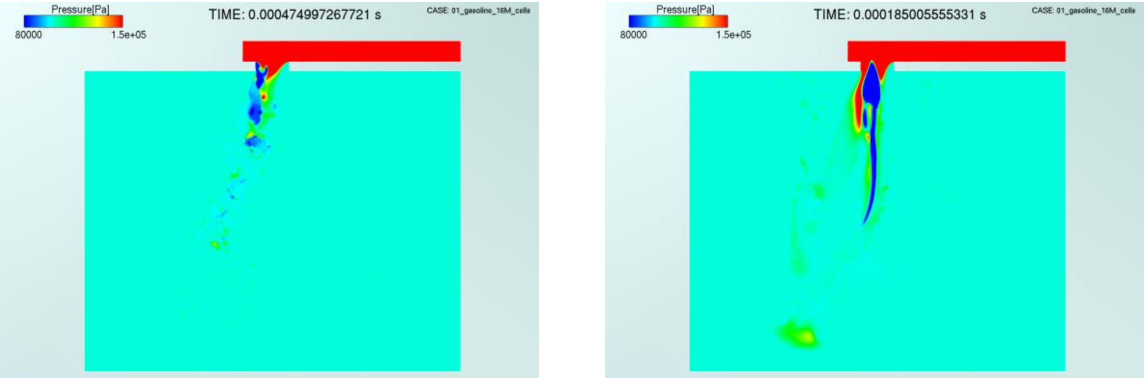

g: pressure 8000-1.5E+05 Pa h: pressure 8000-1.5E+05 Pa

Figure 32: Visualization of the flow field at two different time instants. a) Cavitation starting at the nozzle entrance, b) cavitation induced through swirls c) and d) represents the side view of a) and b) and shows the streamlines colored by velocity the streamlines. e) and f) shows the volume fraction, g) and h) the local pressure.

5.3.2 Primary Break-Up

The primary break-up mechanisms of the simulated liquid jet and their influence on the spray pattern are discussed in this section. One should mention that the illustrations of Figure 6 in the theory section are schematic representations under idealized conditions and will not strictly occur in the investigated injector. In general, the different break-up mechanisms are overlapped. It is also important to separate between numerical surface oscillations as detected in section 4.3 and the physical aerodynamic surface waves on the jet. Anyway, the observed mushroom shape of the liquid at the early beginning of the injection, is clearly induced by relative motion between ambient gas and liquid as shown in Figure 33.

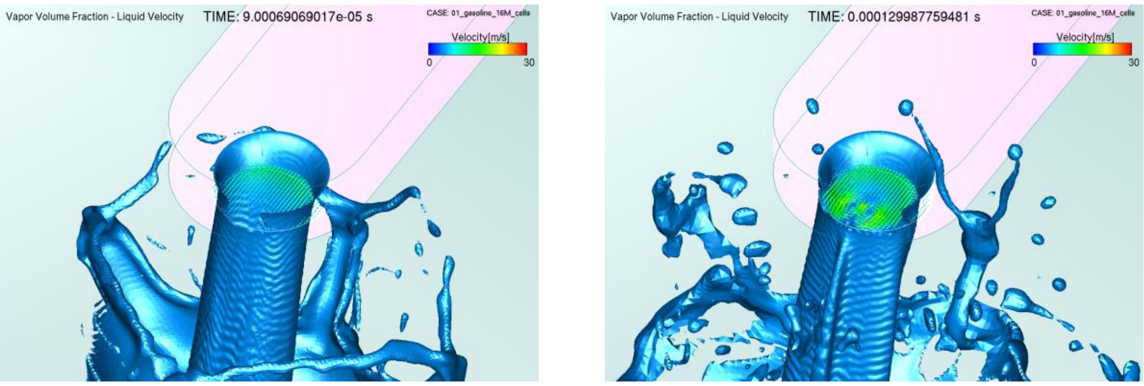

a b

Figure 33: Aerodynamical induced Primary break-up for volume fraction 0.5.

One mechanism for primary break-up is cavitation, as shortly discussed in the theory section. In the simulated low-pressure injector this effect is presented over the period from 0.385 to 0.455ms. It is interesting to see the bulge on the right-hand side of the liquid jet in Figure 34a downstream the nozzle orifice. Figure 34b the jet break-up induced by nozzle instabilities and cavitation is seen at the early beginning. In the next pictures, Figure 34c-h, the spray break-up and its impacts of the final spray pattern is illustrated up to the time of 0.455ms. It is obvious that string cavitation is a highly unstable process and the spray pattern from an earlier disintegration event is visualized in Figure 34a.

a b
c d
e f
g h

Figure 34: Detailed view on the liquid break-up from 0.385 – 0.455ms. Blue iso-surface for the liquid $\alpha_l = 0.5$, and red for vapor $\alpha_v = 0.2$.

5.3.3 Comparison with Experimental Results

The low-pressure Injector was investigated in detail by Ishimoto [3]. His investigation was done with a three phase numerical simulation with the CFD code OpenFoam and a comparison with experiments was performed. For this thesis, only the experimental data from Ishimoto et al. [3] were used for comparison. The numerical simulation of this thesis was done on a much finer mesh but as incompressible simulation with AVL-FIRE^{TM}. This simulation is reasonable because the flow pressure is not high, and compressible effects can be neglected.

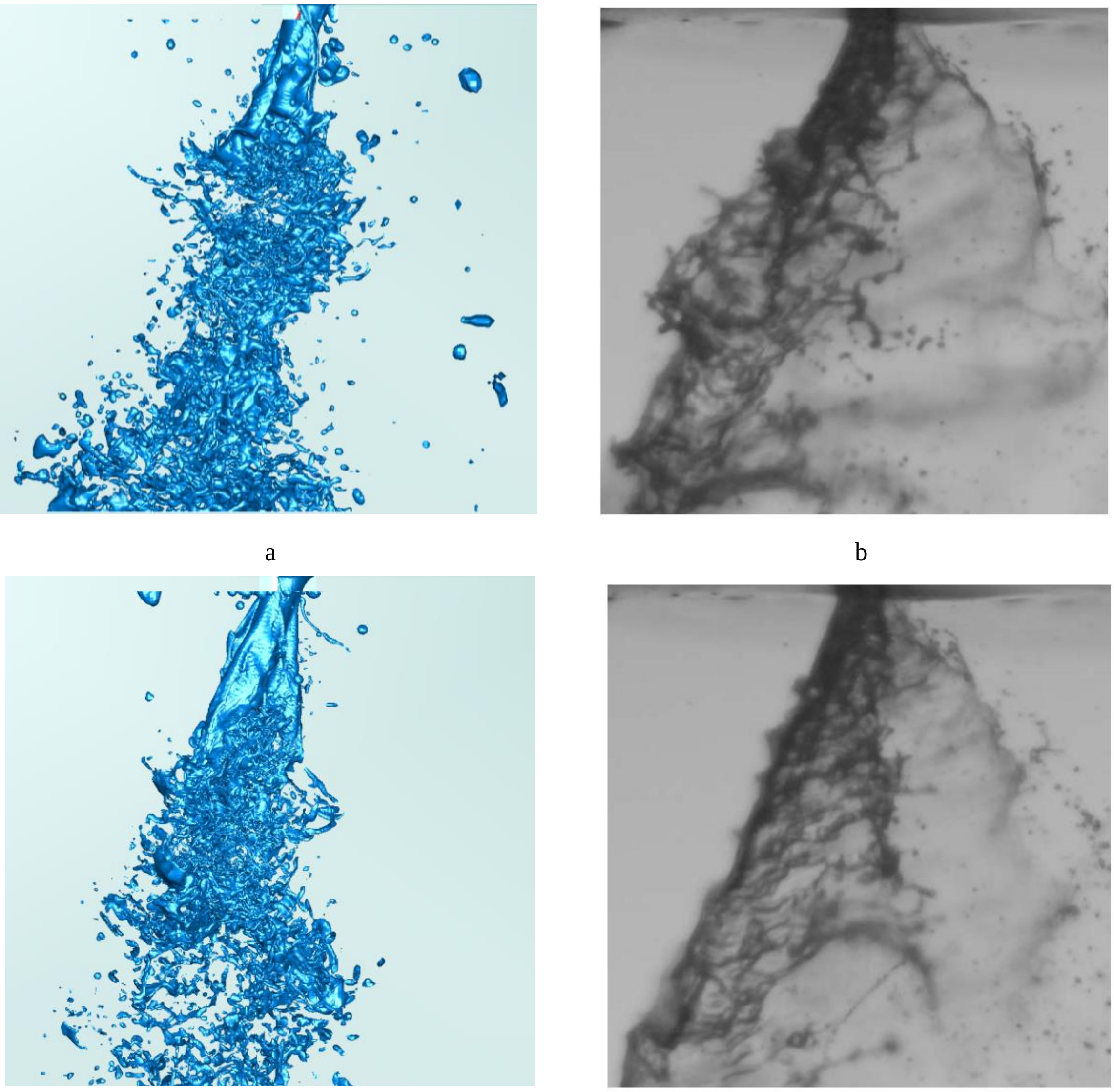

a b

c d

Figure 35: Comparison of the simulated liquid volume fraction iso-surface with photographs from the experiment of Ishimoto et al. [3] with the experiment. a) numerical simulation for t = 0.42ms and b) experiment. c) numerical simulation for t= 0.82ms and d) experiment.

Figure 35a shows the numerical result for $t = 0.42ms$ and Figure 35c represents the solution for $t = 0.82ms$. Opposite on the right hand side of both, visualizations the experimental data Ishimoto et al. [3] are shown. One can observe that the numerical results of AVL-FIRE^{TM} fit well with the experiment. The spray pattern tents to the same characteristic over the course of time. It should be mentioned that the mist which is visible on the right hand side of the experimental pictures, is not resolved by the numerical simulation. Instead there can be seen some large ligaments which are not disintegrated into to smaller droplets. This can be explained by the too coarse mesh cells in this part of the flow domain, and this demonstrated the limit of the performed multiphase simulation. For accurate results the mesh has to be fine enough to resolve the liquid-gas interface. In the current simulation, the interfaces of the ligaments there were not sharp enough, and thus leads to inaccurate break-up in comparison to the experiment. In general, the volume-equivalent sphere diameter from the numerical results should be compared with experimental data. This was not done in this work, since the droplet size distribution was not measured in the experiment from Ishimoto et al. [3].

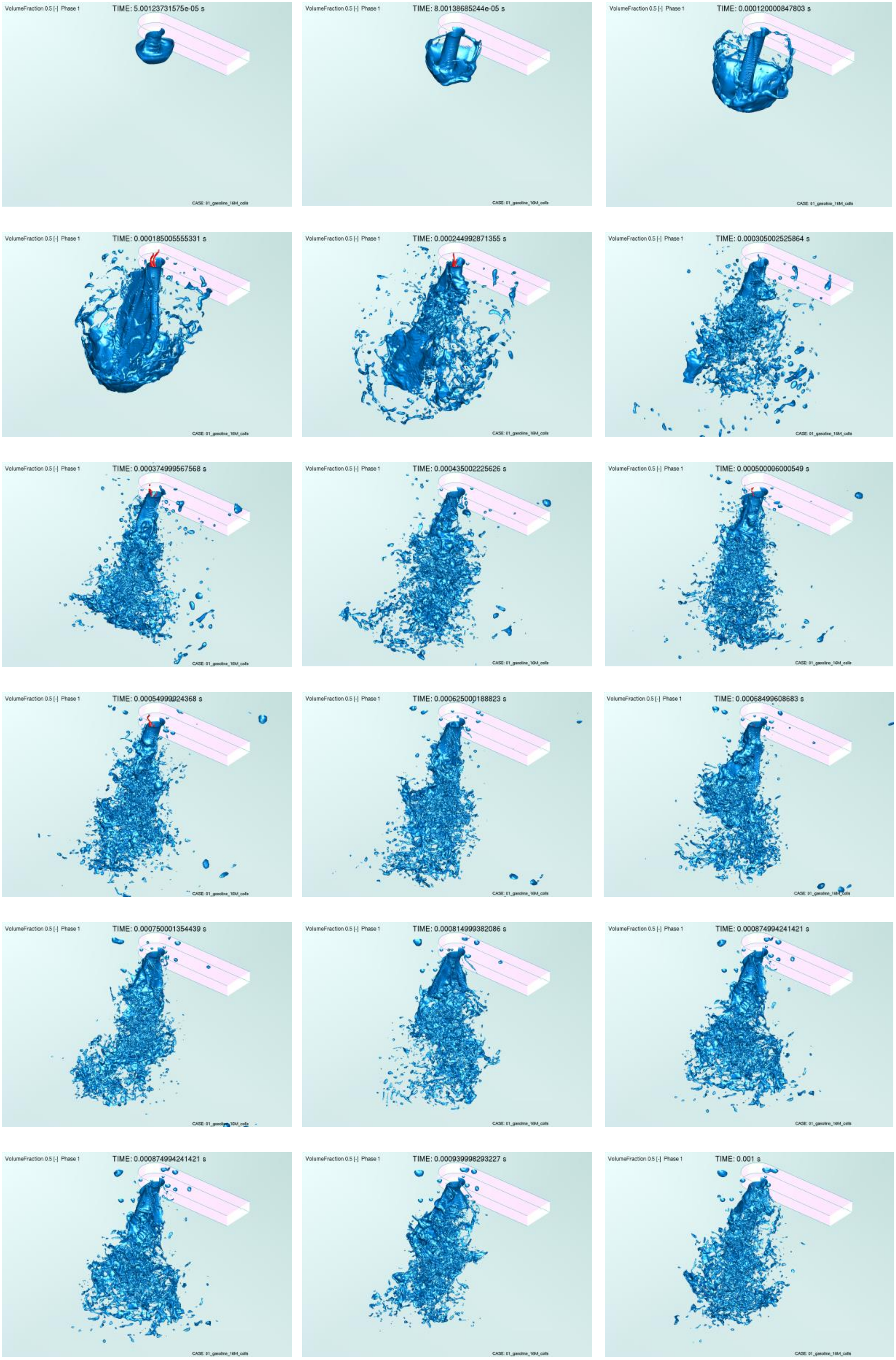

Figure 36: Visualization of the spray break-up from 0 to 1.0 ms.

5.3.4 Form Diagram

One task to evaluate the particle length algorithm was to test the code on a real multiphase simulation. Figure 38 shows the particle form diagram over different heights at the spray domain, as seen in Figure 37. For the height of 1.0 mm measured from the lower boundary, the evaluation is done for half of the spray domain. Each ligament which is inside these limits is detected, and the calculations described in chapter 3 were done to determine the characteristic lengths. Afterwards the form ratios were calculated for each particle and plotted by red colored dots into the particle form diagram. The separation into the different form regions in the diagram as seen in Table 3-1, it is possible to give a statement about the particle shape distribution.

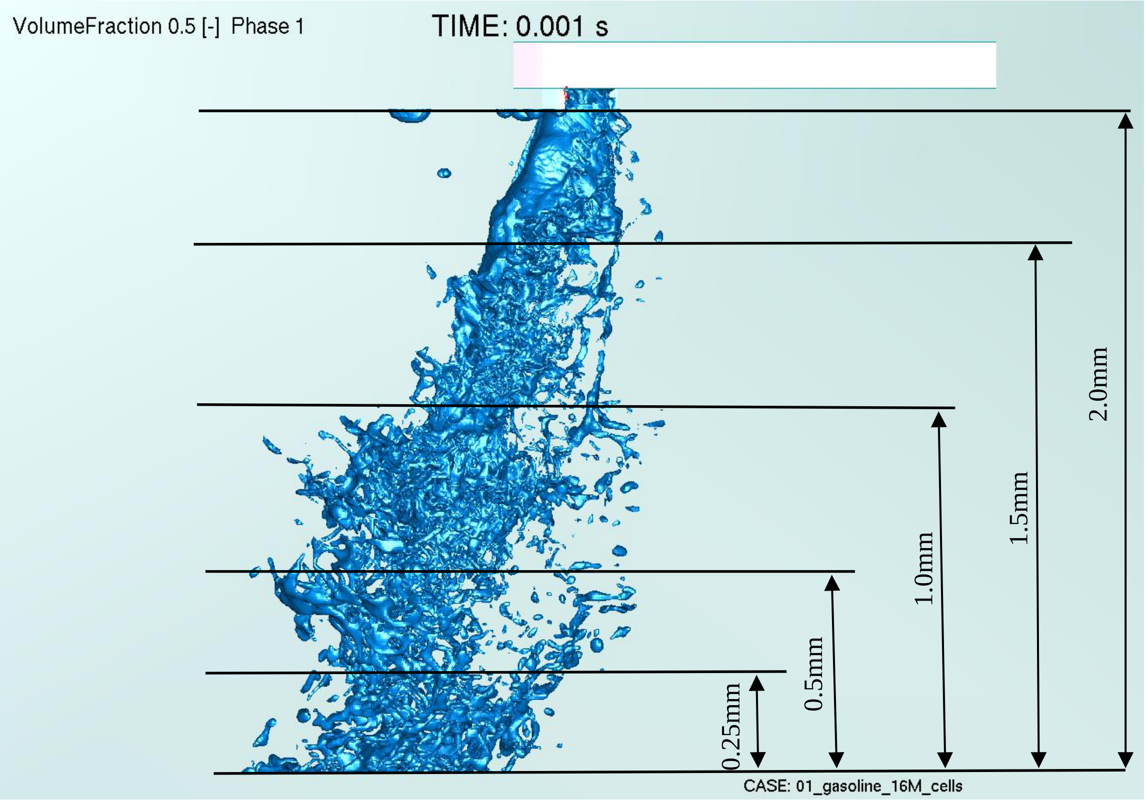

Figure 37: Height limits of the evaluation regions for the particle form diagram.

The results presented in Figure 38 were prepared for different heights from 0.25 mm to 1.5 mm from the bottom of the spray domain at the time of $t = 1.0\,ms$. Consequently, the regions with lower height include less particles. After analyzation it is realized that most ligaments tend to spherical or regularly shaped bodies, because the highest dot density can be seen in the area which is marked by capital A in the diagram.

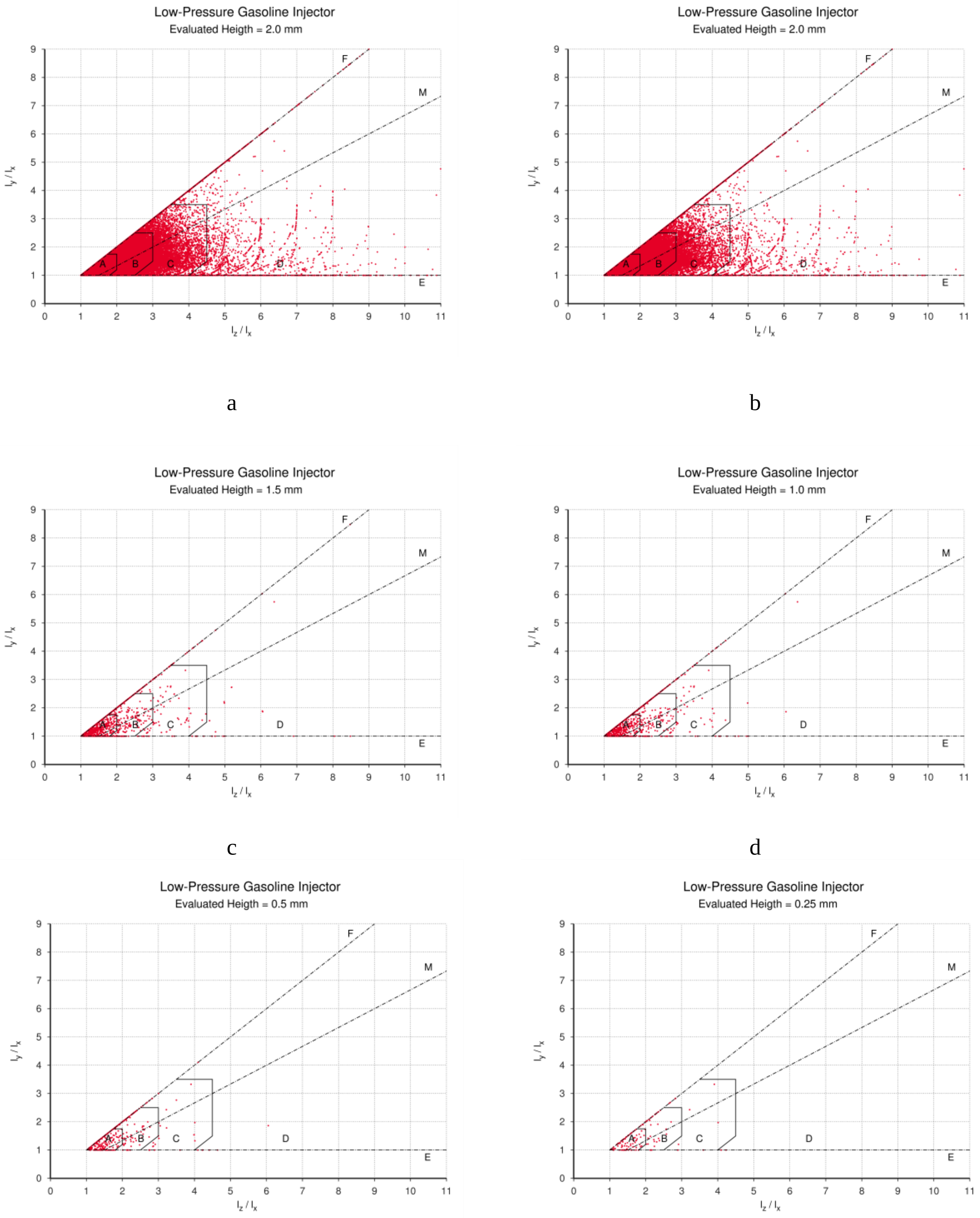

a

b

c

d

d

f

Figure 38: Form diagram of the Low-Pressure Injector over several heights of the evaluation domain over times from 0.0 – 1.0ms after start of injection. a) h = 2.0mm, t = 0.0 – 1.0 ms, b) h = 2.0mm, t = 0.5 – 1.0 ms, c) h = 1.5mm, t = 1.0 ms, d) h = 1.0mm, t = 1.0 ms, e) h = 0.5mm, t = 1.0 ms, f) h = 0.25mm, t = 1.0 ms.

5.3.5 Droplet Size Distribution

To give a meaningful statement about the droplet size distribution after spray break-up, a large number of particles should be considered. After the initial stage the spray reaches a quasi steady steate with homogeneous size distribution. The observed number of particles about 145000 in the period from 0.5 to 1.0ms over the whole spraying domain (for volume based droplet size distribution see Figure 39 and Figure 38b for corresponding particle shapes). The droplet size distribution is based on the volume-equivalent sphere diameters of all ligaments. It should be mentioned that for doing the analysis over the hole flow domain, the particles nearby the nozzle orifice may have a strongly nonspherical shape. By calculation of the equivalent sphere diameter this leads to some inaccuracy, because the longed and stretched will further disintegrate to single droplets of smaller size. This is visualized in Figure 38 for h = 0.25mm, since there are much less elongated or starched particles, because the analyzation was done downstream in the spray domain. Also the Sauter mean diameter tends there to smaller values. A positive side effect in the quantification of non-spherical ligaments, which was not able before the particle length detection was introduced.

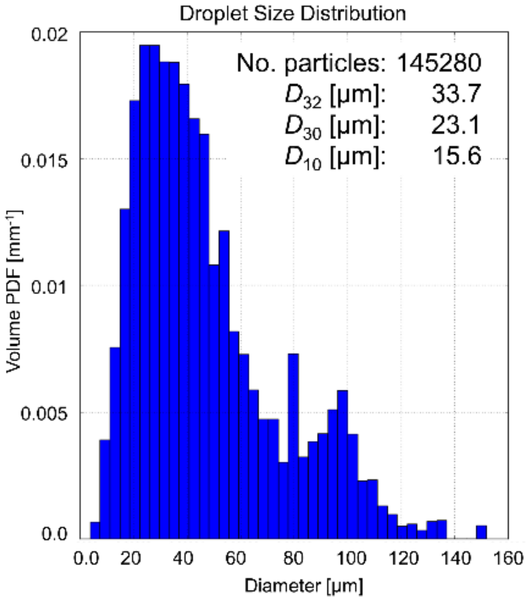

Figure 39: Volume based droplet size distribution for all evaluated particles between 0.5 and 1.0 ms.

5.3.6 Summary

The introduced particle length detection and the particle form diagram, both are now available in the commercial CFD-code AVL-FIRE^{TM} , have been tested for a big number of evaluated particles. The numerical for three phase simulation practices good results and was compared with the work of Ishimoto et al. [3]. the cavitation effects have been investigated. String cavitation was resolved by the simulation. Therefore a high mesh resolution and an LES causing high numerical effort are necessary. With the estimated Ohnesorge and Reynolds number, the classification into the so called second wind-induced break-up regime was done. Also the effects of the nozzle flow instabilities and the cavitation outlet were discussed and visualized. The particle length algorithm was tested in a real case application. In combination with the form diagram a quantification of the particle shapes is now possible. They allow a differentiation between spherical and non-spherical particle shapes over time in a graphical manner.

6 Summary and Conclusions

With this master thesis a new tool for particle length detection in multiphase flow simulations was introduced and implemented into the commercial software AVL-FIRE^{TM}. This new technique is the foundation of the particle form diagram which was introduced for fluid flow. Both tools will improve the spray break-up evaluation from VOF simulations. After implementation the tool was tested carefully by comparison with analytical results. The evaluation of the Volume-of-Fluid framework in AVL-FIRE^{TM} was done in combination with the particle length detection, the form diagram and the visualization of several postprocessing outputs. After the evaluation of the CICSAM and HRIC differencing schemes a statement about accuracy and form stability was given. In forms of accuracy and sharpness of the interface the CICSAM scheme performs better than the HRIC scheme. In calculations with the CICSAM scheme a wavy-surface on the interface was observed in some cases. In the relevant specialized literature, it is common knowledge that a surface which is tangential to the motion direction shows artificial wrinkling effects. These oscillations were also detected in the normalized form diagram. By variation of the blending factor better results could be achieved.

The low-pressure gasoline injector was calculated with the coupled VOF and the EE-approach in a three-phase simulation. The liquid-gas interface was resolved with the VOF-method, and the liquid-vapor interface was modeled with the EE-method. Cavitation effects were observed in different forms. String cavitation as consequence of nozzle flow instabilities were seen over the whole calculation period. As mentioned in the literature, string cavitation is highly unstable. The increasing and decreasing strings as well as bubble collapse and cavitation cloud implosion were seen many times during the simulated spray formation from 0 to 0.001s. Thus the nozzle instability and the cavitation effect influence the spray pattern. The dominant liquid of the multiphase spray simulations is the requirement for small cell sizes in the computational mesh. Otherwise the resolution of cavitation effects or maintaining a sharp interfaces between two phases is not possible. But all together the numerical simulation software AVL-FIRE^{TM} is able to calculate multiphase flow problems in reasonable manner. The comparison with experimental data shows a satisfying agreement. At the present day, it is not easy to predict cavitation effects like unstable string cavitation in a numerical simulation. This is a big advantage of the applied commercial CFD-code.

7 Outlook

The new tool for particle length detection provides the possibility for an improved coupling between the VOF-approach and the Lagrangian particle tracking method. This coupling would reduce the numerical effort, and so the costs of a spray calculation. One approach could be to calculate first the spray break-up with all relevant effects like cavitation and aerodynamical break-up with the VOF-method. The resulting spray pattern includes droplets of different sizes and shapes which can be then detected with the ligament length detection algorithm. The Lagrangian particle simulation use this data for initialization of the droplets and simulates the further spray pattern.

More investigation on the numerical setup should be done to reduce the wavy interface problem between two phases with high density ratios. As it seems these instability effects artificially increase the break-up rate, and lead to spray pattern with smaller ligaments and droplets sizes.

8 Appendix

8.1 Additional Information about the Test Cases Setup and the Evaluation

8.1.1 Plausibility of the Numerical Implementation

Table 8-1: Calculation setup for the test case “Plausibility of the Numerical Implementation”.

Calculation Setup		
Case: Plausibility of the Numerical Implementation		
Setting Type	**Selection**	**Comments for Selection**
Settings Differencing Scheme for VF-Equ.		
Differencing Scheme for VF-Equ.	CICSAM	most sharpening scheme in AVL-FIRE^{TM}
Belnding Exponent	2	default value to test with standard settings
General Calculation Settings		
MPI Parallelization	On 8 CPUs	dependency on fast calculation
Maximum Time	2.40E-02	depends how long particles stay inside the mesh
Turbulence Model	Laminar	is not solved in the volume fraction equation
Flow Category	Incompressible	compressible flows for VOF are not implemented
Gravitational Body Force	Disabled	is not used in the volume fraction equation
Pressure Correction Equation	SIMPLE	was not needed in frozen velocity field
ATS		
Automatic Time Step	Enabled	for fast and accurate results with default selection
ATS: Minimum Time Step	1.00E-06	was much lower as needed
ATS: Maximum Time Step	1.00	was much higher as needed
Solved Variabeles		
Velocity	U,V,W	solved in all three-coordinate axis
Volume Fraction	α	also used for the ligament length detection
Solved Equations		
Volume Fraction Equation	Enabled	is only needed for advection test
Momentum Equation	Disabled	not needed for advection test

8.1.2 Particle Convection Test

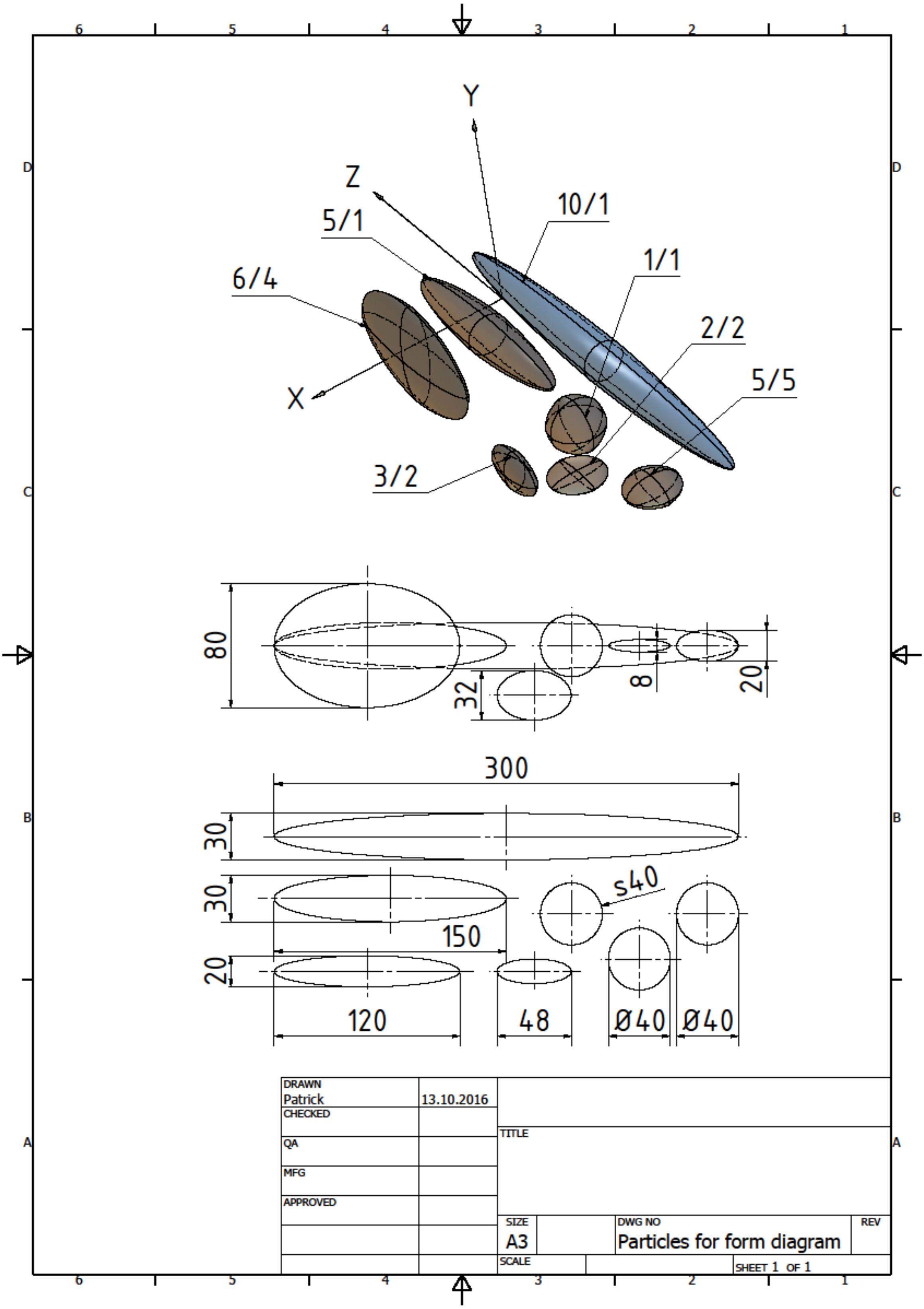

Figure 40: Detailed drawing of the particles for the “Particles Convection Test”.

Table 8-2: Calculation setup for the test case “Mesh Dependency for Translatory Particle Motion”.

Calculation Setup		
Case: Mesh Dependency for Translatory Particle Motion		
Setting Type	**Selection**	**Comments for Selection**
Settings Differencing Scheme for VF-Equ.		
Differencing Scheme for VF-Equ.	CICSAM	most sharpening scheme in AVL-FIRE^{TM}
Blending Exponent	2	default value to test with standard settings
General Calculation Settings		
MPI Parallelization	On 8 CPUs	dependency on fast calculation
Time Step	1.00E-06	selection based on former test cases
Turbulence Model	Laminar	is not solved in the volume fraction equation
Flow Category	Incompressible	compressible flows for VOF were not implemented in applied version
Gravitational Body Force	Disabled	is not used in the volume fraction equation
Pressure Correction Equation	SIMPLE	was not needed in frozen velocity field
Solved Variables		
Velocity	U,V,W	solved in all three-coordinate axis
Volume Fraction	α	also used for the ligament length detection
Solved Equations		
Volume Fraction Equation	Enabled	is only needed for advection test
Momentum Equation	Disabled	not needed for advection test

Table 8-3: Evaluation results of the particle convection test.

Evaluation Normalized Values

Case: Particle Convection Test

Initialization

Direction of motion	**X**		**Y**		**Z**		**XZ**		**XYZ**	
Classification of results	best	worst	best	worst	best	worst	best	worst	best	worst
Form factor	2/2	3/2	1/1	5/5	10/1	5/5	5/5	3/2	1/1	3/2
$I_{1\,in}^{norm}$	1.0084	0.9964	1.0020	1.0055	1.0021	1.0055	1.0055	0.9964	1.0020	0.9964
$I_{2\,in}^{norm}$	1.0084	0.9932	1.0020	1.0055	0.9991	1.0055	1.0055	0.9932	1.0020	0.9932
$I_{3\,in}^{norm}$	1.0085	0.9939	1.0020	1.0039	0.9991	1.0039	1.0039	0.9939	1.0020	0.9939
m_{in}^{norm}	1.0051	0.9972	1.0012	1.0105	1.0007	1.0110	1.0110	0.9972	1.0012	0.9972

Normalized Values for Maximum and Minimum

$I_{1\,max}^{norm}$	0.9854	0.9671	0.9838	0.9579	0.9989	0.9778	0.9676	0.9539	0.9662	0.9450
$I_{1\,min}^{norm}$	0.9671	0.9211	0.9668	0.8849	0.9975	0.9618	0.9569	0.9273	0.9589	0.9245
$I_{2\,max}^{norm}$	0.9893	0.9669	0.9838	0.9579	0.9933	0.9843	0.9689	0.9502	0.9694	0.9436
$I_{2\,min}^{norm}$	0.9815	0.9243	0.9668	0.8856	0.9914	0.9748	0.9603	0.9301	0.9603	0.9291
$I_{3\,max}^{norm}$	0.9870	0.9659	0.9846	0.9554	0.9933	0.9792	0.9647	0.9511	0.9698	0.9445
$I_{3\,min}^{norm}$	0.9728	0.9273	0.9757	0.8837	0.9914	0.9666	0.9572	0.9327	0.9603	0.9294
m_{max}^{norm}	0.9922	0.9801	0.9901	0.9839	0.9983	0.9965	0.9884	09703	0.9803	0.9648
m_{min}^{norm}	0.9848	0.9473	0.9814	0.9176	0.9973	0.9900	0.9844	0.9521	0.9753	0.9516

Loss of Accuracy

$I_{1\,max}^{er}$ [%]	3.29	7.89	3.32	11.51	0.23	3.82	4.31	7.27	4.11	7.55
$I_{2\,max}^{er}$ [%]	1.85	7.57	3.32	11.44	0.86	2.52	3.96	6.99	3.97	7.09
$I_{3\,max}^{er}$ [%]	2.72	7.27	2.43	11.6	0.86	3.34	4.28	6.72	3.97	5.56
m_{max}^{er} [%]	1.52	5.27	1.86	8.23	0.27	1.00	1.56	4.79	2.47	4.84

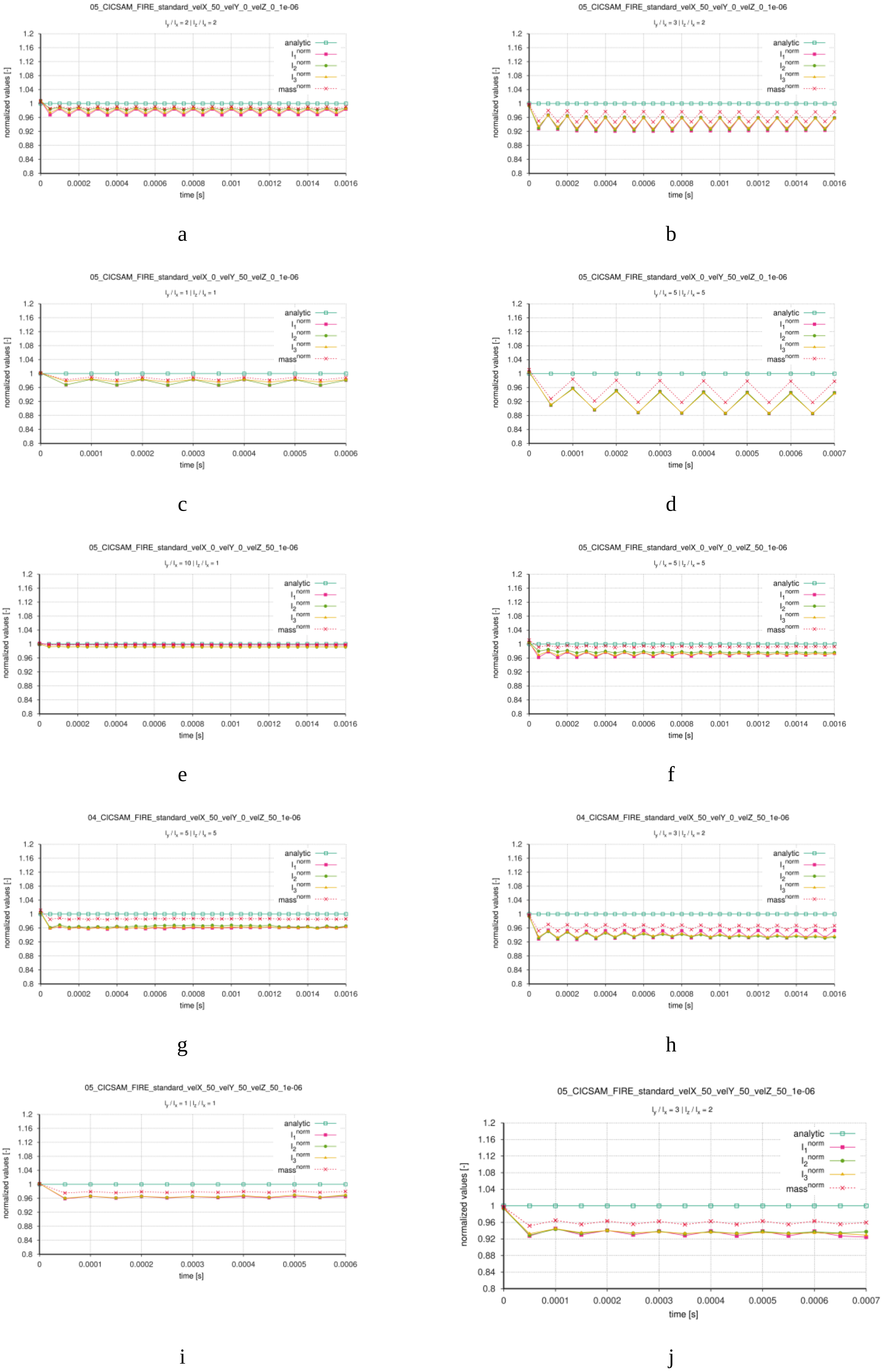

Figure 41: Normalized variable diagram for the mesh dependency test. a) form factor 2/2, b) form factor 3/2, c) form factor 1/1, d) form factor 5/5, e) form factor 10/1, f) form factor 5/5, g) form factor 5/5, h) form factor 3/2, i) form factor 1/1, j) form factor 3/2.

8.1.3 Dependency on the Blending Exponent

Table 8-4: Calculation setup for dependency on the blending exponent.

Calculation Setup		
Case: Mesh Dependency for Translatory Particle Motion		
Setting Type	**Selection**	**Comments for Selection**
Settings Differencing Scheme for VF-Equ.		
Differencing Scheme for VF-Equ.	CICSAM	most sharpening scheme in AVL-FIRE^{TM}
Blending Exponent	0 0.5 1 2	blending factor variation
General Calculation Settings		
MPI Parallelization	On 8 CPUs	dependency on fast calculation
Time Step	1.00E-06	selection based on former test cases
Turbulence Model	Laminar	is not solved in the volume fraction equation
Flow Category	Incompressible	compressible flows for VOF are not implemented
Gravitational Body Force	Disabled	is not used in the volume fraction equation
Pressure Correction Equation	SIMPLE	was not needed in frozen velocity field
Solved Variables		
Velocity	U,V,W	solved in all three-coordinate axis
Volume Fraction	α	also used for the ligament length detection
Solved Equations		
Volume Fraction Equation	Enabled	is only needed for advection test
Momentum Equation	Disabled	not needed for advection test

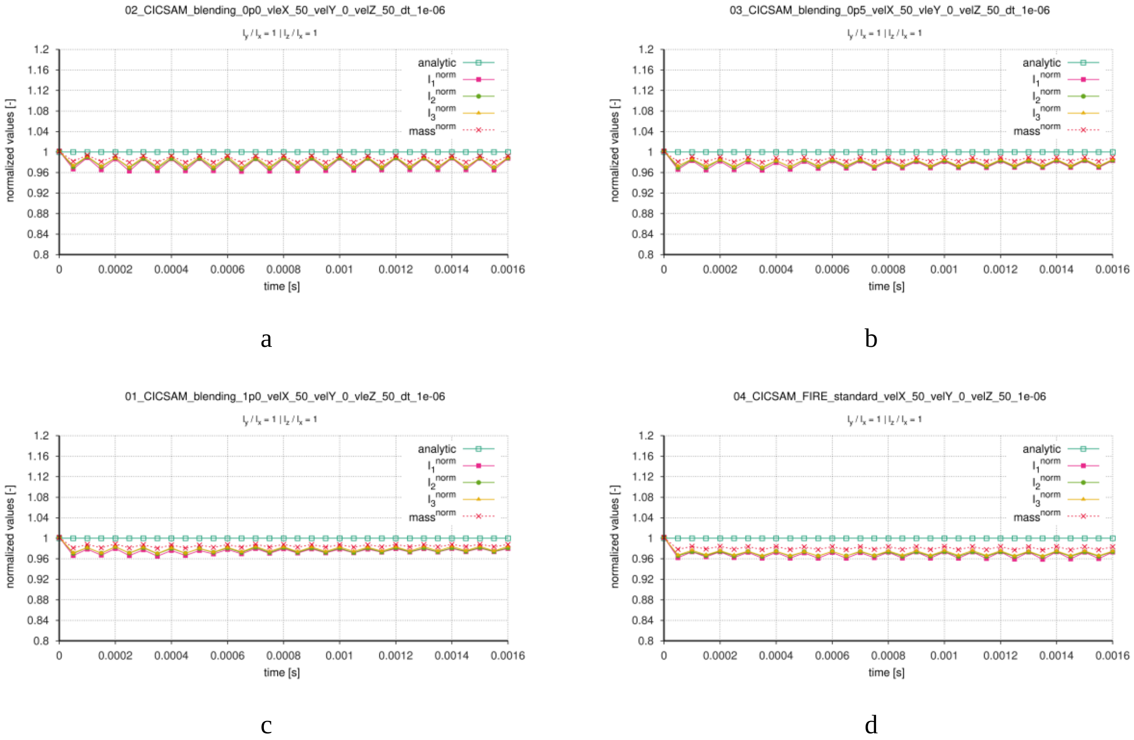

a b

c d

Figure 42: Variation of the blending exponent for a spherical particle with form ratio 1/1. a) blending exponent $C_\theta = 0$, b) blending exponent $C_\theta = 0.5$, c) blending exponent $C_\theta = 1$, d) blending exponent $C_\theta = 2$.

Table 8-5: Evaluation of the “Dependency on blending exponent” test case.

Evaluation Normalized Values

Case: Dependency on Blending Exponent

Initialization

Blending Factor	**0**	**2**
Form factor	5/5	
$I_{1\ in}^{norm}$	1.0055	
$I_{2\ in}^{norm}$	1.0055	
$I_{3\ in}^{norm}$	1.0039	
m_{in}^{norm}	1.0110	

Normalized Values for Maximum and Minimum

$I_{1\ max}^{norm}$	0.9948	0.9646
$I_{1\ min}^{norm}$	0.9617	0.9569
$I_{2\ max}^{norm}$	0.9961	0.9689
$I_{2\ min}^{norm}$	0.9669	0.9603
$I_{3\ max}^{norm}$	0.9940	0.9647
$I_{3\ min}^{norm}$	0.9621	0.9572
m_{max}^{norm}	1.0033	0.9884
m_{min}^{norm}	0.9879	0.9844

Loss of Accuracy

$I_{1\ max}^{er}$ [%]	3.83	4.31
$I_{1\ min}^{er}$ [%]	0.52	3.54
$I_{2\ max}^{er}$ [%]	3.31	3.97
$I_{2\ min}^{er}$ [%]	0.39	3.11
$I_{3\ max}^{er}$ [%]	3.79	4.28
$I_{3\ min}^{er}$ [%]	0.60	3.53
m_{max}^{er} [%]	3.3	1.56
m_{min}^{er} [%]	1.21	1.16

8.1.4 Slotted Sphere Test Case

Table 8-6: Calculation setup for the “Slotted Sphere” test case.

Calculation Setup		
Case: Slotted Sphere		
Setting Type	**Selection**	**Comments for Selection**
Settings Differencing Scheme for VF-Equ.		
Differencing Scheme for VF-Equ.	CICSAM	most sharpening scheme in AVL-FIRE^{TM}
Blending Exponent	2	blending factor variation
General Calculation Settings		
MPI Parallelization	On 8 CPUs	dependency on fast calculation
Maximum Time	0.16 s	depends of the number of rotations
Turbulence Model	Laminar	is not solved in the volume fraction equation
Flow Category	Incompressible	compressible flows for VOF are not implemented in applied version
Gravitational Body Force	Disabled	is not used in the volume fraction equation
Pressure Correction Equation	SIMPLE	was not needed in frozen velocity field
Solved Variables		
Velocity	U,V,W	solved in all three-coordinate axis
Volume Fraction	α	also used for the ligament length detection
Solved Equations		
Volume Fraction Equation	Enabled	is only needed for advection test
Momentum Equation	Disabled	not needed for advection test
Automatic Time Step		
CFL Flow	0.5	is only needed for advection test
CFL Threshold VOF Interphase	0.5 0.45 0.25	variation; first column is standard setting

Table 8-7: Evaluation of the “Slotted Sphere” test case.

Evaluation Normalized Values

Case: Slotted Sphere

Initialization

CFL Threshold VOF Interface	**0.5**	**0.45**	**0.25**
Form factor	1/1		
$I^{norm}_{1\,in}$	1.0232		
$I^{norm}_{2\,in}$	1.0225		
$I^{norm}_{3\,in}$	1.0310		
m^{norm}_{in}	1.0110		

Normalized Values for Maximum and Minimum

$I^{norm}_{1\,max}$	0.8542	0.8911	0.9307
$I^{norm}_{1\,min}$	0.6431	0.8258	0.9038
$I^{norm}_{2\,max}$	0.8985	0.9209	0.9590
$I^{norm}_{2\,min}$	0.8089	0.8975	0.9435
$I^{norm}_{3\,max}$	0.9044	0.9293	0.9578
$I^{norm}_{3\,min}$	0.7935	0.9120	0.9499
m^{norm}_{max}	0.9407	0.9691	0.9986
m^{norm}_{min}	0.8326	0.9401	0.9832

Loss of Accuracy

$I^{er}_{1\,max}$ [%]	35.69	17.42	9.62
$I^{er}_{1\,min}$ [%]	14.58	10.89	6.93
$I^{er}_{2\,max}$ [%]	19.10	10.25	5.65
$I^{er}_{2\,min}$ [%]	10.15	7.91	4.10
$I^{er}_{3\,max}$ [%]	20.65	8.8	5.01
$I^{er}_{3\,min}$ [%]	9.56	7.07	4.22
m^{er}_{max} [%]	16.74	3.09	1.68
m^{er}_{min} [%]	5.93	5.99	0.14

Number of Time Steps

Number	2488	3040	5328

8.2 Comparison of the CICSAM and HRIC-scheme

8.2.1 Scheme Comparison of the “Translatory Particle Motion” Test Case

Table 8-8: Evaluation of the “Translatory Particle Motion” test case.

Evaluation Normalized Values

Case: Comparison for Translatory Particle Motion

Initialization

Direction of Motion	**Y**			
Differenzing Scheme	CICSAM	HRIC	CICSAM	HRIC
Form factor	1/1		5/5	
$I^{norm}_{1\,in}$	1.0020		1.0055	
$I^{norm}_{2\,in}$	1.0020		1.0055	
$I^{norm}_{3\,in}$	1.0020		1.0039	
m^{norm}_{in}	1.0012		1.0105	
$I^{norm}_{1\,max}$	0.9838	0.9528	0.9579	0.9545
$I^{norm}_{1\,min}$	0.9668	0.9474	0.8849	0.9466
$I^{norm}_{2\,max}$	0.9838	0.9594	0.9579	0.9572
$I^{norm}_{2\,min}$	0.9668	0.9535	0.8856	0.9506
$I^{norm}_{3\,max}$	0.9846	0.9605	0.9554	0.9527
$I^{norm}_{3\,min}$	0.9757	0.9549	0.8837	0.9469
m^{norm}_{max}	0.9901	0.9733	0.9839	0.9818
m^{norm}_{min}	0.9814	0.9697	0.9176	0.9775

Loss of Accuracy

$I^{er}_{1\,max}$ [%]	3.32	5.26	11.51	5.34
$I^{er}_{2\,max}$ [%]	3.32	4.65	11.44	4.94
$I^{er}_{3\,max}$ [%]	2.43	4.51	11.6	5.31
m^{er}_{max} [%]	1.86	3.03	8.23	2.25

8.2.2 Scheme Comparison in the Slotted Cylinder Test Case

Table 8-9: Calculation setup for the “ Slotted Cylinder” test case.

Calculation Setup

Case: Slotted Cylinder

Setting Type	Selection		Comments for Selection
Settings Differencing Scheme for VF-Equ.			
Differencing Scheme for VF-Equ.	CICSAM	HRIC	variation of the differencing scheme
Blending Exponent	2	0.05	blending factor was default
General Calculation Settings			
MPI Parallelization	On 8 CPUs		dependency on fast calculation
Maximum Time	0.16 s		depends of the number of rotations
Turbulence Model	Laminar		is not solved in the volume fraction equation
Flow Category	Incompressible		compressible flows for VOF are not implemented
Gravitational Body Force	Disabled		is not used in the volume fraction equation
Pressure Correction Equation	SIMPLE		was not needed in frozen velocity field
Solved Variables			
Velocity	U,V,W		solved in all three-coordinate axis
Volume Fraction	α		also used for the ligament length detection
Solved Equations			
Volume Fraction Equation	Enabled		is only needed for advection test
Momentum Equation	Disabled		not needed for advection test
Automatic Time Step			
CFL Flow	0.5		is only needed for advection test
CFL Threshold VOF Interface	0.45		was for all calculations the same

Table 8-10: Evaluation for the "Slotted Cylinder" test case.

Evaluation Normalized Values

Case: Slotted Cylinder

Initialization

Differencing scheme	**CICSAM**	**HRIC**
Form factor	2/1	
$I_{1\,in}^{norm}$	1.0228	
$I_{2\,in}^{norm}$	1.0441	
$I_{3\,in}^{norm}$	1.0361	
m_{in}^{norm}	1.0562	

Normalized Values for Maximum and Minimum

$I_{1\,max}^{norm}$	0.9411	0.9276
$I_{1\,min}^{norm}$	0.9332	0.9140
$I_{2\,max}^{norm}$	0.9594	0.9422
$I_{2\,min}^{norm}$	0.9505	0.9202
$I_{3\,max}^{norm}$	0.9622	0.9408
$I_{3\,min}^{norm}$	0.9547	0.9275
m_{max}^{norm}	0.9918	0.9756
m_{min}^{norm}	0.9860	0.9578

Loss of Accuracy

$I_{1\,max}^{er}$ [%]	6.68	8.60
$I_{1\,min}^{er}$ [%]	5.89	7.24
$I_{2\,max}^{er}$ [%]	4.95	7.98
$I_{2\,min}^{er}$ [%]	4.06	5.78
$I_{3\,max}^{er}$ [%]	4.53	7.25
$I_{3\,min}^{er}$ [%]	3.78	5.92
m_{max}^{er} [%]	1.40	4.22
m_{min}^{er} [%]	0.82	2.44

Number of Time Steps

Number	3582	3612

8.3 Primary Break-up at the Low-Pressure Gasoline Injector

Table 8-11: Calculation setup for the “Low-Pressure Injector” simulation.

Calculation Setup

Case: Low-Pressure Injector

Setting Type	Selection	Comments for Selection
Settings Differencing Scheme for VF-Equ.		
Differencing Scheme for VF-Equ.	CICSAM	most sharpening scheme in AVL-FIRE^{TM}
Blending Exponent	0.25	smaller blending factor for sharper interface
General Calculation Settings		
MPI Parallelization	On 90 processors	dependency on big number of cells
Maximum Time	0.001 s	based on publication [3]
Turbulence Model	LES-CSM model	based on publication [4]
Flow Category	Incompressible and isothermal	compressible flows for VOF are not implemented in applied version
Gravitational Body Force	Enabled	considered during vertical motion of particles
Pressure Correction Equation	SIMPLE	coupling for pressure and velocity
Solved Variables in the Balance Equations		
Velocity	U,V,W	solved in all three-coordinate axis
Pressure	p	equal for all phases
Volume Fraction	α	also used for the ligament length detection
Solved Equations		
Volume Fraction Equation	Enabled	transport equation for volume fraction
Momentum Equation	Enabled	includes terms of surface tension and gravity force, mass and momentum transfer, turbulence pressure and momentum transfer for mass
Automatic Time Step		
CFL Flow	0.5	is only needed for advection test
CFL Threshold VOF Interface	0.45	was for all calculations the same

References

[1] Wallis G B, One-dimensional two-phase flow, New York: LinkMcGraw-Hill, 1969.

[2] Edelbauer W, Birkhold F, Rankel R, Pavlovic Z, Kolar P, Simulation of the Liquid Break-up at an AdBlue Injector with the Volume-of-Fluid method followed by Off-Line Coupled Lagrangian Particle Tracking, Comoputers & Fluids, in press, available online 6 September, 2017.

[3] Ishimoto J, Sato, F, Sato G, Computational Prediction of the Effect of Microcavitation on an Atomization Mechanism in a Gasoline Injector Nozzle., vol. 132, Journal of Engineering for Gas Turbines and Power, Vol. 132, Issue 8, 2010.

[4] Edelbauer W, Numerical simulation of cavitating injector flow and liquid spray break-up by combination of Euleria-Eulerian and Volume-of-Fluid methods, Computer and Fluids, Vol. 144, 2016, pp. 19-33.

[5] Drew D, Passman S, Theory of Multicomponent Fluids, Springer, 1999.

[6] Alajbegovic A, Greif D, Basara B, Iben U, Cavotation Calculation with the Two-Fluid Model, Certosa di Pontignano: Proceedings of the 3rd European-Japanese two-phase flow group meeting, Italy 2003.

[7] Sauer J, Winkler G, Schnerr GH, Cavitation and Condensation – Common Aspects of Physical Modeling and Numerical Approach, Chemical Engineering Technology, Vol. 23, Issue 8, 2000, p. 663–666.

[8] Schiller L, Naumann A, Über die grundlegenden Berechnung bei der Schwerkraftaufbereitung, Verband Deutscher Ingenieure, Vol. 77, 1933, pp. 318-320.

[9] Hirt C W, Nichols B D, Volume of Fluid (VOF) Method for the Dynamics of Free Boundaries, 39 ed., Journal of Computational Physics,Vol. 39, Issue 1, 1981, pp. 201 - 225.

[10] AVL FIRE, user manual version v2017, 2017.

[11] Hirsch CH, Numerical computation of internal and external flows, Butterworth-Heinemann, 2007.

[12] Waclawczyk T, Koronowicz T, Modeling of the Wave Breaking with CICSAM and HRIC-Resolution schemes, Netherlands: ECCOMAS CFD 2006: Proceedings of the European Conference on Computational Fluid Dynamics, 2006.

[13] Leonard B P, The ULTIMATE conservative difference scheme applied to unsteady one-dimensional advection, Computer Methods in Applied Mechanics and Engineering, Vol. 88, Issue 1, 1991, pp. 17-74.

[14] Gaskell A. P , Lau A. K. C, Curvature-compensated convective transport: SMART, A new boundedness- preserving transport algorithm, Numerical Methods in Fluids, Vol. 8, Issue 6, 1988.

[15] Ubbink O, Numerical prediction of two fluid systems with sharp interfaces, Ph.D. Thesis, University of London, 1997.

[16] Muzaferija S, Peric M, Sames P, Schellin T, A Two-Fluid Navier-Stokes Solver to Simulate Water Entry, Conference: 22nd Symposium on Naval Hydrodynamics, At Washington, D.C., 1998, pp. 638-651.

[17] Brackbill J U, Kothe D B, Zemach C, A Continuum method for modelling surface tension, Journal of Computational Physics, Vol. 100, Issue 2, 1992, pp. 335-354.

[18] Alajbegovic A, Large Eddy simulation fomalism applied to multiphase flows, New Orleans, Louisiana: Proceedings of the 2001 ASME Fluids Engineering Division Summer Meeting, May 29 - June 1, 2001.

[19] Smagorinsky J, General circulation experiments with the primitive equations, part I: the basic experiment, Monthly Weather Review, Vol. 9, Number 3, 1963, pp. 99-164.

[20] Kobayashi H, The subgrid-scale models based on coherent structures for rotating homogeneous turbulence and turbulent channel flow, Physics of Fluids, Vol. 17, 2005.

[21] Parkus H, Mechanik der festen Körper, 2. Auflage, Springer.

[22] Kessel S, Fröhling D, Technische Mechanik - Engineering Mechaniks, vol. 2, Springer Vieweg, 2012.

[23] Dankert J, Dankert H, Technische Mechanik, 7. Auflage, Springer Vieweg, 2013.

[24] Bartsch H J, Taschenbuch für Ingenieure und Naturwissenschaftler, München: Carl Hansa Verlag, 2014.

[25] Ohnesorge W, Die Bildung von Tropfen an Düsen und die Auflösung flüssiger Strahlen., Zeitschrift für angewandte Mathematik und Mechanik, Vol 16, Issue 6, 1936, p. 355–358.

[26] Lefebvre A, Atomization and Spray, 1989.

[27] Reitz R D, Bracco F V, Mechanisms of Breakup of Round Liquid Jets, The Encyclopedia of Fluid Mechanics, Vol. 3, 1986, pp. 223-249.

[28] Baumgarten C, Modellierung des Kaviationseinflusse auf den primärenStrahlzerfalles bei Hodruck-Dieseleinspritzungen, VDI-Verlag, Ed., Fortschritt-Berichte VDI, 2003.

[29] Som S, Aggarwal S K, Effects of primary breakup modeling on spray and combustion characteristics of compression ignition engines, Combustion and Flame,Vol. 157, Issue 6, 2010, pp. 1179-1193.

[30] Leick P, Quantitative Untersuchungen zum Einfluss von Düsengeometrie und Gasdichte auf den Primärzerfallsbereich von Dieselsprays, Ph.D. Thesis, TU Darmstadt, 2008.

[31] Sauter J, Die Grössenbestimmung der in Gemischnebeln von Verbrennungskraftmaschinen vorhandenen Brennstoffteilchen, VDI-Forschungsheft Nr. 279, 1926.

[32] Walz, Die Betonstraße, Vol 11, 1936, p. 27–36.

[33] Stieß M, Mechanische Verfahrenstechnik- Partikeltechnologie 1, 3 ed., vol. 1, Springer Berlin Heidelberg, 2009.

[34] Zalesak S, Fully multidimensional flux-corrected transport algorithms for fluids, Journal of Computational Physics, Vol. 31, Issue 3, 1979, pp. 335-362.

[35] Merziger G, Wirth T, Repetitorium der höheren Mathematik, 5 ed., Binomi, 2006.

[36] Edelbauer W, Kolar P, Schellander D, Pavlovic Z, Almbauer R, Numerical Simulation of Spray Break-up from Cavitating Nozzle Flow by Combined Eulerian-Eulerian and Volume-of-Fluid Methods, Int. J. Comp. Meth. and Exp. Meas. , in press, 2017.

[37] Edelbauer W, Coupling of 3D Eulerian and Lagrangian Spray Approaches in Industrial Combustion Engine Simulations, Journal of Energy and Power Engineering, Vol. 8, 2014, pp. 190-200.